REPORT NO. ACNP-6012

PATHFINDER ATOMIC POWER PLANT
TECHNICAL PROGRESS REPORT

JULY 1960 - SEPTEMBER 1960

Submitted to

U. S. ATOMIC ENERGY COMMISSION

NORTHERN STATES POWER COMPANY

and

CENTRAL UTILITIES ATOMIC POWER ASSOCIATES

by

ALLIS-CHALMERS MANUFACTURING COMPANY
ATOMIC ENERGY DIVISION
Milwaukee 1, Wisconsin

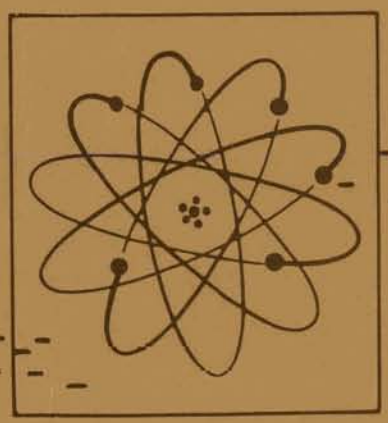

Ref: AEC Contract No. AT(11-1)-589

DISCLAIMER

LEGAL NOTICE

PATHFINDER ATOMIC POWER PLANT
TECHNICAL PROGRESS REPORT
JULY 1960 – SEPTEMBER 1960

Submitted to

U. S. ATOMIC ENERGY COMMISSION

NORTHERN STATES POWER COMPANY

and

CENTRAL UTILITIES ATOMIC POWER ASSOCIATES

by

ALLIS-CHALMERS MANUFACTURING COMPANY

Under

Agreement dated 2nd Day of May 1957, as Amended
between
Allis-Chalmers Mfg. Co. & Northern States Power Co.
under
AEC Contract No. AT (11-1)-589

(January 5, 1961)

Approved: C. B. Graham
C. B. Graham
Chief Engineer
Nuclear Power Dept.–Greendale

Approved: C. R. Braun
C. R. Braun
Manager
Nuclear Power Dept.–Greendale

ALLIS-CHALMERS MANUFACTURING COMPANY
ATOMIC ENERGY DIVISION
MILWAUKEE 1, WISCONSIN

Approved: Hibbert Hill
Hibbert Hill
Chief Engineer

NORTHERN STATES POWER COMPANY
15 SOUTH FIFTH STREET
MINNEAPOLIS 2, MINNESOTA

THIS PAGE

WAS INTENTIONALLY

LEFT BLANK

TECHNICAL PROGRESS REPORT

JULY 1960 - SEPTEMBER 1960

DISTRIBUTION

USAEC, Chicago Operations Office - 9800 S. Cass Ave., Argonne, Illinois	8
USAEC, Division of Reactor Development - Washington 25, D.C.	8
USAEC, TISE, Oak Ridge, Tennessee OFFSET MASTER, PLUS	20
Northern States Power Company & CUAPA	35
Allis-Chalmers Manufacturing Company	39
TOTAL COPIES	110

THIS PAGE

WAS INTENTIONALLY

LEFT BLANK

TABLE OF CONTENTS

Page

Distribution..... iii
List of Illustrations..... vii
Foreword..... xi
Design Data..... xii

Part A Preconstruction Research and Development

1. Fuel Element Research and Development
   1.1 Fuel Material Cladding, Bonding, and Irradiation Testing.... 1
   1.2 Heat Transfer and Fluid Flow..... 8
   1.4 Fuel Element Manufacturing Research & Development..... 19
   1.5 Nuclear Handling Tools..... 57
   1.6 Low-Enrichment Superheater Fuel Element..... 59

2. Reactor Mechanical Studies
   2.1 Vessel and Structures..... 93
   2.2 Recirculation System..... 112
   2.3 Control Rods, Guide Tubes, and Control Rod Drives..... 115

3. Nuclear Analysis
   3.1 Reactor Physics (Statics)..... 123
   3.2 Reactor and System Dynamics..... 134
   3.3 Critical Experiments..... 152

Part B Postconstruction Research and Development

1. Initial Stability and Performance Tests
   1.1 Oscillator Rod and Drive..... 165

THIS PAGE

WAS INTENTIONALLY

LEFT BLANK

LIST OF ILLUSTRATIONS

Figure Number	Title	Page Number
I.1	Test section containing radioactive sample	2
I.2	Drilling fixture for preparing calibration standards for superheater corrosion-erosion test	3
I.3	Count as a function of weight of radioactive sample	4
I.4	Schematic of heat transfer loop	9
I.5	Boiler element mock-up assembly	11
I.6	Aluminum-lucite subassembly mock-up	13
I.7	Maximum wall temperatures at partial and full power and pressure	17
I.8	Pressure drop through core at partial power and pressure	17
I.9	Flat-bottom four-element quad box with integral control rod stub	22
I.10	Step-tube boiler fuel element assembly	23
I.11	Stress-strain curve for Zircaloy-2 at 600 F	26
I.12	Boiler fuel-rod thermal bowing	26
I.13	Fuel-rod-cladding allowable pressure vs. ovality at 750 F	29
I.14	Allowable pressure vs. wall thickness for 0.353 i.d. at 750 F	29
I.15	Allowable pressure vs. wall thickness for 0.327 i.d. tube at 750 F	29
I.16	Allowable pressure vs. wall thickness for 0.315 i.d. tube at 750 F	29
I.17	304 stainless-steel nozzle and sleeve after nozzle galling test	41
I.18	17-4 Ph stainless steel nozzle and stainless steel sleeve after nozzle galling test	41

Figure Number	Title	Page Number
I.19	Galling of 17-4 Ph nozzle and 304 sleeve	43
I.20	Chrome plated 304 nozzle and 304 sleeve after galling test	45
I.21	Final roll and sinter of uranium dioxide stainless steel cermet	48
I.22	Layout of head for boiler fuel handling tool	58
I.23	Swage-compacting of uranium dioxide powder in 316 L stainless steel tubes	66
I.24	Swage-compacted, stainless steel clad, uranium dioxide fuel rods	67
I.25	Swaged density vs. powder particle size	68
I.26	As-received 316 L stainless steel tubing 0.010-in thick used in swaging JK-A series rods	69
I.27	Photomicrographs of swaged cladding JK-A1	70-71
I.28	Photomicrographs of swaged cladding JK-A3	70-71
I.29	Photomicrographs of swaged cladding JK-A5	70-71
I.30	Photomicrographs of swaged cladding JK-A7	72-73
I.31	Photomicrographs of swaged cladding JK-A9	72-73
I.32	Photomicrographs of swaged cladding JK-A10	72-73
I.33	Photomicrographs of swaged cladding JK-A12	74-75
I.34	Photomicrographs of swaged cladding JK-A14	74-75
I.35	Photomicrographs of swaged cladding JK-A16	74-75
I.36	Photomicrographs of swaged cladding JK-A18	76-77
I.37	Photomicrographs of swaged cladding JK-A19	76-77
I.38	Photomicrographs of swaged cladding JK-A20	76-77
I.39	Photomicrographs of swaged cladding JK-A33	78
I.40	Photomicrographs of swaged cladding JK-A33	78

Figure Number	Title	Page Number
I.41	Photomicrographs of as-received stainless steel tubing 0.370-in o.d	82-83
I.42	Photomicrographs of as-received stainless steel tubing 0.350-in o.d	82-83
I.43	Photomicrographs of as-received stainless steel tubing 0.330-in o.d	82-83
I.44	Photomicrographs of JKI-I (64.6 per cent reduction)	84-85
I.45	Photomicrographs of JKI-AI (64.6 per cent reduction)	84-85
I.46	Rotary straightened swage-compacted clad	86
2.1	Full-scale closure test	94
2.2	Meridional stresses in closure due to bolt load	95
2.3	Closure test bolting up to 30,000 psi stress	95
2.4	Schematic diagram of moisture de-entrainment test setup	99
2.5	Moisture entrained 33 in. above interface in a 19-in diameter test section	100
2.6	Schematic of centrifugal steam dryers	102
2.7	Outlet moisture from centrifugal steam dryer	102
2.8	Outlet moisture from 6-in thick mesh steam dryer	103
2.9	Steam separator support shelf	107
2.10	Superheater seal test assembly	109
2.11	Prototype recirculation pump being tested in hot test loop at reactor conditions	113
2.12	Comparison of boiler control rod displacement with and without net coolant flow	118
3.1	Superheater power fraction for various fuel and burnable poison loadings	129
3.2	Superheater power fraction as a function of reactor operation	131

Figure Number	Title	Page Number
3.3	Turbine runback when inlet valve is wide open and closes in 0.6 sec. - automatic actuation of by pass valve (equal percentage)	136
3.4	Turbine runback when inlet valve is wide open and closes in 0.6 sec - automatic actuation of by pass valve (linear)	137
3.5	Turbine trip when inlet valves are wide open - automatic actuation of by pass valve (equal percentage)	138
3.6	Turbine trip when inlet valves are wide open - automatic actuation of by pass valve	139
3.7	Reactor scram from 100 per cent power level with 10 dollars negative reactivity assumed in scram rods	145
3.8	Accidental by pass valve opening with no automatic pressure control	146
3.9	Pathfinder closed-loop frequency response	147
3.10	Linearized block diagram of reactor core dynamics	149
3.11	Control rod pattern for rod drop experiment	153
3.12	Location of data points for rod drop experiment	155
3.13	Schematic of electrical circuit for rod-drop experiment	158
3.14	Measurement of control-rod drop time	160

FOREWORD

This is the twelfth of a series of reports covering technical progress on the research and development program being performed in connection with the design of the Pathfinder Atomic Power Plant. This plant will be located at a site near Sioux Falls, South Dakota and is scheduled for operation in June 1962. Owners and operators of the plant will be the Northern States Power Company of Minneapolis, Minnesota.

The U.S. Atomic Energy Commission, through Contract No. AT(11-1)-589, with Northern States Power Company, and Central Utilities Atomic Power Associates*(CUAPA), are sponsors of the research and development program.

Allis-Chalmers Manufacturing Company of Milwaukee, Wisconsin, under contract with Northern States Power Company, is performing the research, development, and design; and will construct the plant including the reactor, which is designated the Controlled Recirculation Boiling Reactor (CRBR) with Nuclear Superheater. Pioneer Service and Engineering Company of Chicago, Illinois is providing the architect-engineer services to Allis-Chalmers. Portions of the R & D program, particularly in connection with fuel development, have been subcontracted by Allis-Chalmers.

Conceptual engineering and component research and development is well under way at Allis-Chalmers Greendale Laboratories. Erection of a number of major experimental facilities, which will provide important design data, has been completed. A Critical Experiment Facility was constructed and is now in operation.

---

*CUAPA Member Companies:

Central Electric and Gas Company
Interstate Power Company
Iowa Power and Light Company
Iowa South Utilities Company
Madison Gas and Electric Company
Northern States Power Company
Northwestern Public Service Co.
Otter-Tail Power Company
St. Joseph Light and Power Co.
Wisconsin Public Service Corp.

DESIGN DATA

CRBR WITH NUCLEAR SUPERHEATER

Plant

Power, boiler region	157,200 kw
Power, superheater region	42,400 kw
Steam flow at rated power	616,125 lbs/hr
Total core power	199,600 kw
Gross electrical capability	66,000 kw
Net electrical output	62,000 kw
Net efficiency	31.0 per cent
Steam outlet pressure	535 psig
Reactor operating pressure	600 psig
Temperature, boiler region	489 F
Outlet temperature, superheater region	825 F
Gross heat rate	10,199 Btu/kw-hr
Reactor building size	50 ft dia x 120 ft

Reactor

Vessel size (overall)	11 ft 6 in o.d. 36 ft 1 in
Total core dimensions	6 ft x 6 ft
Dimensions of superheater region	6 ft x 30 in
Fuel, boiler (Zr clad)	approx. 2.2 per cent enriched UO_2
Fuel, superheater (S.S. clad)	approx. 93 per cent enriched UO_2
Fuel, loading, boiler (U-235)	145.6 kg
Fuel, loading, superheater (U-235)	42 kg
Power density (boiler core coolant)	87 kw/liter
Average heat flux, boiler region	128,000 Btu/hr-ft^2
Average heat flux, superheater region	77,800 Btu/hr-ft^2
Maximum heat flux, boiler region	462,000 Btu/hr-ft^2
Maximum heat flux, superheater region	245,000 Btu/hr-ft^2
Recirculation rate	60,000 gpm
Recirculation pump power	794 kw
Neutron flux	approx. 5×10^{13} n/cm^2-sec

1. FUEL ELEMENT RESEARCH AND DEVELOPMENT

1.1 FUEL MATERIAL CLADDING, BONDING, AND IRRADIATION TESTING

The objectives of this project are as follows: 1) to perform investigations and experimental work regarding fuel compacts, cladding materials, processes for bonding, welding and sealing of fuel compacts leading to the development of improved and reliable fuel elements for the Pathfinder reactor; and 2) to determine the feasibility and practicability of manufacturing boiler and superheater fuel according to conceptual design specifications.

1.1.1 CLADDING

1.1.1.1 Steam Corrosion-Erosion Test of Stainless Steels. Description of Test Loop. A schematic of the equipment and fluid flow for the steam corrosion-erosion test was shown in the last quarterly report.[1] Superheated steam at 850 psig and 710 F passes through a controlled column of water in the loop to reach saturation at 600 psig and 489 F.

The saturated steam passes downward over three sample stations. The top station contains a nest of three concentric tubes each of a different stainless steel grade. The bottom station contains a radioactive specimen of type 316 stainless steel. The middle station contains a duplicate of the bottom specimen except that it is not radioactive. The method in which the radioactive specimen is mounted within the test section is shown in Figure 1.1.

Specimens in the top and middle station are used to compare corrosion-erosion resistance of various grades of stainless steel by conventional weight measurements and electrolytic stripping techniques.

---

1. "Pathfinder Atomic Power Plant, Technical Progress Report, April 1960 - June 1960", Fig. 1.5, Allis-Chalmers Report No. ACNP-6007, October 15, 1960.

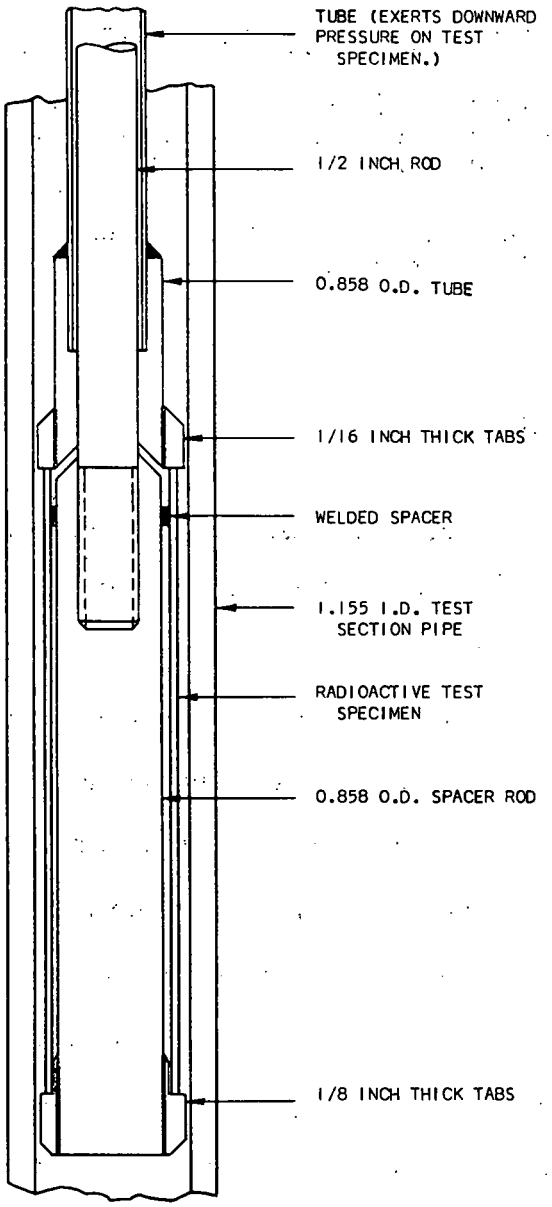

Figure I.1 Test section containing radioactive sample. (A-C Dwg. 43-024-346)

These results are compared with those obtained by radioactive tracer techniques, which are used for the irradiated specimen.

Out of consideration for the radioactive hazards involved, various safety devices are included in the test set-up. The particle trap downstream from the filter is a safety precaution to catch any large radioactive particle that may accidentally be dislodged from the radioactive sample and pierce the filter. Two fiber glass filters are used in series to check filter efficiency for radioactive particles. A differential pressure switch is installed across the filters to close off the steam supply should the pressure drop indicate filter break-through. Excessive pressure in the filter vessel also closes off the steam supply. The sump in the purifier is monitored continuously and the presence of activity shuts down the loop.

Calibration. A 1-in o.d. by 4-3/4-in long piece of type 316 stainless steel tubing was irradiated at Argonne National Laboratory to 2.6×10^{19} nvt. A 1/4-in long section from the same tube was irradiated at the same time.

The short section was placed in the lucite drilling fixture shown in Figure 1.2. Pieces of drillings from the section were then weighed on a microbalance and placed between 3/8-in thick by 2-in dia. aluminum disks. Individual pieces of drillings were placed in prick-punch impressions in disks and cover disks were cemented in place. The periphery of the disks were then sealed with tape.

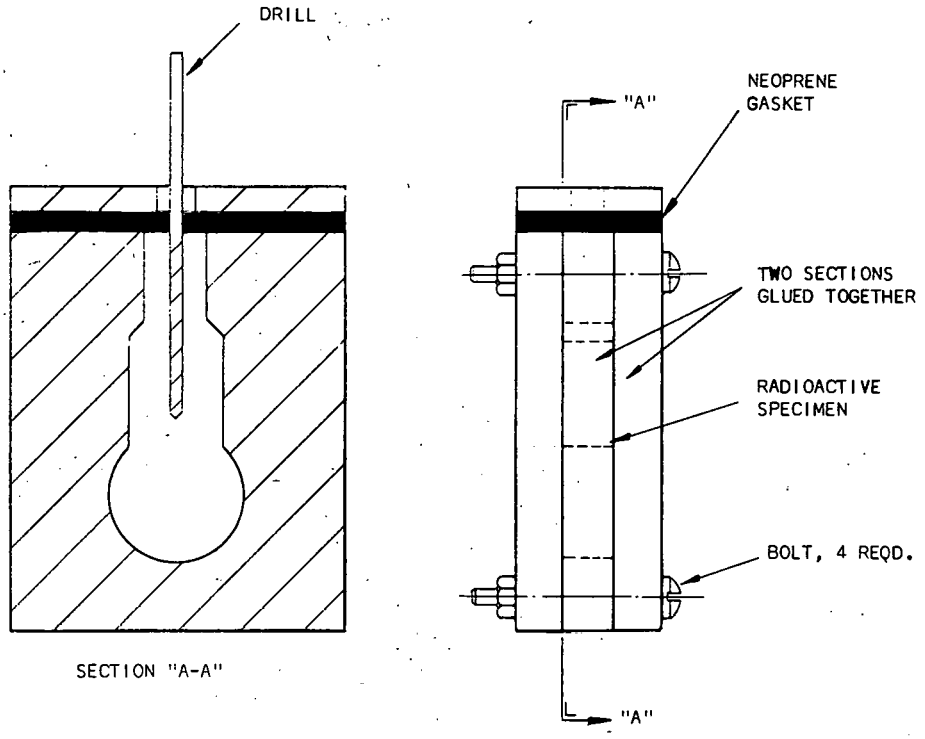

Figure 1.2 Drilling fixture for preparing calibration standards for superheater corrosion-erosion test. (A-C Dwg. 43-024-347).

Aluminum was selected as the disk material since it has essentially the same density as the melted fiber glass filter material in which the radioactive corrosion-erosion products will be embedded after the filter is reduced.

A gross gamma count was made of each standard specimen and the results are plotted in Figure 1.3. Using this data, the gross weight of stainless steel corrosion product collected by the filters can be estimated.

A plot of the gamma spectrum for each standard sample is also being prepared. By comparing the gamma spectrum of the corrosion-erosion products with the spectra of the various standards, an estimate of the selective retention or release of various nuclides can be made.

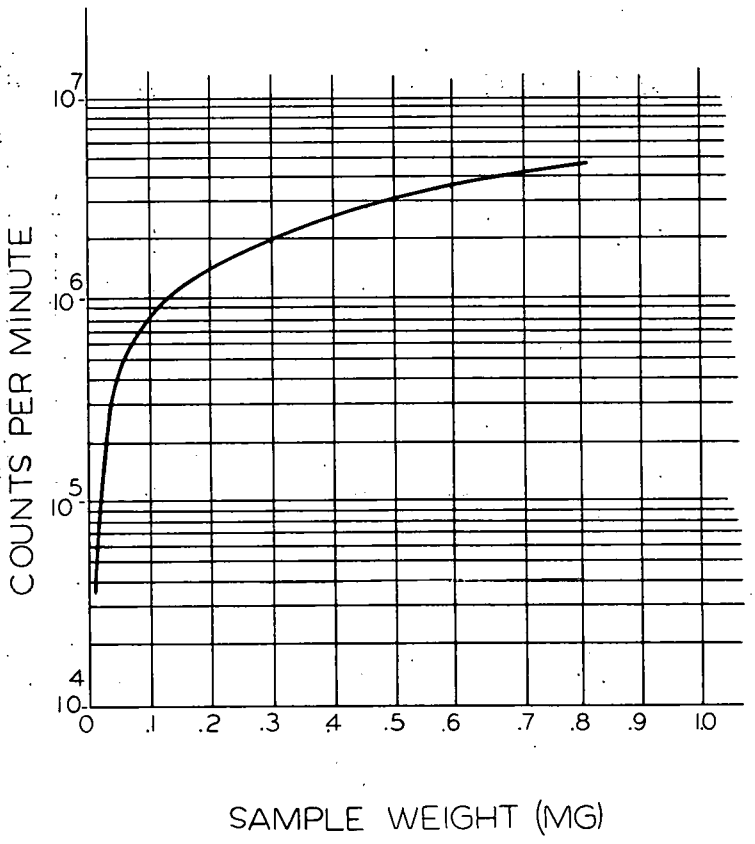

Figure 1.3 Count as a function of weight of radioactive sample. (A-C Dwg. 43-024-342).

1.1.2 IRRADIATION STUDIES

1.1.2.1 Capsule Irradiation Tests. Summary. A summary of results of irradiation tests of aluminum clad fuel is given in Table 1.1. Since visual examination of Capsule 2 and 3 showed sufficient damage to make further irradiation inadvisable, Capsule 1 was removed before the scheduled 15,000-MWD/T burnup. A post-irradiation examination is being made and will be completed shortly. A complete analysis of data will be presented in the next quarterly report. Results thus far are given in the following paragraphs.

Visual Post-Irradiation Examination of Fuel Specimens. Visual examination of fuel specimens in Capsule 2 revealed the following. The 6-percent enriched specimen had a combination longitudinal crack and bulge in the clad with a deposit of crud around the bulge.

Table 1.1 Capsule Irradiation Test Results

Capsule Number	Removal Date	Estimated Maximum Heat Flux (BTU/hr-ft^2)	Maximum Clad Temperature (F)	Estimated Burn-up (MWD/T)
1	July 25, 1960	500,000	525	12,000
2	May 16, 1960	500,000	500	8,900
3	June 20, 1960	700,000	800	10,300

(The crud deposit probably resulted from NaK bleed-out from the crack while leaching the NaK with alcohol.) A small longitudinal crack was found in the clad of the 7-percent enriched specimen. A local reaction took place at points where a thermocouple tip had been in contact with the clad. The result was a depressed area in the clad at the point of contact.

Visual examination of the fuel specimens in Capsule 3 revealed the following. The fission gas space in the 6- and 7-percent enriched specimens had collapsed. The surface of the aluminum clad had been attacked by the NaK at the high temperatures and showed considerable corrosion and some loss of aluminum metal. The thermocouple contact points appeared as depressed areas in the cladding and one tip had completely penetrated the cladding wall.

Visual examination of fuel specimens in Capsule 1 showed no defects. The specimens were in very good condition.

Gamma Scan. Gamma scans were made of all fuel specimens before sectioning. The scans indicated the presence of cracks, gaps, fuel redistribution, and changes in fuel length. The scan indicated gaps from 0.030 to 0.050 in. between fuel pellets in Capsule 1 and 2. The scan indicated gross cracking of fuel within Capsule 3 so that pellet boundaries could not be distinguished. The results of the gamma scan will be verified or discounted by physical measurements, which will be made during the next quarter.

Sectioning. A longitudinal section of the 7-per cent specimen in Capsule 3, which experienced the highest temperature, showed no center void; but considerable grain growth was observed. Appropriate samples are being polished for microanalysis and microphotographs. The results will be available next quarter.

1.2 HEAT TRANSFER AND FLUID FLOW

The objectives of this project are as follows: 1) to experimentally determine the actual heat transfer and fluid flow characteristics of the boiler fuel elements so as to establish and improve performance under conditions of high velocity two-phase flow; and 2) to experimentally determine the actual heat transfer and fluid flow characteristics of the high enrichment superheater fuel elements.

1.2.1 HEAT TRANSFER LOOP

A 450-kw motor-generator set was installed and tested under load. The set performed satisfactorily and was used for all tests conducted in the heat transfer loop during the quarter.

A schematic diagram of the heat transfer loop is shown in Figure 1.4. A low-flow recirculation pump was received and installed during the quarter. This pump is operating satisfactorily. A new seal was installed in the high-flow recirculation pump. This pump has since operated frequently at 615 psia saturated without failure. The cement base for the motor, gearbox, and 1800-kw Unipolar generators was rebuilt to eliminate vibration. The motor and gearbox were installed.

1.2.2 BOILER FUEL ELEMENT

1.2.2.1 10-8-6-Pin Test Section. Four tests, which required a total of 80 hr, were conducted on the 10-8-6-pin test section. These tests are described in the following paragraphs.

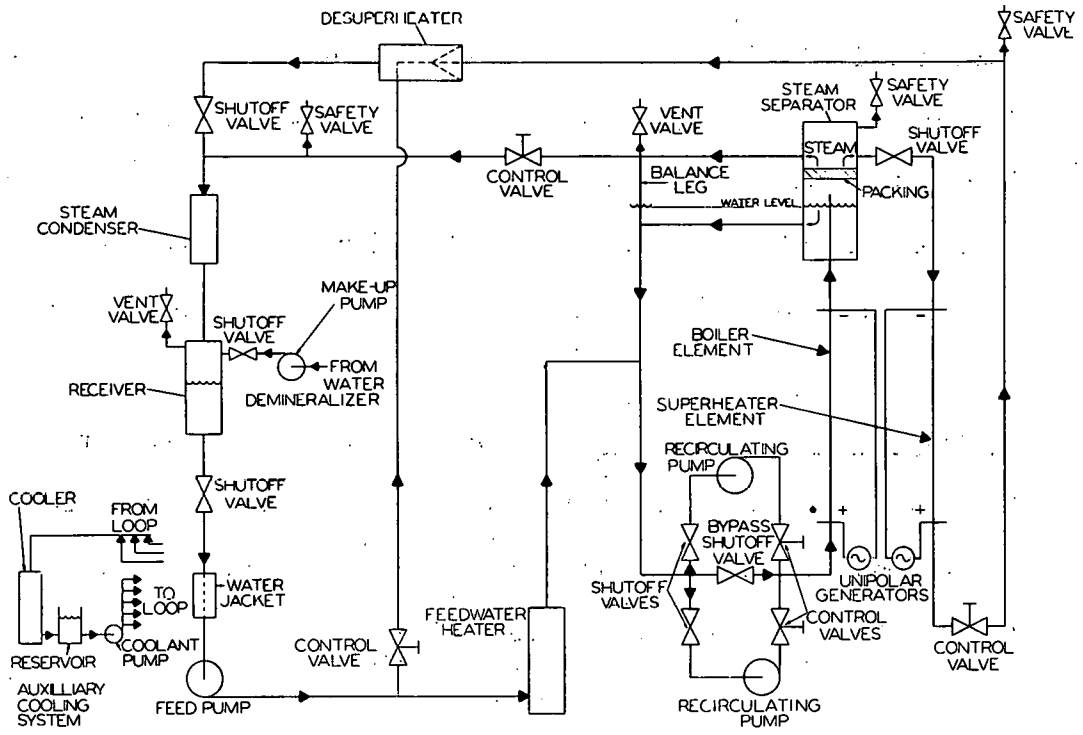

Figure 1.4 Schematic of heat transfer loop. (A-C Dwg. 43-400-935).

Calibration of thermocouples. The water thermocouples were calibrated by comparing them against saturation temperatures at various loop temperatures. The thermocouples were found to be accurate within the specified limits of $\pm$ 0.75 per cent.

Calibration of Orifice in Low-Flow Recirculation Loop. The low-flow loop orifice was calibrated by using a weigh tank, and values were then compared with those obtained with the Gentile flow meter. The orifice gave values 2 per cent higher than the flow meter.

Heat Balance Tests. A heat balance test was conducted and results show a consistent 9 to 11 per cent loss of heat from the test section. This was not acceptable, and no method of accounting for or correcting this loss could be found. All the loop instrumentation pertaining to the heat balance was rechecked, and no inaccuracies were found.

Isothermal Pressure-Drop Tests. Data from the isothermal pressure-drop tests were compared with data taken the previous quarter. Results were 5 per cent lower than previous experimental data, and 15 per cent lower than calculated values.

Conclusions. The unacceptable heat balance, change in pressure drop, and indications of an electrical insulation break-down prompted a decision to disassemble the test section. Examination showed heavy crud deposit on the heating rods. The rods were slightly pitted, and sides of the box were heavily pitted. Several silver-solder joints had failed, and surface-temperature thermocouples had broken away from the rods. The test section will be cleaned, repaired, and reassembled, without the surface-temperature thermocouples. After this is completed, further heat-loss and pressure-drop tests will be conducted.

1.2.2.2 Full-Scale Boiler Test Section. The Pathfinder boiler fuel element was redesigned (see Section 1.4), and the full-scale boiler test section (81-64-pin) was redesigned with 81 stepped tubes. The test section is shown in Figure 1.5. All material was ordered.

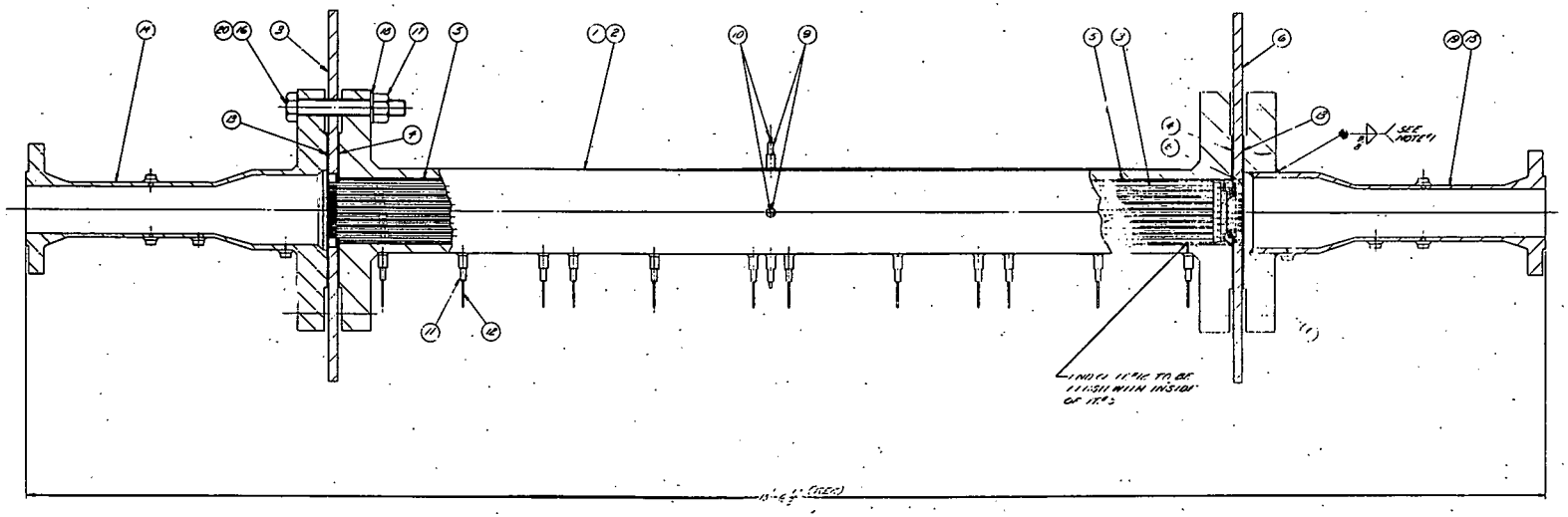

Figure 1.5 Boiler element mock-up assembly. Code: 2) boiler container assembly; 3) bundle assembly; 5) liner assembly; 6) bottom electrode; 9) centering fitting; 10) centering rod assembly; and 12) pressure tap. (A-C Dwg. 43-500-885)

1.2.2.3 One-Pin Burn-Out Tests. No one-pin burn-out tests were conducted during the quarter. Tests will be conducted during the next quarter as soon as tests with the superheater test section are complete (see Section 1.2.3). Multi-point, millivolt recorder will be installed to determine burnout heat fluxes and maximum rod temperatures.

1.2.2.4 Low-Pressure Air-Water Test. Void-fraction measurements of the boiler subassembly were completed. Data is now being analyzed.

Further investigation of the gamma-ray attenuation method of measuring void fraction is being made with an aluminum-lucite-air mockup of the subassembly. The object of this investigation is as follows: 1) to investigate the non-exponential attenuation of gamma rays in regions of abrupt geometry changes; 2) to check experimental values obtained with annular flow model against calculated values and adjust the air-water void fraction data accordingly; and 3) to check the assumption that constant absorption coefficient holds for the geometry used in obtaining air-water void-fraction data.

The model used for these tests is shown in Figure 1.6. Aluminum tubes were set in a lucite block, and lucite tubes of two outside diameters were pressed over the aluminum tubes. The lucite will simulate water, since their gamma absorption coefficients are nearly the same. The model is constructed to simulate a theoretical annular flow pattern for two average void fractions.

A series of tests were conducted, and data is now being analyzed.

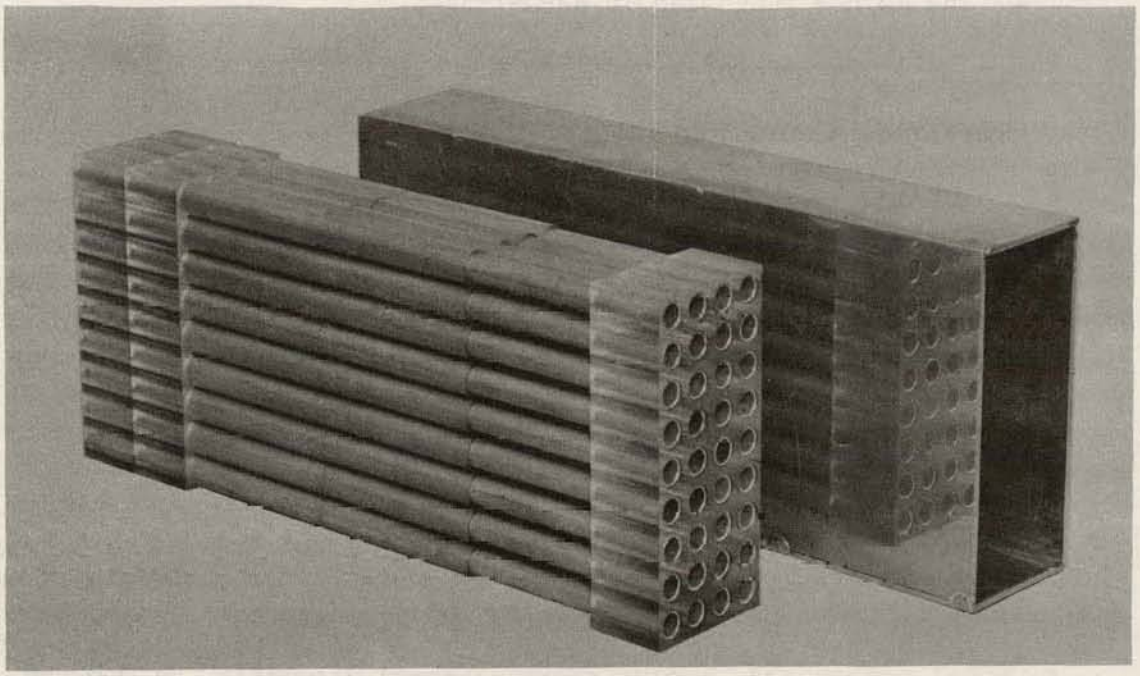

Figure 1.6 Aluminum-lucite subassembly mockup. (A-C Photo 211021)

1.2.2.5 Boiler Hydraulic Analysis. Coincident with the changes in the design of the boiler fuel element, the methods and correlations used for computing the flow-pressure-drop relations were completely reviewed. As a result of this review, the following procedures were established:

1) the Martinelli-Nelson correlation with the Sher mass-flow rate correction recommended in ANL-6063 is used to predict two-phase frictional pressure-drop multipliers;

2) two phase form losses are predicted from single-phase theory, and loss coefficients are predicted using the specific volume of a homogeneous, two-phase mixture;

3) void fractions are predicted by the modified Martinelli correlations in the bulk boiling region and are assumed to be zero in the sub-cooled nucleate boiling region;

4) Sub-cooled, nucleate boiling friction factors are based on the method presented in WAPD-T-844;

5) burnout predictions are based upon the correlations presented in WAPD-188.

These procedures will be continually reviewed as new data both from Greendale and other laboratories become available; and modifications will be incorporated as necessary. The pressure drop predicted for the Pathfinder boiler fuel element is nominally 11.8 psi on the following basis:

1)	boiler exit pressure	615 psia
2)	power	159.8 mw
3)	power distribution -- lower half	65 per cent
	-- upper half	35 per cent
4)	active (fuel element) flow rate	54,000 gpm
5)	inlet temperature	485.4 F

This pressure drop included the losses from just below the bottom fuel pin grid plate to above the top end bracket. The pressure drop from just below the boiler grid plate to just below the lower fuel pin grid plate is 1.8 psi for the same flow rate (54,000 gpm). This gives a fuel element plus nozzle pressure drop of 13.6 psi. A detailed list of the calculated pressure drops is given in Table 1.2; the flow uncertainty is estimated to be 10 per cent.

1.2.3 SUPERHEATER FUEL ELEMENT

1.2.3.1 Partial Power and Partial Pressure Operation. During start-up the Pathfinder reactor operates at partial power and pressure. The superheater fuel element performance in this operating region was investigated. A program was formulated making use of the IBM-704 code STER (formerly referred to as ASTER). It was assumed that

TABLE 1.2 BOILER PRESSURE DROPS

Position	Static Pressure (psia)				
	minimum pressure at minimum flow	minimum pressure at nominal flow	nominal pressure at nominal flow	maximum pressure at nominal flow	maximum pressure at maximum flow
just below reactor grid plate	624.0	625.6	628.6	631.5	634.2
just below lower fuel rod grid plate	622.8	624.2	626.8	630.9	633.9
just above lower fuel rod grid plate	622.0	623.2	625.6	629.2	632.0
just below first tube sheet	620.9	622.0	624.2	627.4	629.7
just above first tube sheet	620.5	621.5	623.6	626.6	628.8
just below second tube sheet	619.2	620.0	621.7	624.1	625.7
just above second tube sheet	618.8	619.5	621.0	623.3	624.6
just below third tube sheet	617,8	618.4	619.5	621.1	622.2
just above third tube sheet	617.2	617.9	618.5	619.8	620.6
just below upper fuel rod grid plate	616.2	616.5	616.9	617.6	618.0
just above upper fuel rod grid plate	616.0	616.2	616.6	617.2	617.6
just above upper end fitting	615.0	615.0	615.0	615.0	615.0
between boxes just above reactor grid plate			617.6		
between boxes just above lower fuel rod grid plate			617.2		
control rod channel just above stub with rod inserted			621.2		
control rod channel just above stub with rod withdrawn			618.1		

the power distribution between sensible, latent, and superheat remained constant for all powers and pressures. Pressures of 100, 200, 300, 400, 500, and 615 psia at 25, 50, and 100 per cent of rated reactor power were investigated. A consistent set of hot-spot factors (no manufacturing factors) was used. Results of this study are presented in Figures 1.7 and 1.8. It is seen that the maximum wall temperature decreases with decreased power but increases with decreased operating pressure. It also should be noted that at low operating pressures core pressure drops increase very rapidly with reactor power.

1.2.3.2 Analysis of Fuel Element Tolerances. The effect of dimensional variations from the nominal case on fuel element performance was investigated to determine tolerances that would be required during manufacture. The performance of the concentric tube element is extremely sensitive to dimensional changes. The following dimensions are being analyzed:

1) i.d. of inner insulating tube
2) i.d. of fuel tubes
3) o.d. of poison rod
4) wall thickness of fuel tubes
5) tube assembly clearance
6) diameter of spacer wire
7) element insertion clearance

Because the tubes are spaced by three parallel wires, it is possible that the accumulation of tolerances and clearance will lead to an eccentric fuel element where the minimum flow area gap is less than the spacer wire diameter. Results of this analysis will be reported during the next quarterly.

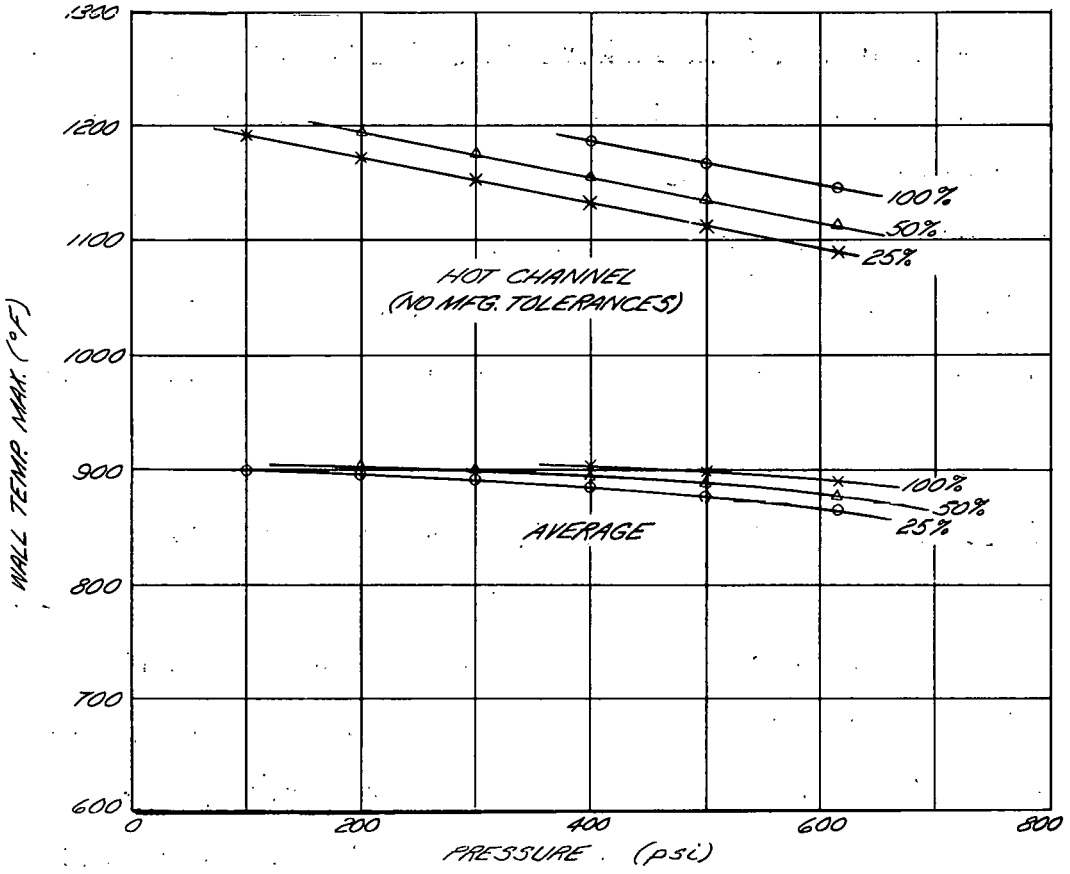

Figure 1.7 Maximum wall temperatures at partial and full power and pressure. (A-C Dwg. 43-024-337).

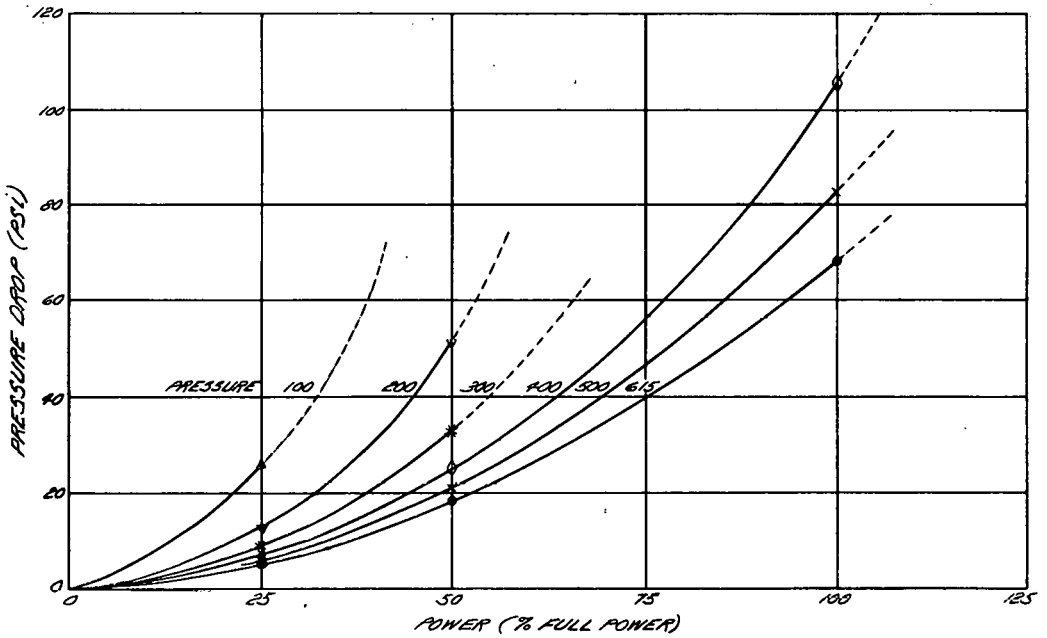

Figure 1.8 Pressure drop through core at partial power and pressure. (A-C Dwg. 43-024-338)

1.2.3.3 Heat Transfer Loop Superheater Tests. Shakedown tests of the superheater test section will begin as soon as the steam generator can be fabricated and installed in the boiler loop. During shakedown, steam will be superheated by a dummy test section, which has been installed. After shakedown is completed, the concentric-tube superheater test section will be installed, and a testing program will be initiated.

1.2.3.4 Superheater After-Glow Test. A superheater afterglow test was designed to test the superheater tube temperature level as a function of decay-heat power level under stagnant steam conditions. The test section was assembled and is ready to install in the pressure vessel. The testing will be performed under operating conditions of 489 F at 600 psi with up to 4 kw of heat to a mockup of a single superheater fuel element. The test is expected to be completed during the next quarter. The test section has been built without a poison rod or wire spacers to facilitate installation of thermocouples.

1.4 FUEL ELEMENT MANUFACTURING RESEARCH AND DEVELOPMENT

The objective of this project is to perform calculations and studies of methods for producing core subassemblies to determine the most economical manufacturing methods and to obtain maximum performance.

1.4.1 BOILER FUEL ELEMENT BOXES

A quad box (Figure 1.9) was designed to contain four boiler fuel elements and a closed control rod channel; and a simpler box was designed to contain one boiler fuel element only. These boxes are semi-permanent parts of the reactor core and are designated as reference for Pathfinder. They replace the individual boxes which had been included in the design of the boiler fuel element. The redesign of the boiler fuel element is described in Section 1.4.2.

The bottom of the quad box is formed by a 1-1/2-in thick plate. The control rod stub is welded to the top of the plate and extends into the control rod channel. A 2-in dia. nozzle is partially inserted and welded into the center of the bottom of the plate. In addition to locating the quad box in the boiler grid plate, the nozzle provides coolant from the lower coolant inlet plenum through slots in its upper end to a cruciform plenum in the bottom of the box bottom plate. The coolant passes from the cruciform plenum through orifice holes in the plate and control rod stub to the control-rod coolant channel. The coolant passes over the control rod and out through slots in the upper wall of the cruciform control rod channel.

The bottom of the box has four holes in which boiler fuel element nozzles are seated. The box is held down by the weight of the boiler fuel elements and the upper hold down structure.

The single boxes have a simple bottom plate that accommodates the boiler fuel element nozzle. These boxes are semi-permanent structures that will be installed in the thirty-two fuel-element positions which are not immediately adjacent to a control rod.

This redesign of the fuel element box, which was made without changing the core layout, was necessary to provide adequate coolant to the control rods. With this design, the flow to each control rod is controlled by the size of the holes in the control rod stub, which accounts for about 75 per cent of the total flow resistance.

Preliminary calculations have indicated that twenty-five 0.25-in i.d. holes are required in each control rod stub to deliver the necessary coolant with the rod inserted. The actual hole size will be established in a test with a simulated control-rod coolant circuit. Details of the preliminary calculations are given in Section 2.4.

Two alternate schemes for providing coolant to the control rod channel were also investigated. One method involved a large single nozzle with a transition piece that directed flow to the four fuel elements and the control rod channel. This method was not used because it left the fuel element springs unprotected from the high velocity flow. In addition, it was difficult to fasten the spring to a fuel element without a fuel element nozzle.

The second method studied consisted of a plate on the bottom of the four element box similar to that used in the present design except that four nozzles were attached to it. The nozzle on the fuel element would then seat within the box nozzles. This method was not used because of the difficulty of simultaneously inserting four nozzles into their respective sleeves in the grid plate.

1.4.1.2 Stress Analysis. Stresses in four-element boxes of various configurations were calculated. Strain energy methods were used to obtain the maximum bending moments acting on the box walls. The strain energy equations for deflection and rotation of a thin beam[2] are as follows:

$$\delta_Q = \frac{\partial U}{\partial Q} = \int \frac{M}{EI} \frac{\partial M}{\partial Q} dx \qquad (1.1)$$

$$\theta_C = \frac{\partial U}{\partial C} = \int \frac{M}{EI} \frac{\partial M}{\partial C} dx \qquad (1.2)$$

where,

δ_Q = deflection at load, Q, in the direction of the force, Q

M = bending moment at any point

θ_C = rotation of a section at the point of an applied couple, C

I = moment of inertia = $t^3/12$, where t = wall thickness.

Since the box sides act as thin wide beams, the modulus of elasticity, E, in Eq. (1.1, 1.2) should be replaced by the quantity,

$$\frac{E}{1 - \nu^2}$$

where ν is Poisson's ratio. At the curved corner of the box, dx is replaced by $Rd\theta$. Then, by applying the proper boundary conditions, to the deflections and rotations, the bending moments and stresses can be calculated at any point in the box wall.

The maximum stress occurs at the box corners and was calculated from the following equation for a curved beam[2]:

$$\sigma_{max} = \frac{P_N}{A} + \frac{M}{AR}\left(1 + \frac{I}{Z}\frac{Y}{R + Y}\right) \qquad (1.3)$$

---

2. Seely and Smith, "Advanced Mechanics of Materials," 1952

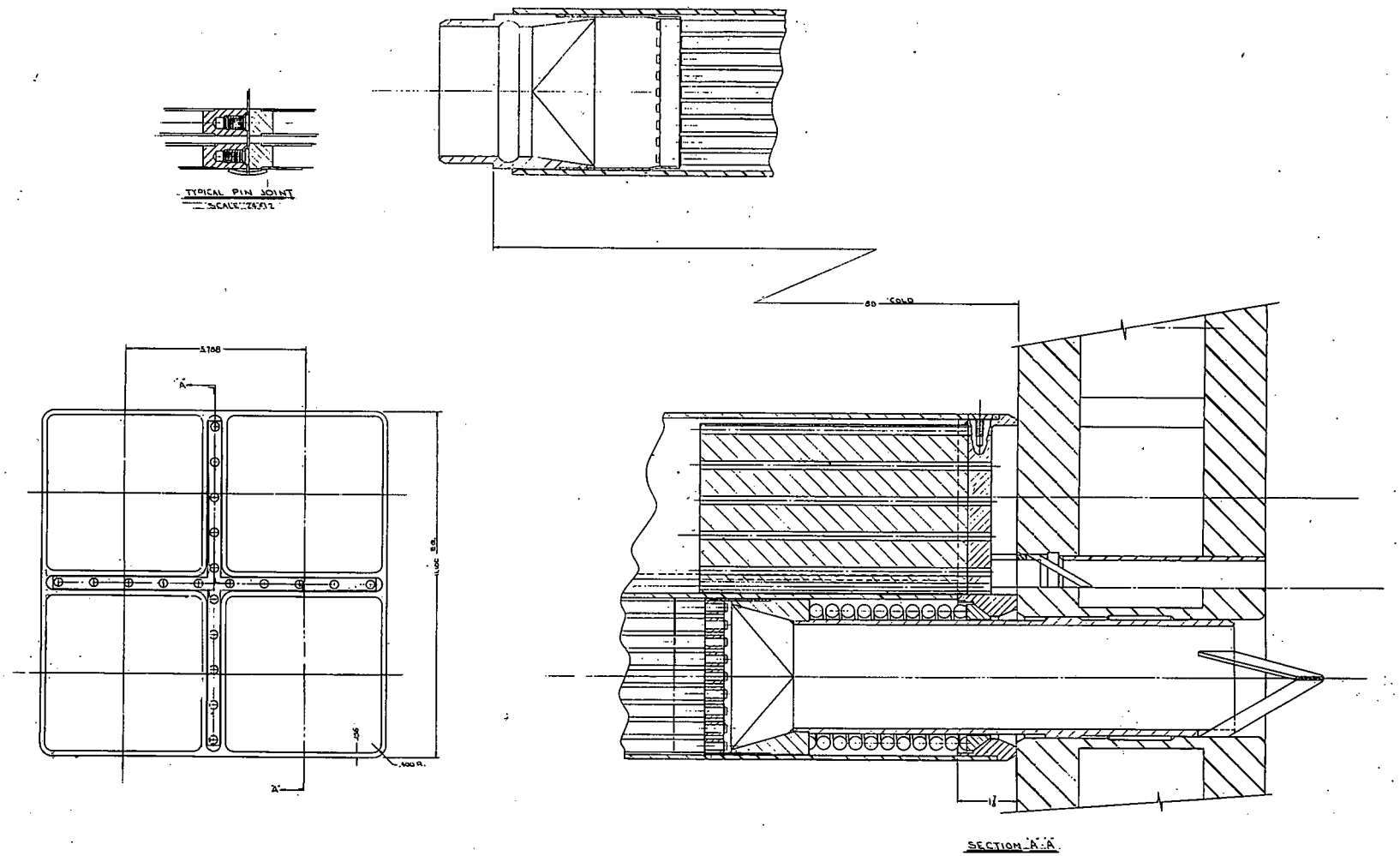

Figure 1.9 Flat-bottom four-element quad box with integral control rod stub. (A-C Dwg. 43-002-205)

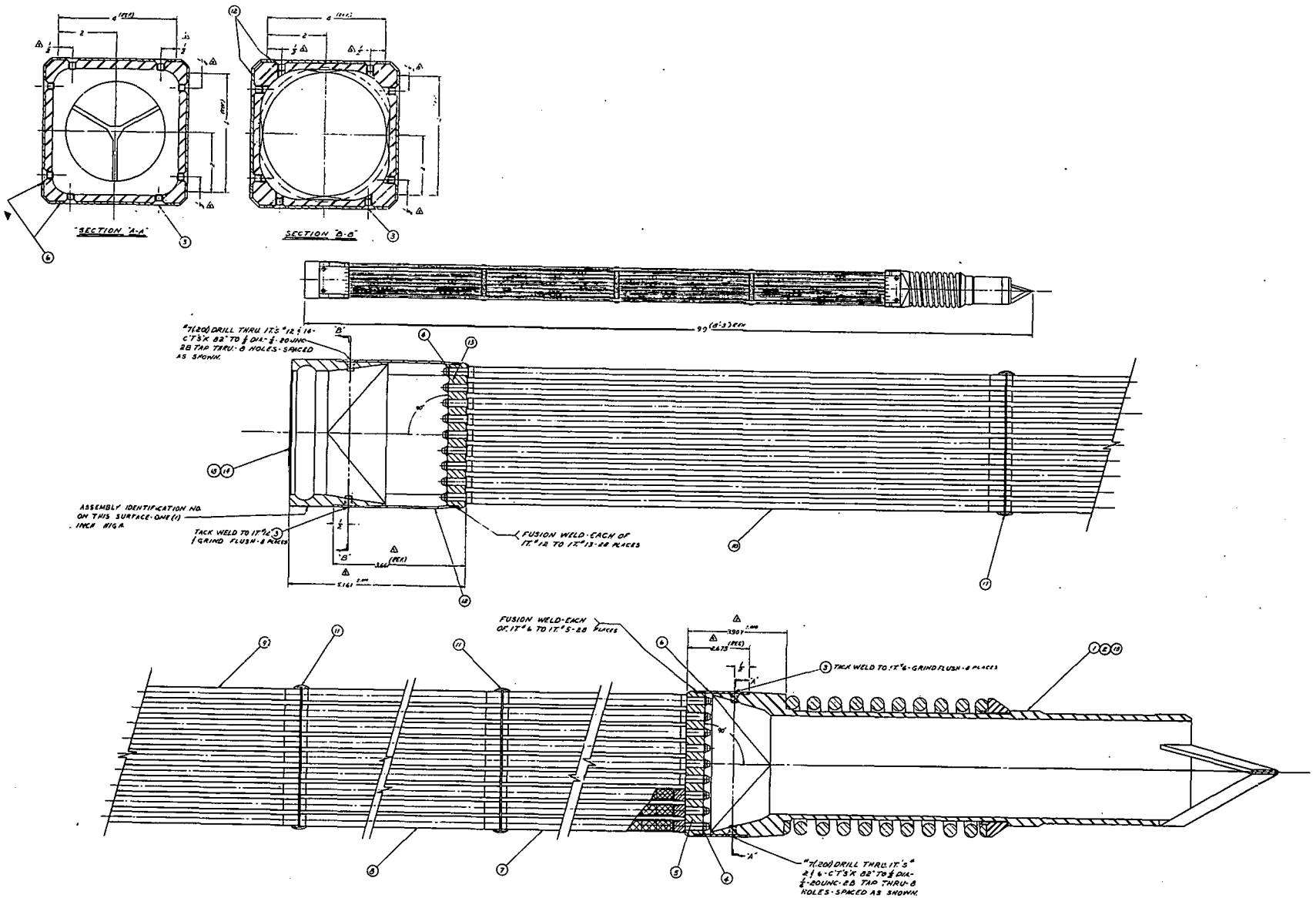

Figure 1.10 Step-Tube boiler fuel element assembly. Code: 1) nozzle assembly; 4) retaining ring; 5) fuel rod support grid; 6) bottom skirt 7, 8, 9, 10) fuel rod sections; 11) tube sheet assembly; 12) top skirt; 13) upper fuel rod support grid; 14) upper end fitting.
(A-C Dwg. 43-500-842)

where,

$$Z = \frac{1}{3}\left(\frac{C}{R}\right)^2 + \frac{1}{5}\left(\frac{C}{R}\right)^4 + \frac{1}{7}\left(\frac{C}{R}\right)^6 + \ldots$$

P_N = the normal force acting on the section

A = area of the unit width section = t

R = the mean radius of the corner

C = t/2, where t = wall thickness

Y = distance from centerline of wall

Calculations for a plain box 10.788 in. sq. inside and 0.150 in. thick wall with inside corners of 0.250 in. radius showed maximum stress at the inside corner caused by the 14.5 psi internal pressure to be 42,300 psi.

Calculations for a box of the same dimension with the center of each side fixed by a cross-bar showed maximum stress at the inside corner with 14.6 psi internal pressure to be 11,540 psi.

Calculations for the quad box with 12.6 psi in the fuel element sections and 0.8 psi in the control rod channel showed a maximum stress of 10,300 psi at one of the corners.

A Plexiglas model of the quad box is being fabricated and will be tested under internal pressure to verify the theoretical stress calculations. The deflection of the box walls will also be measured.

1.4.2 BOILER FUEL ELEMENT

1.4.2.1 Reference Design. Since the fuel element box was redesigned as a semipermanent part of the core, the boiler fuel element was redesigned accordingly. This fuel element is shown in Figure 1.10.

The general dimensions, spacing, supporting method, nozzle assembly, and upper end-fitting are essentially the same. However, the element now consists of a single fuel bundle in a 9 x 9 lattice. The fuel rod diameter is reduced (stepped) in the upper half to accommodate the increasing steam-void volume. This differs from the previously described design which included a 9 x 9 lattice bundle in the lower half and an 8 x 8 lattice bundle in the upper half.

Spacing between the inside of the semi-permanent box and the outer rows of fuel rods is maintained by skids that are part of the tube sheets. The fuel element nozzle is attached to a skirt that is welded to the bottom fuel-tube grid plate. Bosses in the corners of the upper fuel-tube grid plate concentrate axial compressive loads in the four corner fuel rods. The remaining fuel rods are free to move axially precluding distortion due to differential thermal expansion between fuel rods.

1.4.2.2 Fabrication. Fabrication continued on the Pathfinder boiler prototype element and the boiler qualification rods described in the previous quarterly report.

1.4.2.3 Mechanical Design Analysis. Compressive Load on Corner Boiler Fuel Rods. A compressive load is placed on the four corner fuel rods by the fuel element nozzle spring and by the upward hydraulic force of recirculating water. This force is calculated to be 110 lb/rod.

Two methods of failure were considered: elastic failure due to direct compression of the fuel rod; and inelastic failure or buckling.

The compressive stress was calculated to be 3820 psi, and the elastic failure is therefore no problem.

The corner fuel rod may be considered as an intermediate column since the minimum slenderness ratio of the upper half of the rod is 50.3. The critical load for inelastic failure was therefore calculated by the tangent modulus theory,

$$P_T = \frac{\pi^2 E_T A}{(l/r)^2} \qquad (1.4)$$

where,

P_T = maximum load under which an ideal column will not bend;

E_T = tangent modulus

A = minimum cross sectional area of fuel rod cladding

l/r = slenderness ratio

The tangent modulus was determined as shown in Figure 1.11.

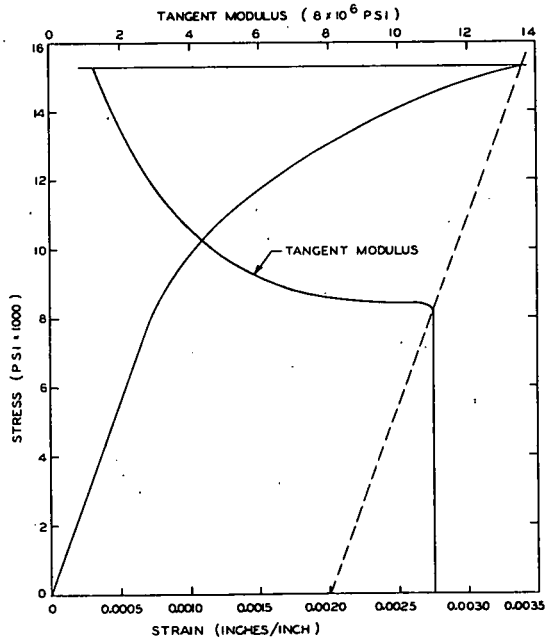

Figure 1.11 Stress-strain curve for Zircaloy-2 at 600 F. (A-C Dwg. 43-024-364)

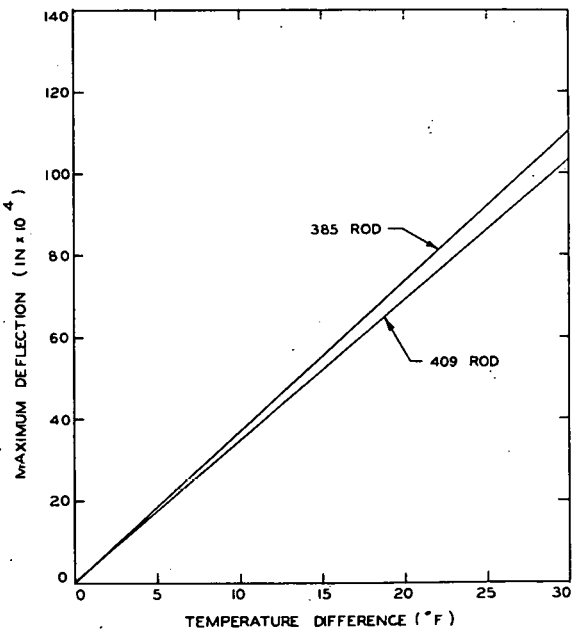

Figure 1.12 Boiler fuel-rod thermal bowing. (A-C Dwg. 43-024-365)

Through trial and error, the critical load was calculated to be 340 lb/rod. Since the maximum load resulting from compressive loads is 110 lb/rod, the axial support provided by the four corner fuel rods is adequate.

Thermal Bowing. Thermal bowing of a fuel rod as a result of a difference in temperature across the fuel rod was calculated after making the follwing assumptions:

1) the temperature differential across the rod is linear,
2) the temperature difference along the length is constant,
3) the spacers act as a simple support and prevent deflection,
4) the deflection is small compared to the rod length.

The maximum deflection occurs at the midpoint between spacers and was calculated by the equation,

$$\delta = \frac{\alpha \Delta T L^2}{8d} \qquad (1.5)$$

where,

δ = deflection (in.)
α = coefficient of expansion for Zircaloy-2
ΔT = temperature difference across the rod (F)
L = length of rod (in.)
d = outside diameter of rod (in.)

Results of calculations are shown in Figure 1.12. Since heat-transfer calculations indicate that the maximum temperature difference would be 30 degrees, the bowing is not excessive.

Ovality in Fuel Rod Clad. Ovality in the cladding tube will be most restricted by a condition of high temperature (750 F) and high pressure (1600 psi) during autoclaving. Calculations were therefore made to determine the greatest ovality that can be permitted in the cladding tube.

The allowable ovality in the cladding tube was calculated using an equation given by R. G. Sturm:

$$\bar{W} = \frac{Z\bar{S}\left(\frac{t}{D}\right)}{1 + \frac{4A_o}{t}\,\frac{E\left(N^2 - 1 + \mu\frac{\pi^2 D^2}{L^2}\right)\left(\frac{t}{D}\right)^3}{(1-\mu^2)(W_c - \bar{W})}} \qquad (1.6)$$

where,

A_o = ovality = $\frac{\text{Max. i.d.} - \text{min. i.d.}}{2}$

E = Young's Modulus

D = average diameter = i.d. + t

L = length of cylinder

N = number of lobes

R = average radius

$\bar{S}$ = allowable total stress

t = wall thickness

$\bar{W}$ = allowable pressure on out-of-round tube

W_c = critical pressure for elastic failure = $\frac{ZE}{1-\mu^2}(t/D)^2$

μ = Poisson's ratio

From this equation, curves were plotted showing:

1) allowable pressure vs. ovality for different tubes at 750 F

2) allowable pressure vs. wall thickness for 0.353-in i.d. tube at 750 F

3) allowable pressure vs. wall thickness for 0.327-in i.d. tube at 750 F.

4) allowable pressure vs. wall thickness for 0.315-in i.d. tube at 750 F.

---

3. R. G. Sturm, "A Study of the Collapsing Pressure of Thin Walled Cylinders", Bulletin Series No. 329, University of Illinois Engineering Experiment Station.

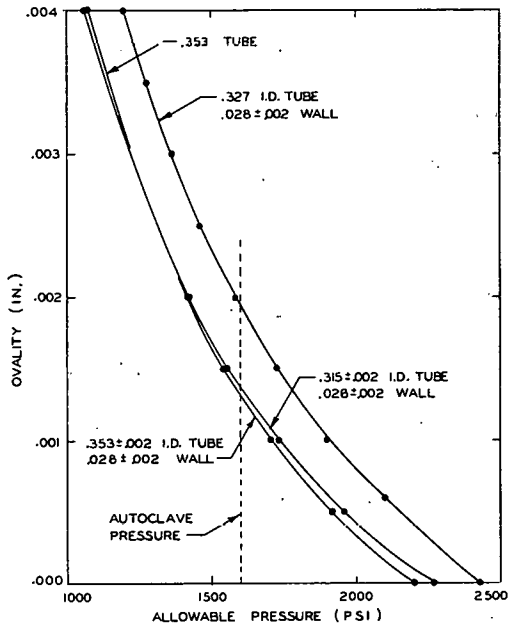

Figure 1.13 Fuel-rod-cladding allowable pressure vs. ovality at 750 F. (A-C Dwg. 43-024-363).

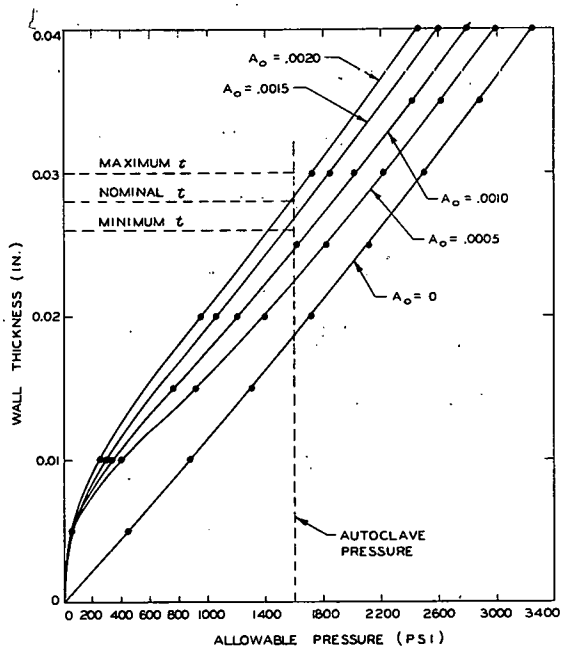

Figure 1.14 Allowable pressure vs. wall thickness for 0.353 i.d. tube at 750 F. (A-C Dwg. 43-024-367).

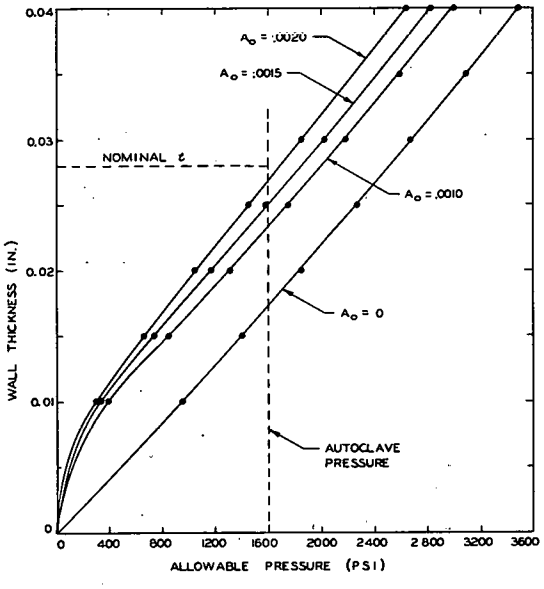

Figure 1.15 Allowable pressure vs. wall thickness for 0.327 i.d. tube at 750 F. (A-C Dwg. 43-024-366).

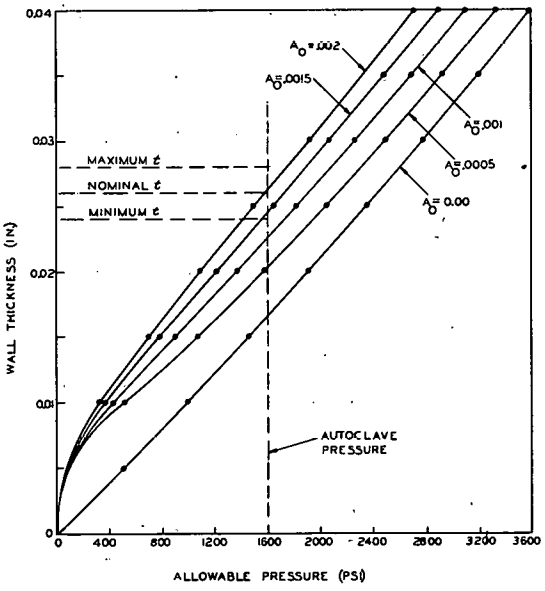

Figure 1.16 Allowable pressure vs. wall thickness for 0.315 i.d. tube at 750 F. (A-C Dwg. 43-024-368).

These results are given in Figures 1.13, 1.14, 1.15, and 1.16.

In view of the worst condition (1600 psi, 750 F), the curves show that the greatest permissible ovality, A_o, is 0.001 in., or 0.002 in. on the diameter.

Fuel Rod Dimensions. The required nominal operating dimensions of fuel rods were established from physics considerations and are given in Table 1.3. The dimensions to which fuel rods will be fabricated in order to meet this requirement were calculated and are also given in Table 1.3.

Table 1.3 Fuel Pellet Dimensions

	as-fabricated	nominal-operating
Upper half		
pellet diameter (in.)	.3235 ± .0005	.325
clad i.d. (in.)	.329 ± .002	.3295
wall thickness (in.)	.028 ± .002	.028
clad o.d. (in.)	.385 ± .006	.3855
density UO_2 (per cent)	95	93.5
Lower half		
pellet diameter (in.)	.348 ± .0005	.350
clad i.d. (in.)	.353 ± .002	.3536
wall thickness (in.)	.028 ± .002	.028
clad o.d. (in.)	.0409 ± .006	.4096
density UO_2 (per cent)	95	92.9

In calculating the fuel rod dimensions, it was necessary to determine the centerline temperatures of the fuel pellets. An equation, Eq. (1.9) to make this calculation was derived in the following manner.

An equation due to Taraba,[4]

$$T(r) = \frac{1}{K}\int_b^r \left[\frac{1}{r'}\int_0^{r'} r''\, S(r'')\, dr''\right] dr' + T_b \qquad (1.7)$$

where,

$T(r)$ = temperature as a function of radius (F)

K = coefficient of thermal expansion

$S(r'')$ = heat generation as a function of radius

T_b = temperature at surface of pellet (F)

b = outside radius of pellet (in.)

$0 \leq r = r' = r'' \leq b$

was taken at the outset. The heat generation, $S(r'')$ was included in Eq. 1.7 in terms of N and M as defined by the equation.

$$S(r) = Nr^2 + M \qquad (1.8)$$

where,

N,M = constants derived from the known normalized neutron flux distribution in the pellets

which assumed that heat generation was parabolic within the pellet. By making this substitution in Eq. 1.7, the equation

$$T(r) = \frac{1}{K}\left[\frac{N}{16}(b^4 - r^4) - \frac{M}{4}(b^2 - r^2)\right] + T_b \qquad (1.9)$$

was obtained.

---

4. Taraba, ANL 5873, p.8

In calculating the centerline temperature, it was further assumed that 38 per cent of the boiler power is generated in the upper half of the core and 62 per cent is generated in the lower half. The 38 per cent of boiler power means an average volumetric heat generation of 9630 Btu/hr-in^3 in the upper half; and the 62 per cent means an average volumetric heat generation of 13,750 Btu/hr-in^3 in the lower half.

The centerline temperature (T at r = 0) that was calculated for the upper half is 1282F. The centerline temperature for the lower half is 1825 F.

The equation for radial expansion of uranium dioxide fuel pellets was then derived in the following manner.

The equation,[5]

$$\epsilon_r = \frac{1}{E}\left[\sigma_r - \nu(\sigma_\theta - \sigma_z)\right] + \alpha T \qquad (1.10)$$

$$\sigma_r = \frac{\alpha E}{1-\nu}\left[\frac{1}{b^2}\int_0^b Tr\,dr - \frac{1}{r^2}\int_0^r Tr\,dr\right] \qquad (1.11)$$

was taken at the outset. No axial or radial restraint is assumed, i.e, $\sigma_\theta = 0$ and $\sigma_z = o$.

The equation for radial expansion,

$$\Delta r = \int_o^b \epsilon_r\,dr = \frac{\alpha}{24K(1-\nu)}\left[-\nu Nb^5 + Mb^3(3-4\nu) + 24bK(1-\nu)T_b\right] \qquad (1.12)$$

where,

b = radius of UO_2 pellet as fabricated

K = thermal conductivity in Btu/hr-in^2 F/in.

---

5. Timoshenko, "Theory of Elasticity", pp. 408-410

may be derived from Eqs. (1.9, 1.10, 1.11). The as-fabricated pellet diameter for the upper and lower sections were then calculated by Eq. 1.12 from the required nominal operating diameters of fuel.

In order to calculate the change in apparent density of uranium dioxide from the as-fabricated to the nominal-operating density, it was necessary to calculate the axial expansion, in addition to the radial expansion. This calculation was made with the equation,[6]

$$\Delta L = L_o (1 + \nu)\alpha T_E - 2\nu\alpha T_{ave} - \alpha T_R \qquad (1.13)$$

where,

ΔL = axial expansion (in.)

L_o = original length (in.)

ν = Poisson's ratio

α = thermal coefficient of expansion

T_E = centerline temperature

T_{ave} = average temperature

T_R = room temperature.

Results obtained with this equation agreed well with data on dimensional behavior of uranium dioxide at high temperature reported by W. R. Martin[7].

---

6. WAPD-RDa-7

7. W. R. Martin and J. R. Weir, "Dimensional Behavior of UO_2 at High Temperature", US/UK Research Newsletter No. 9, June 1960

Cladding Stresses. A summary of stresses in the cladding is given in Table I.4. The thermal stresses were calculated by the equations,[8]

$$\sigma_a = \frac{E\,\alpha}{2(1-\nu)} \times f_2(t_b - t_a) \qquad (I.14)$$

$$\sigma_b = \frac{E\,\alpha}{2(1-\nu)} \times f_3(t_b - t_a) \qquad (I.15)$$

where, σ_a = inside stress

σ_b = outside stress

E = Young's Modulus

ν = Poisson's Ratio

f_2, F_3 = constants

t_b = temperature outside

t_a = temperature inside

Pressure stresses were calculated according to Lamé's solution for stresses due to internal pressure:

$$\sigma_t = \frac{P_1 a^2 - P_2 b^2 + \frac{a^2 b^2}{\rho^2}(P_1 - P_2)}{b^2 - a^2} \qquad (I.16)$$

$$\sigma_z = \frac{P_1 a^2 - P_2 b^2}{b^2 - a^2} \qquad (I.17)$$

where, σ_t = tangential stress at $r = \rho$

σ_z = axial stress

P_1 = internal pressure

P_2 = external pressure

a = inside radius

b = outside radius

ρ = radius at which stress is calculated, $a \leq \rho \leq b$

8. H. Etherington, "Nuclear Engineering Handbook," p. 1-61, McGraw-Hill Book Co., 1958

TABLE 1.4 SUMMARY OF CLADDING STRESSES (END EFFECTS NOT INCLUDED)

CASE I TEMPERATURES AVERAGED OVER HALF OF CORE (AXIALLY) BASED ON NEW CLEAN POWER DISTRIBUTION (ALL RODS OUT).

CASE II TEMPERATURES AVERAGED OVER SINGLE TUBE FOR MAX. AXIAL POWER AND MAX. RADIAL POWER (NO ENGR. HOT CHANNEL FACTORS).

CASE III TEMPERATURES AVERAGED OVER SINGLE TUBE FOR MAX. AXIAL POWER AND MAX. RADIAL POWER (WITH ENGR. HOT CHANNEL FACTORS)

	MINIMUM WALL			NOMINAL WALL			MAXIMUM WALL		
	MIN. ID	NOM. ID	MAX. ID	MIN. ID	NOM. ID	MAX. ID	MIN. ID	NOM. ID	MAX. ID
LOWER HALF									
I.D.	.3516	.3536	.3556	.3516	.3536	.3556	.3516	.3536	.3556
O.D.	.4036	.4056	.4076	.4076	.4096	.4116	.4116	.4136	4156
CASE I $Q/A = 12\ K\ \Delta T/(a\ \ln\ b/a) = 175{,}200$ BTU/hr-ft^2									
ΔT	48.2	48.8	48.4	51.5	51.4	52.1	54.7	54.7	55.1
σ_a Compressive	1733	1756	1740	1860	1858	1883	1980	1980	1995
σ_b Tensile	1570	1590	1580	1678	1672	1700	1775	1775	1790
σ_t Tensile	8950	8785	8950	8200	8200	8150	7500	7750	7580
σ_x Tensile	3860	3775	3870	3480	3480	3460	3130	3210	3180
$\sigma_{max.} = \sigma_t + \sigma_b = \sigma_{t\ max.}$	10,520	10,375	10,530	9878	9872	9850	9375	9525	9370
CASE II $Q/A = 412{,}467$ BTU/hr-ft^2									
ΔT	113.3	114.7	113.8	121.2	121.0	122.6	128.7	128.7	129.6
σ_a Compressive	4077	4127	4094	4369	4362	4420	4563	4563	4685
σ_b Tensile	3696	3741	3712	3945	3939	3991	4180	4180	4210
σ_t Tensile	8950	8785	8950	8200	8200	8150	7500	7750	7580
σ_x Tensile	3860	3775	3870	3480	3480	3460	3130	3210	3180
$\sigma_{max.} = \sigma_t + \sigma_b = \sigma_{t\ max.}$	12646	12526	12662	12145	12139	12141	11680	11930	11790
CASE III $Q/A = 423{,}310$ BTU/hr-ft^2									
ΔT	116.3	117.7	116.8	124.4	124.2	125.8	132.0	132.0	133.0
σ_a Compressive	4185	4235	4203	4485	4477	4535	4772	4772	4808
σ_b Tensile	3794	3839	3810	4049	4043	4095	4288	4288	4320
σ_t Tensile	8950	8785	8950	8200	8200	8150	7500	7750	7580
Tensile	3860	3775	3870	3480	3480	3460	3130	3210	3180
$\sigma_{max.} = \sigma_b + \sigma_t = \sigma_{t\ max.}$	12744	12624	12760	12249	12243	12245	11788	12038	11900
UPPER HALF									
I.D.	.3275	.3295	.3315	.3275	.3295	.3315	.3275	.3295	.3315
O.D.	.3795	.3815	.3835	.3835	3855	.3875	.3875	.3895	.3915
CASE I $Q/A = 100{,}500$ BTU/hr-ft^2									
ΔT	27.5	27.5	27.6	29.2	29.3	29.3	31.2	31.1	31.3
σ_a Compressive	1030	1030	1032	1090	1095	1095	1170	1168	1175
σ_b Tensile	925	925	930	980	985	985	1047	1043	1050
σ_t Tensile	8165	8150	8295	7490	7497	7716	7002	7013	7124
σ_x Tensile	3478	3484	3538	3150	3158	3250	2907	2917	2963
$\sigma_{max.} = \sigma_t + \sigma_b = \sigma_{t\ max.}$	9090	9075	9225	8470	8482	8701	8049	8056	8174
CASE II $Q/A = 382{,}017$ BTU/hr-ft^2									
ΔT	104.1	104.1	104.5	110.6	111.0	111.0	118.3	117.9	118.7
σ_a Compressive	3888	3888	3903	4138	4153	4153	4439	4424	4454
σ_b Tensile	3503	3503	3517	3718	3732	3732	3964	3951	3978
σ_t Tensile	8165	8151	8295	7490	7497	7716	7002	7013	7124
σ_x Tensile	3478	3484	3538	3150	3158	3250	2907	2917	2963
$\sigma_{max.} = \sigma_t + \sigma_b = \sigma_{t\ max.}$	11668	11654	11812	11208	11229	11448	10966	10964	11102
CASE III $Q/A = 395071$ BTU/hr-ft^2									
ΔT	107.7	107.7	108.1	114.3	114.8	114.8	122.3	121.9	122.8
σ_a Compressive	4022	4022	4037	4277	4295	4295	4589	4574	4608
σ_b Tensile	3625	3625	3638	3842	3859	3859	4098	4085	4115
σ_t Tensile	8165	8151	8295	7490	7497	7716	7002	7013	7124
σ_x Tensile	3478	3484	3538	3150	3158	3250	2907	2917	2963
$\sigma_{max.} = \sigma_t + \sigma_b = \sigma_{t\ max.}$	11790	11776	11933	11332	11355	11575	11100	11098	11239

The calculations made with Eqs. (1.14, 1.15, 1.16, and 1.17) implicitly assumed that the cladding consisted of an infinitely long cylinder. This assumption is valid except in calculating the stress at the ends of the rod. The stress in the cladding near the end may be calculated by equations given by C. H. Kent:[9]

$$y = \frac{1-\mu^2}{2EI\beta^2}\left(M_o\phi - \frac{q_o}{\beta}\theta\right) + \frac{1+\mu}{2\beta^2}\frac{\alpha\Delta T\psi}{h} + \frac{pc^2}{Eh} \qquad (1.18)$$

$$\sigma_x = \frac{E\alpha\Delta T}{(1-\mu)h}\eta(1-\phi) - \frac{12\eta}{h^3}\left(M_o\phi + \frac{q_o}{\beta}a\right) + \frac{pc}{2h} \qquad (1.19)$$

$$\sigma_t = E\alpha\Delta T\frac{\eta}{h} + \frac{Ey}{c} + \mu\left(\sigma_x - \frac{pc}{\eta}\right) \qquad (1.20)$$

where,

$a = e^{-\beta x}\sin\beta x$

c = mean radius of cylindrical shell

E = Young's Modulus = 11.5×10^6 lb/in^2

h = thickness of shell

h_1 = thickness of head (end cap)

I = moment of inertia of strip of unit width and depth, $h = \frac{h^3}{12}$

M_o = moment

p = pressure inside cylinder - pressure outside

q_o = force

T = radial temperature drop through clad = 110 F

x = distance along cylinder axis

y = deflection

α = thermal coefficient of expansion = 3.4×10^{-6} in/in$^\circ$F

---

9. C. H. Kent, "Thermal Stresses in Thin-Walled Cylinders," APM-55-13.

$$\beta = \left[\frac{3(1-\mu^2)}{h^2c^2}\right]^{.25} = 17.5$$

η = distance from neutral axis + h/2 to o.d.
- h/2 to i.d.

$\theta = e^{-\beta x} \cos\beta x$

μ = Poisson's ratio = .45

σ = stress

σ_t = tangential stress

σ_x = axial stress

$\phi = e^{-\beta x} (\cos\beta x + \sin\beta x)$

$\psi = e^{-\beta x} (\cos\beta x - \sin\beta x)$

where, M_o and q_o are determined by solving the following equations simultaneously:

$$\frac{1+\mu}{2\beta^2} \frac{\alpha\Delta T}{h} + \frac{pc^2}{Eh} - \frac{1-\mu^2}{2EI\beta^2}\left(M_o + \frac{q_o}{\beta}\right) = -\frac{q_o c}{Eh_1}(1-\mu) \qquad (1.21)$$

$$-\frac{1-\mu^2}{2EI\beta^2}(2\beta M_o + q_o) - \frac{1+\mu}{\beta}\frac{\alpha\Delta T}{h} = -\frac{3pc^3(1-\mu)}{2Eh_1^3} + \frac{12M_o c}{Eh_1^3}(1-\mu) + \frac{\alpha\Delta T}{h_1} c \qquad (1.22)$$

By assuming that the end cap is infinitely thick compared to the wall thickness and that there is a constant temperature gradient in the radial direction, only the stresses in the clad may be found.

Before calculating stress, it can be shown that σ_t is maximum at a point far removed from the end cap. Therefore end effects in the tangential direction are negligible. Furthermore, σ_x is maximum when x is zero, thus cancelling some terms in the equations. It is obvious that the worst condition in the boiler core will be in the lower half with maximum i.d. and minimum wall because the upper half has a smaller diameter with the same wall thickness.

Solving the simultaneous equations; Eq. (1.21, 1.22), it is found that M_o = 1.73 lb-in/in. of circumference, and q_o = -76 lb. Substituting in the Eq. (1.19) at x = 0, it is found that the axial stress on the outside of the clad is 10,150 psi. Stress on the inside of the clad is 20,390 psi.

1.4.2.4 Fuel Element Component Testing. Nozzle-Galling Test.

A test apparatus was designed and constructed to test nozzle materials and treatments (Fig. 1.19, ACNP-6007). The apparatus simulates movement of the fuel element nozzle in the grid plate by moving a nozzle assembly up and down within a nozzle sleeve. The test is activated by means of two air cylinders, one mounted vertically and the other horizontally. By operating the vertical cylinder alone, the nozzle assembly is moved up and down within the nozzle. By operating the horizontal cylinder, the nozzle sleeve, which is mounted on a clevis bracket, can be tilted. Thus the situation simulates a condition in the reactor when the fuel element may be tilted with respect to the reactor grid plate and where differential thermal expansion causes relative motion between the two. The total length of travel of the nozzle in the test apparatus was 1.25 in.

Visual inspections of the nozzle and nozzle sleeve were made after a test run. During the test, the vertical and horizontal pressures were recorded and the force necessary to move the nozzle within the sleeve was subsequently calculated.

In order to determine the friction force of the shafts moving through the packing glands, a test was conducted without the nozzle or nozzle sleeve. The friction forces were about 30 lb. on the vertical shaft and 60 lb. on the horizontal shaft. However, the packing was changed several times between test runs and the packing rings were tightened from time to time during the heating up period. Therefore, these values for the forces required to overcome friction could have varied considerably.

Nozzle sleeves for the test were made of 304 stainless steel, which is the material used in the reactor. Nozzles were made of the following materials: 304 stainless steel, 17-4Ph stainless steel, and chrome-plated 304 stainless steel.

304 Stainless Steel Nozzle. The hardness, surface finish, and diameters of the 304 stainless steel nozzle or nozzle sleeve were not exactly known for this test. The test was run at 540 psi and 477 F with no horizontal force. At 55 psi air in the vertical cylinder, the nozzle moved approximately 1/8 in. Application of pressures up to 98 psi in the vertical cylinder did not result in further movement of the nozzle. These air pressures correspond to net downward forces of 388 and 1228 lbs respectively.

After the test apparatus had cooled to room temperature, an attempt was made to move the nozzle. At 50 to 55 psi vertical-cylinder pressure, the nozzle moved through its maximum stroke, 1.25 in. The pressure was equivalent to a net downward force of about 1000 lb. The nozzle was operated through four strokes in this manner. Severe galling was noted on both the nozzle and nozzle sleeve when they were examined after the test. This galling is shown in Figure 1.17.

17-4 Ph Stainless Steel Nozzle. A second test was conducted with a nozzle made of 17-4 Ph stainless steel. The characteristics of this nozzle were as follows: hardness - BHN 404; surface finish - 20×10^{-6} in.rms. The 304 stainless steel sleeve had a hardness of BHN 153 and a surface finish of 20 to 32×10^{-6} in. rms. The

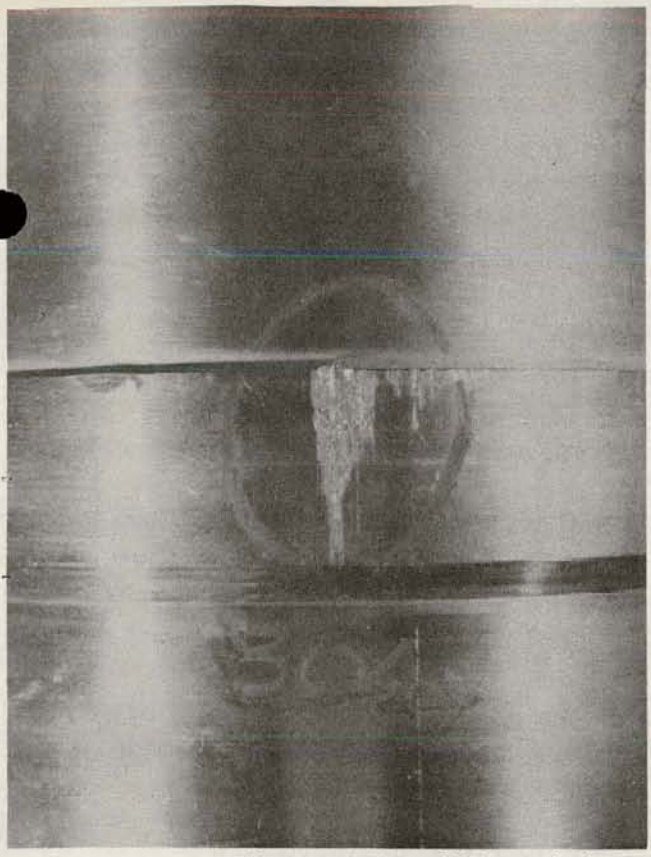

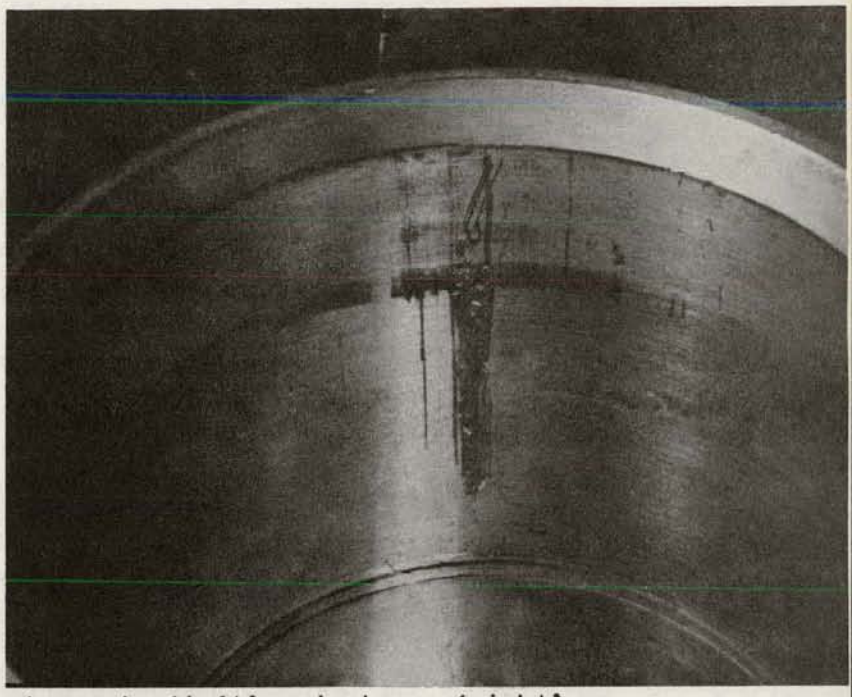

Figure I.17 304 stainless steel nozzle (left) and sleeve (right).
No horizontal force was applied to the sleeve. (NP Photo 18A-5, -10).

Figure I.18 17-4 Ph Nozzle (left with 304 stainless steel sleeve.
No horizontal force was applied. (N-P Photos 18A-7, -9).

diametral clearance between nozzle and sleeve was 0.014 in.

The first test run consisted in 50 cycles with no horizontal force at 595 psi 488 F. Initially approximately 65 psi was required to move the nozzle. This operating pressure leveled off to about 45 psi with 578 psi in the test housing, which yields a net downward force of 144 lb.

When the test was disassembled, the nozzle and sleeve were both slightly marred. The marring seemed to consist of scratches rather than galling. The surfaces are shown in Figure 1.18.

A second test run was made with the same nozzle and sleeve. The nozzle was cycled one-hundred times with no horizontal force at 620 psi in the test housing at 490 F. The operating force leveled off to about 33 lb net downward force.

Under these circumstances, a 165-lb horizontal load was applied. The net force required to move the nozzle rose to 482 lb on the first and second stroke. The force increased to 780 lb. net on the third stroke, and to 978 lb. net on the fourth. The horizontal load was then reduced to 70 lb, and the operating force decreased to 592 lb. net for the next six cycles. The horizontal load was removed entirely and the nozzle was operated for ten cycles. The force required to operate the vertical cylinder decreased to 425 lb. net, but did not decrease further. This increase from 33 lb. net at the start of the test to 425 lb. net at the end of the test is attributed to galling.

When the test was disassembled considerable evidence of galling on both the nozzle and sleeve was evident (Figure 1.19).

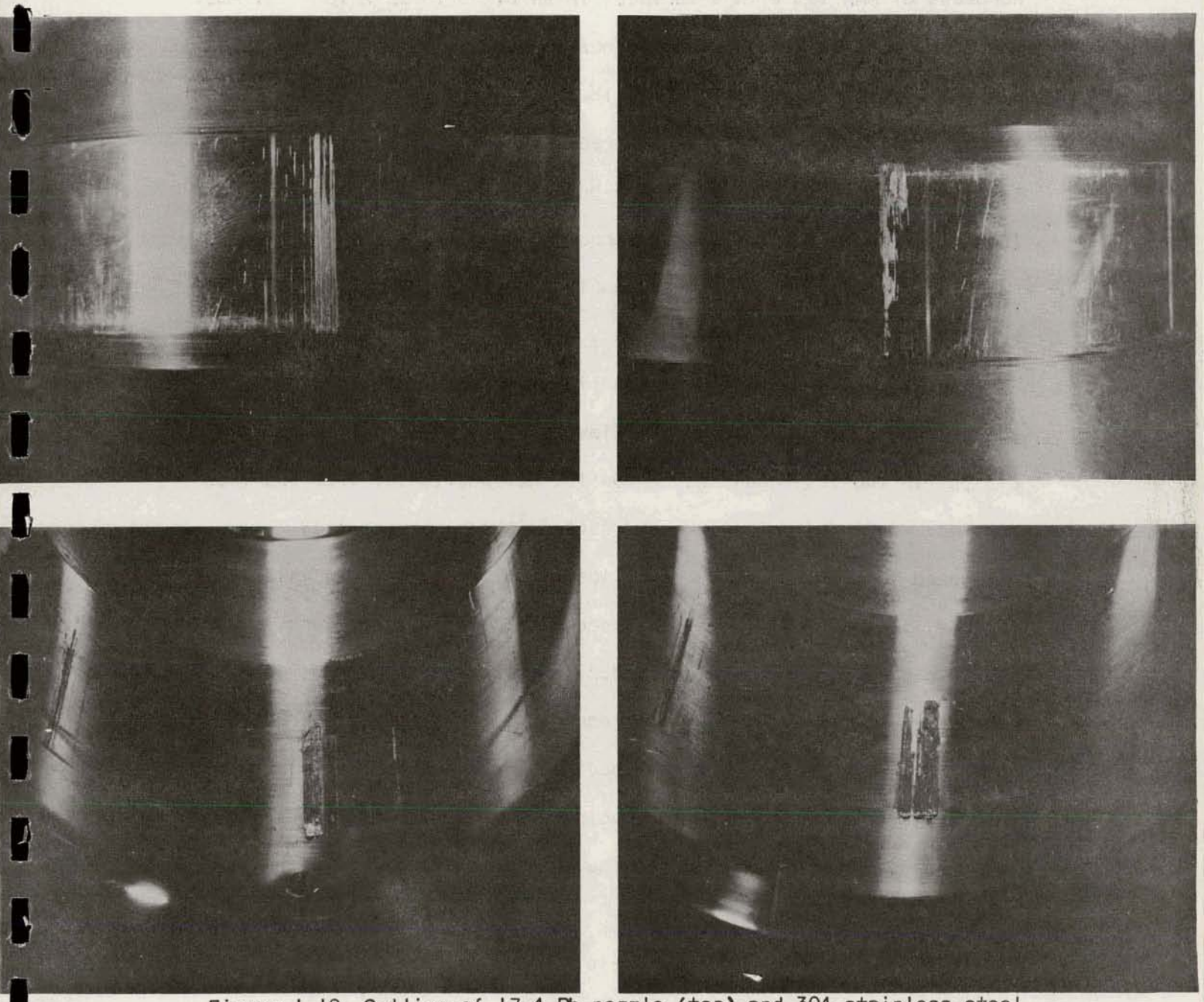

Figure 1.19 Galling of 17-4 Ph nozzle (top) and 304 stainless steel sleeve (bottom). Horizontal load of 165 lb was applied. (N-P Photos 18a-15, -16, -13, and -12).

Chrome-Plated 304 Stainless Steel Nozzle. The third nozzle tested was chrome-plated 304 stainless steel of hardness BHN 870 and with surface finish of 18 to 25 x 10^{-6} in. rms. The 304 sleeve had a hardness of BHN 153 with a surface finish of 20 to 32 x 10^{-6} in. rms. The diametrical clearance between nozzle and sleeve was 0.012 in.

The first test run consisted in 100 cycles without any horizontal force applied. The pressure required to operate the vertical air cylinder quickly leveled off to 43 psi with the housing at 615 psi. This resulted in a net downward force of 60 lb.

The test assembly was disassembled for inspection. The nozzle was not marred. The sleeve had only minute scratches.

The second test run consisted first in 50 cycles without a horizontal load. The operating force leveled off to 60 lb. net with 615 psi in the test housing. A 155 lb. net horizontal load was then applied. On the first stroke thereafter, the operating load increased to 575 lb. net downward load. On the second and third strokes, the required force increased to 673 lb. net downward. From the fourth through tenth cycles, during which the horizontal load was decreased to 82 lb. net, the required downward force decreased to 581 lb. net. The horizontal load was then removed entirely, and the nozzle was operated for ten cycles. The force required decreased to 60 lb. net downward, which is the same force required at the beginning of the test.

When the test nozzle and nozzle sleeve were examined, no galling was observed (Figure 1.20). The nozzle was not marred but the sleeve was scratched.

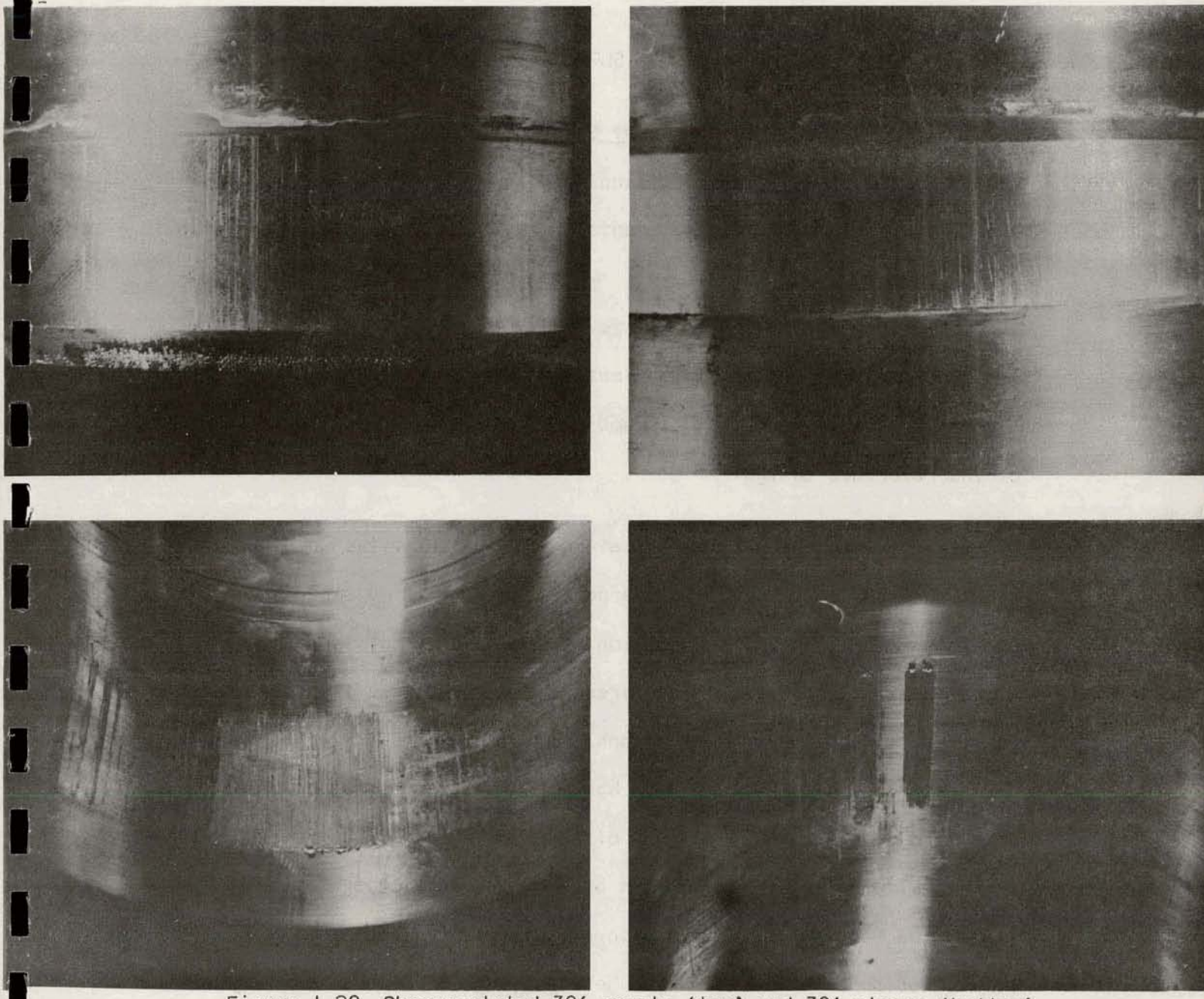

Figure 1.20 Chrome-plated 304 nozzle (top) and 304 sleeve (bottom) after galling test with 155 lb. horizontal load.
(N-P Photo 18A-18, -19, -25, and -20).

Conclusions. Tests thus far show that chrome-plated 304 stainless steel is a suitable material for the fuel element nozzle. Further tests will be conducted with chrome-plated stainless steel with different surface finishes.

1.4.3 HIGH-ENRICHMENT SUPERHEATER FUEL ELEMENT

1.4.3.1 Prototype High-Enrichment Superheater Fuel Element. A program to formulate fabrication techniques for the manufacture of high-enrichment superheater fuel elements to Pathfinder specifications with current technology is continuing. Martin Nuclear Division is conducting this study under subcontract to Allis-Chalmers. The program consists of two phases: 1) to fabricate cermet dispersion fuel tubes, and 2) to develop a suitable method of assembling superheater elements of the reference design.

Uranium Dioxide Powder. Specifications require that the uranium dioxide powder used in making the cermet be high-fired spherical particles of -270+325 mesh fraction with a density not less than 93 per cent of theoretical. At present, it is difficult to obtain powder meeting these specifications. Davison Chemical Co. has agreed to supply 20 lbs, of which 2 lbs have been delivered. Other possible suppliers have been queried, but offer no guarantee of delivery.

In view of the difficulty in obtaining powder of a suitable grade, the Martin Nuclear Division is experimentally preparing a high-fired spherical powder by a jet-spraying technique. Although

powder prepared initially showed internal porosity, the technique shows promise. Continued study of this technique is being sponsored by the Martin Nuclear Division.

Cermet Fuel Tubes. Several cermet strips were prepared using various grades of uranium dioxide powder. Longitudinal views of three strips are shown in Figure I.21. The top strip was rolled from Mallinckrodt Chemical Works' spherical grade powder. The powder is very spherical in the larger particle sizes, but is similar to regular high-fired powder in the size (-270+325 mesh fraction) desired.

The center photomicrograph is a view of a strip prepared from Davison spherical powder. The superior quality of this strip is easily apparent in less stringering and agglomeration of oxide particles within the stainless steel matrix.

The bottom strip was fabricated from high-fired polygonal-shaped powder.

Approximately four to six cermet fuel tubes will be made with the 2 lbs of Davison powder that has been received, and the fabrication process and cermet quality will be evaluated.

Assembly of Fuel Elements. Fuel tubes made from high-fired polygonal shaped oxide will be used for studying assembly operations. This will be a study of assembling the entire fuel element including the poison tube, two fuel tubes, and wire spacers to tolerances stated in Pathfinder specifications.

Preliminary studies were made of three assembly methods by using stainless steel tubes mocking up Pathfinder fuel tubes. The first

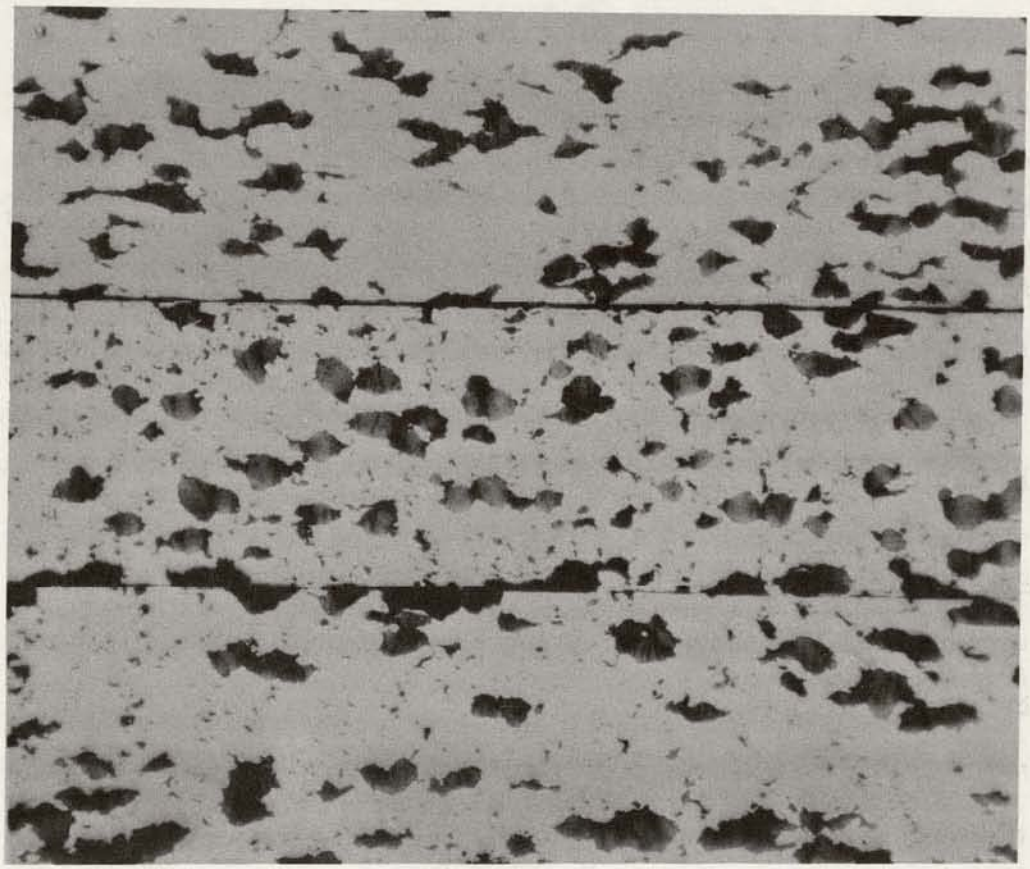

Figure I.21 Final roll and sinter of uranium dioxide cermets. Longitudinal sections of strip d, strip j, and strip k (top to bottom) as-polished. Magn. 100 X. (Martin Nuclear Division).

method studied consisted in manually slipping one stainless steel tube within another. The specified spacer wires were attached with soft solder. Lengths of only 12 to 24 in. could be put together in this way.

In the second method studied, the inside tube was cooled with liquid nitrogen while the outer tube was heated with hot water. Using this technique it was possible to assemble the fuel tubes and poison rod only with considerable galling between spacer wires and tube surfaces.

In the third method, a V-block is used to press the outer tube against a flat bed flexing the tube within its elastic range to approximate a triangular shape. The inner tube with the spacer wires attached may then be slipped into the outer tube. The poison tube is being assembled within the inner tube in the same manner.

Methods of attaching the spacer wires over the entire length of the tube were studied. At present, an ultrasonic welding technique appears best.

1.4.3.2 Mechanical Design. Stress Analysis. The fuel tubes have A 1/4-in gap at the center and a 1/2-in length at the ends that contain no fuel. The temperature of these non-fueled portions drops down to steam temperature within a short distance from the fuel bearing section, and causes axial temperature gradients and thermal stresses.

The axial temperature gradient was calculated by considering the tube wall to be a thin, flat fin with two-dimensional heat flow by the equation,[11]

11. Bird, et al. "Notes on Transport Phenomenon", p. 162, 1959

$$\theta_{x,y} = \frac{T - T_s}{T_w - T_s} = 2H\theta_o \sum_{n=1}^{\infty} \frac{\cos(\alpha_n \eta) \cos h[\alpha_n (1-\xi)]}{[\alpha_n^2 + H^2)r + H] \cos(\alpha_n r) \cos h(\alpha_n)} \quad (1.24)$$

where, $H = \frac{hL}{k} = \alpha \tan \alpha r$

$r = c/L$, $\xi = x/L$, $\eta = y/L$

h = surface heat transfer coefficient, Btu/hr-ft^2-^{o}F

k = thermal conductivity of tube, Btu/hr-ft-^{o}F

L = length of tube in (x) direction, ft.

T_w = constant wall temperature at the end of the fuel

T_s = temperature of the steam surrounding the end of the tube.

This equation gave an axial temperature gradient for the hottest fuel element of 560 F per in. at the end of the tube, and 2400 F per in. at the center fuel gap.

Assuming a linear temperature gradient, which is conservative, the maximum longitudinal stress was calculated from the equation,[12]

$$\sigma_z = \frac{2(0.329)\alpha E \sqrt{R_m t}}{(1-\nu^2)^{3/4}} \frac{\Delta T}{\Delta Z} \quad (1.25)$$

where, α = linear coefficient of expansion, in/in-^{o}F

E = modulus of elasticity, lb/in^2

ν = Poisson's ratio

R_m = mean radius of the tube

t = wall thickness

$\frac{\Delta T}{\Delta Z}$ = linear temperature gradient

12. Timoshenko, "Theory of Plates and Shells," p. 424, 1940

The tangential stress due to the axial temperature gradient is given by the equation,

$$\sigma_\theta = \nu \sigma_z \qquad (1.26)$$

There is also a radial temperature gradient of 66 F at the end of the tube and 50 F at the center gap. The stress due to the radial temperature gradient is calculated by the equation,

$$\sigma_\theta = \sigma_z = \frac{\alpha E \Delta T}{2(1-\nu)} \qquad (1.27)$$

for the portion of the cylinder away from the end. At the free end of the cylinder, the stress is about 30 per cent higher[13].

Eqs. (1.25, 1.26, 1.27) gave the following maximum stresses due to both the radial and axial temperature gradients:

at tube end

σ_z = 21,100 psi
σ_θ = 16,350 psi
$\sigma_{yield\ stress}$ = 19,000 psi
(316 SS at 1300F)

at center gap

σ_z = 47,400 psi
σ_θ = 21,400 psi
$\sigma_{yield\ stress}$ = 20,000 psi
(316 SS at 1180F)

Since these stresses are in excess of the yield strength of the material, there will be some plastic deformation. Assuming free differential expansion, the maximum deformation is a reduction in the tube diameter of 0.001 in. at the end and 0.003 in. at the center gap.

13. C. H. Kent, "Thermal Stresses in Thin-Walled Cylinders", APM-53-13, p. 167, 1931

Thermal Fatigue. The fuel tubes were checked for thermal fatigue due to cycling of the stresses at the fuel gaps. The number of stress cycles needed to cause failure was calculated from the equation,[14]

$$N^{1/2} = \frac{C}{\Delta\epsilon_p} \qquad (I.28)$$

where,

N = number of cycles to failure

$C = f/2 = 1/2 \ln \frac{100}{100-RA}$

where, RA is the percentage reduction in area determined in a tensile test

$$\Delta\epsilon_p = \frac{\sigma_{max} - 2\sigma_{yield\ stress}}{E}$$

Eq.(I.28) gave 1.88×10^6 cycles for the maximum stress of 47,400 psi.

Thermal Shock. Preliminary thermal shock calculations indicate that the superheater fuel tubes can withstand a shock of 1000 F for 1000 cycles if the tubes retain their original ductility. However, under reactor operating conditions, it is known that a brittle phase known as sigma phase can occur in 316L stainless steel when held at elevated temperatures. The number of stress cycles that a material can withstand is related to the ductility by Eq. (I.28), since the percentage reduction in area (RA) is a measure of ductility. The plastic strain range is determined from stress calculations. Therefore, if the percentage reduction in area is known for the given material conditions, the number of cycles to failure can be predicted with reasonable accuracy.

The reduction in ductility due to sigma phase formation will

14. L. F. Coffin, "Design for Low Cycle Fatigue", SESA Design Clinic, October 1959

be determined by heating tensile test specimens of 316L stainless steel in a furnace and measuring the percentage reduction in area in a tensile test after various heating times. It is expected that the reduction in ductility will level off after a period of time, allowing extrapolation to the fuel element lifetime. With the maximum expected reduction in ductility known, it should be possible to predict a safe thermal shock limit.

Plastic Deformation during Shut-Down. When the superheater is flooded at shutdown, uneven flow patterns can cause permanent deformation of the fuel element as well as failure due to thermal shock stresses. The spacers and other restraints will effect the maximum stresses and deformations; therefore, a thermal shock test is planned in which the flooding conditions will be simulated using a complete fuel element assembly.

The maximum temperature gradient that can be tolerated without stressing the superheater tubes beyond the elastic limit were calculated for various temperature distributions.

A linear temperature difference (ΔT) across the tube diameter would tend to cause bowing, which can be calculated by the equation,

$$y = \int \frac{(\alpha \Delta T)}{d_o} dx + \iint \frac{M}{EI} dx^2 \qquad (I.29)$$

where,

y = deflection, in.

d_o = outside diameter of tube, in.

M = bending moment caused by spacers

I = moment of inertia of the tube cross section

Since the deflection at the spacers is zero, the bending moment and stress can be determined as a function of ΔT. With the tube completely restrained from bowing, the maximum stress is given by the equation,

$$\sigma_z = \frac{\alpha E \Delta T}{2} \qquad (1.30)$$

Calculations show that if a maximum temperature differential of 190 F is not exceeded, the elastic limit of the tube will not be exceeded.

If the tube is restrained at intermittent points along its length, the maximum stress is higher at these points.

With the tube simply supported at the center and at each end, the maximum stress is given by the equation,

$$\sigma_z = 3/4\ \alpha E \Delta T \qquad (1.31)$$

For this case, the maximum temperature differential is 124 F.

In restricting the bowing, the wire spacers apply a radial force on the tube wall that can cause radial deformation. Assuming that the tube is simply supported at the center and at each end, the maximum circumferential bending stress is given by the equation,

$$\sigma = 27 \frac{\alpha \Delta T}{d_o} \left(\frac{E}{L}\right)\left(\frac{Rm^4}{t}\right) \qquad (1.32)$$

where, Rm = mean radius of the tube

d_o = outside diameter of tube

L = total length of tube.

Calculations then show that if maximum linear temperature differentials across the tube diameter of 250 F for the outer fuel tube or 600 F for the inner fuel tube are not exceeded, the elastic limits of the tubes will not be exceeded.

Collapsing stress in poison rod cladding. The maximum stress in the poison rod cladding is due to the external pressure (p) of approximately 600 psi. The equation for the critical collapsing pressure (p_{cr}) for a perfectly round tube is given by the equation[15],

$$P_{cr} = \frac{Et^3}{4(1-\nu^2)\ R_m^3} \qquad (1.33)$$

which when calculated gives a required wall thickness of 0.010 in. However, there will be some initial ovality of the tube which increases the required wall thickness. The maximum stress in a long tube with an initial radial deviation from a circle (w_o) is given by the equation,[16]

$$\sigma_{max} = \frac{pR_m}{t} + \frac{6pR_m}{t} \frac{w_o}{1 - p/p_{cr}} \qquad (1.34)$$

Eq. (1.34) gives approximately the same stress as an equation given by R. G. Sturm[17].

Eq. (1.34) was used to plot curves of maximum stress versus wall thickness for various ovality tolerances. When the maximum temperature of the poison rod cladding is determined, the allowable stress at this temperature can be used to determine the required wall thickness.

Stresses in the inner insulating tube. The required wall thickness for the inner insulating tube was calculated using the ASME Unfired Pressure Vessel code, Section VIII, 1959, Par. UG-27. With a maximum transient pressure drop of 180 psi through the superheater, a wall

15. Timoshenko, "Theory of Elastic Stability"
16. Timoshenko, op. cit.
17. R. G. Sturm, "A Study of the Collapsing Pressure of Thin-Walled Cylinders", University of Illinois Engineering Experimental Station, Bulletin No. 329, 1941.

thickness of 0.0064 is required using 304 stainless. With a wall thickness of 0.020 in. the maximum tangential stress is 4,100 psi and the maximum longitudinal stress is 2140 psi.

In the supporting section at the end of the fuel element, the maximum tangential stress is 3000 psi tension and the maximum longitudinal stress is 1500 psi compression. All stresses in the inner insulating tube are below that required for 1 per cent creep in 10,000 hr. for 304 stainless steel.

1.4.3.3 Superheater Container Tube Seal Test. A high-pressure test of the superheater container tube seal is under consideration. The seal that will be tested is a tapered aluminum sleeve in series with a stainless steel O-ring. Two seals were ordered and received. The seals will be tested in the test apparatus (Fig. 2.10) that is being used to test a cold-rolled seal between the inner and outer container tube.

1.5 NUCLEAR HANDLING TOOLS

The objective of this project is to perform conceptual engineering and experimental work as required for development of simplified but reliable fuel handling tools and special tools for repairing or replacing reactor parts.

1.5.1 BOILER FUEL HANDLING TOOLS

A preliminary layout of the boiler element handling tool was completed, and is shown in Figure 1.22. The redesign of the boiler fuel element (see section 1.4.2) eliminated the need for underwater box-changing equipment.

1.5.2 SUPERHEATER FUEL HANDLING TOOLS

The prototype superheater element handling pole shown in the last quarterly report (Fig. 1.22, ACNP-6007) was constructed and tested in the 40-ft handling tank. It performed very well.

1.5.3 CONTROL ROD HANDLING EQUIPMENT

A test was run to determine the feasibility of using an underwater torch to cut irradiated control rods. The cutting operation caused rapid blackening of the water, which was unsatisfactory.

Some preliminary work was done on conceptual design of handling tools for both the boiler and superheater control rods. The superheater control-rod poison pins will be delatched from the yoke in the core, and picked-up with a long handled tool, and placed in a handling rack. This procedure is similar to that used in handling superheater fuel elements.

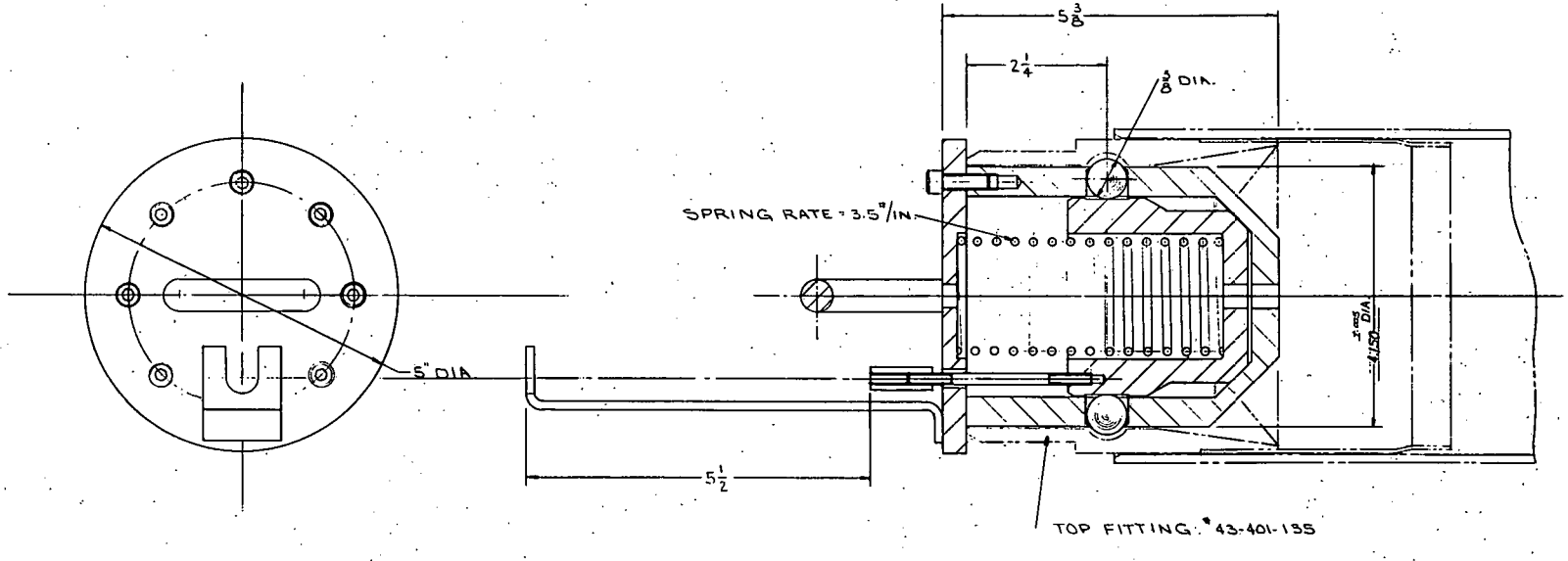

Figure 1.22 Head layout for boiler fuel handling tool. (A-C Dwg. 43-002-216)

1.6 LOW-ENRICHMENT SUPERHEATER FUEL ELEMENT

The objectives of this project are as follows: 1) to perform calculations optimizing nuclear and thermal characteristics of a low-enrichment superheater fuel element: 2) to evaluate fabrication and testing techniques that will lead to the lowest cost superheater fuel possible within limits of Pathfinder Plant design and operating reliability; and 3) to attempt to get as much information as is required for early insertion of a low-enrichment superheater core.

1.6.1 CRITICAL FACILITY FUEL

An order was placed with M & C Nuclear Corp for 1400, 3.5 percent enriched and 400, 7-percent enriched stainless steel clad fuel rods for use in critical experiments. Fabrication of these rods is continuing on schedule. The container tubes and other hardware were designed. Detail drawings are being made.

1.6.2 FABRICATION DEVELOPMENT

1.6.2.1 Programmatic Data Survey. Published data on swage compacting fuel is being collected and evaluated. This data includes valuable information on equipment and techniques for cold and hot swaging, cladding materials, fuel element properties, irradiation stability, etc.

1.6.2.2 Ceramic Pellet Fabrication. Minor effort was continued on uranium dioxide pellet fabrication. Four 0.388-in dia. pellets were formed of Shattuck ceramic grade oxide ball milled for 128 hr with 2 w/o Carbowax binder-lubricant. The pellets were pressed at 70 tsi. The green densities of the pellets are given in Table 1.5

Table 1.5 Uranium Dioxide Pellet Density

Sample Number	Green Density (Per cent)
1	72.46
2	72.52
3	72.59
4	72.43

The pellets were placed in the entry zone of a hydrogen furnace and were out-gassed at 250 to 450 C for 12 hr. Density measurements of the out-gassed specimens are being made. The average green density of the pellets was 72.50 per cent of theoretical.

Analysis of some previously fabricated pellets was continued to verify density characteristics. Three of the pellets were prepared from 64-hr ball-milled Shattuck ceramic grade oxide using 2.0 w/o Carbowax pressed at 70 tsi and sintered for 15 hr at 1700 C. Each of these pellets was sectioned into four or five wafers and individual pycnometer densities were made of each wafer. The results are given in Table 1.6.

In the three specimens, density variations between 1 to 3 percent of theoretical, or 0.11 to 0.33 g/cc were found. The first two samples gave wafer density averages in good agreement with the gross pellet density. In the third sample, porosity in the top of the pellet may have resulted in the measurement of a high gross density compared to the average wafer density.

Arc-Fused Uranium Dioxide Powder. Three different sets of uranium dioxide pellets were prepared from Spencer Chemical Company's arc-fused grade of oxide to evaluate pelleting characteristics. The

TABLE 1.6 DENSITY VARIATIONS IN UO_2 PELLETS

SAMPLE NUMBER	GROSS DENSITY Per Cent of Theoretical (Pycnometer)	WAFER DENSITY Per Cent of Theoretical (Pycnometer)				
		1	2	3	4	5
40	92.35	94.81	91.52	91.62	90.90	94.90
		Average = 92.75 ± 2.15				
49	89.87	90.71	89.77	90.64	88.77	-----
		Average = 89.97 ± 1.20				
59	90.39	86.06	89.49	89.44	85.02	89.33
		Average = 87.87 ± 2.85				

TABLE 1.7 UO_2 PELLET PROPERTIES

Sample Number	Forming Pressure (tsi)	Green Density (Percent of Theoretical)	Sintered Density (Percent of Theoretical)
1	70	81.83	
2	70	86.57	
3	60	76.73	
4	60	81.03	
5	70	83.31	
6	70	83.18	
7	70	83.29	
8	70	83.39	
9	70	83.13	
10	70	83.43	
		Ave. = 83.29 + 0.16	
11	70	82.5	95.72
12	70	82.4	95.53
13	70	82.4	95.81
14	70	82.2	95.99
		Ave. = 82.4 ± 0.2	= 95.76 ± 0.23

pellets were made of -400 mesh powder with an average sub-sieve particle diameter of 6 μ. Applicable data is given in Table I.7.

The first four samples were prepared to establish forming pressure. The first ten specimens were sintered in one batch. All of these samples disintegrated in the furnace either due to over-pressing or failure to out-gas all organic binder. Specimens 11 through 14 were sintered for eight hours at 1650 C in hydrogen atmosphere. These specimens were crack-free but surface characteristics were inferior to sintered pellets made from ceramic grade powder.

The automatic time-temperature program controller was installed on the hydrogen furnace. A new series of pellets is being pressed for an evaluation of the time-temperature sintering cycle on pellet characteristics. Results of this study should be available in the next quarterly report.

I.6.4.3 Swage-Compaction Studies. A major effort was continued on swage-compacting uranium dioxide fuel rods. The objective is to prepare a high-density UO_2 fuel rod with limited interconnected porosity for retention of fission-product gases, and with good heat transfer properties. Primary emphasis is directed towards a finished diameter of 0.225 in. for assembly into the septafoil cluster design. A density of 90 to 95 per cent of theoretical is desired.

Parameters under investigation include the following: grade of oxide, powder particle size, particle size distribution, particle density, tap density of pre-swaged powders, quantity and schedule of swaging reduction, and strength and ductility of clad material.

The general procedure followed in fabricating the swage-compacted fuel rods is as follows:

1) cut tube to length
2) clean inside and outside of tube
3) plug one end with steel wool
4) crimp plug end
5) fill tube with powder
6) vibratory pack for 15 min.
7) plug open end of tube
8) crimp plugged end
9) weld crimp ends
10) swage according to schedule

During swaging, the powder first acts as a compressible material After the powder achieves a higher density, the compacted powder acts as a mandrel within the tubing. The cladding, therefore, increases in thickness at first and then decreases in thickness as the ceramic material densifies. The tube progressively elongates after the ceramic material becomes fully dense.

Effects of Power Particle Size. A series of swage-compacted rods were made to determine the effects of particle size on the ultimate swaged density and on the condition of the fuel rod cladding. Spencer Chemical Co. arc-fused oxide of various mesh fractions, was used to load the rods. The 316L stainless steel tubing used in the study was 0.325-in o.d. with 0.010-in thick wall. The loaded tubes were reduced in two successive passes in 0.250 and 0.225 in. dies. The swaging operation is shown in Figure 1.23. Compacted tubes following the last reduction pass are shown in Figure 1.24. The fabrication variations and results of swaging are given in Table 1.8.

TABLE I.8

PROPERTIES OF SWAGE COMPACTED URANIUM DIOXIDE [1]
JK-A Series

SAMPLE NUMBER	MESH SIZE	TAP DENSITY (PERCENT)	REDUCTION SCHEDULE [2]	PERCENT REDUCTION IN AREA	PERCENT ELONG.	FINAL DIAMETER (IN.)	PERCENT OF THEO-RETICAL	WALL THICK. (IN.X10^{-3})	PERCENT VARIATION	SURFACE [3] APPEARANCE
JK-A7	-400	48.1	1	54.1	38	0.220	86.5±0.5	10.1±0.9	8.9	VG
JK-A8	-400	48.1	1	54.1	37	0.220	86.1±0.4	10.5±1.1	10.5	VG
JK-A9	-325+400	48.6	1	54.1	27	0.221	89.2±0.1	11.8±0.8	6.8	FE
JK-A28	-270+325	48.5	3	54.1	42	0.220	90.3±0.9			VG
JK-A32	-230+270	47.7	3	54.1	40	0.221	91.8±0.1			S
JK-A31	-200+230	49.1	3	54.1	43	0.222	90.6±0.9			S
JK-A27	-170+200	47.6	3	54.1	46	0.221	90.6±0.6			VG
JK-A10	-170+325	46.7	1	54.1	31	0.220	89.6+0.6	11.1+1.1	9.9	FE
JK-A11	-170+325	46.7	1	54.1	28	0.221	89.8±0.7	12.4±3.0	24.2	FE
JK-A33	-140+170	50.5	3	54.1	46	0.222	92.2±0.5	11.4±1.4	12.3	S
JK-A12	-140+325	54.7	1	54.1	30	0.220	89.8±0.8	11.6±1.4	12.1	VG
JK-A13	-140+325	54.7	1	54.1	29	0.221	90.3±0.1	11.2±0.4	3.6	F-S
JK-A26	-120+140	50.4	1	54.1	50	0.221	90.6±0.1			VG
JK-A29	-100+120	51.2	1	54.1	47	0.221	91.4±0.4			VG
JK-A5	-100+325	50.5	1	54.1	--	0.219	90.2±0.2	11.1±1.5	13.5	VG
JK-A6	-100+325	50.5	1	54.1	--	0.220	89.6±0.2	10.9±1.0	9.2	VG
JK-A14	-100+325	50.5	1	54.1	32	0.221	89.1±0.8	10.3±0.9	8.7	VG
JK-A15	-100+325	50.5	1	54.1	31	0.221	90.6±0.3	10.3±0.3	2.9	VG

SAMPLE NUMBER	MESH SIZE	TAP DENSITY (PERCENT)	REDUCTION SCHEDULE[2]	PERCENT REDUCTION IN AREA	PERCENT ELONG.	FINAL DIAMETER (IN.)	PERCENT OF THEO-RETICAL	WALL THICK. (IN.X10^{-3})	PERCENT VARIATION	SURFACE[3] APPEARANCE
JK-A25	-80+100	54.8	1	54.1	52	0.221	90.9±1.0			VG
JK-A20	-70+100	48.3	1	54.1	29	0.220	90.6±0.3	10.9±1.1	10.1	VG
JK-A21	-70+100	48.3	1	54.1	29	0.220	90.0±0.5	10.6±1.2	11.3	VG
JK-A18	-70+140	56.7	1	54.1	34	0.219	90.4±0.5	10.6±1.5	14.2	VG
JK-A19	-70+140	56.7	2	54.1	30	0.220	91.7±0.3			VG
JK-A16	-70+170	52.7	1	54.1	29	0.221	89.9±0.1	10.6±1.8	17.0	FE
JK-A17	-70+170	52.7	1	54.1	30	0.221	89.0±0.4	11.4±0.8	7.0	VG
JK-A3	-70+200		1	54.1		0.220	89.5±0.5	11.1±1.3	11.7	VG
JK-A4	-70+200		1	54.1		0.220	86.3±2.5	10.7±1.1	10.3	VG
JK-A30	-70+80	50.2	3	54.1	52	0.221	90.1±1.1			VG
JK-A1	As-Rec'd	60.5	1	54.1		0.220	86.3±2.5	9.5±3.4	35.8	VG
JK-A2	As-Rec'd	60.5	1	54.1		0.219	90.3±1.3	10.2±1.2	11.7	VG

1 All elements prepared from Spencer Fused UO_2 using 0.325 in. o.d. tubing with a 0.010 in. wall.

2 Reduction Schedules 1 = (.325 to .250 to .225); 2 = .325 to .225); 3 = (.325 to .250 to .225 using electric drill).

3 Surface appearance VG = very good; F = folded; FE = folded end; S = Scored.

Figure 1.23 Swage-compacting of uranium dioxide power in 316L stainless steel tubes. (A-C Photo 210491).

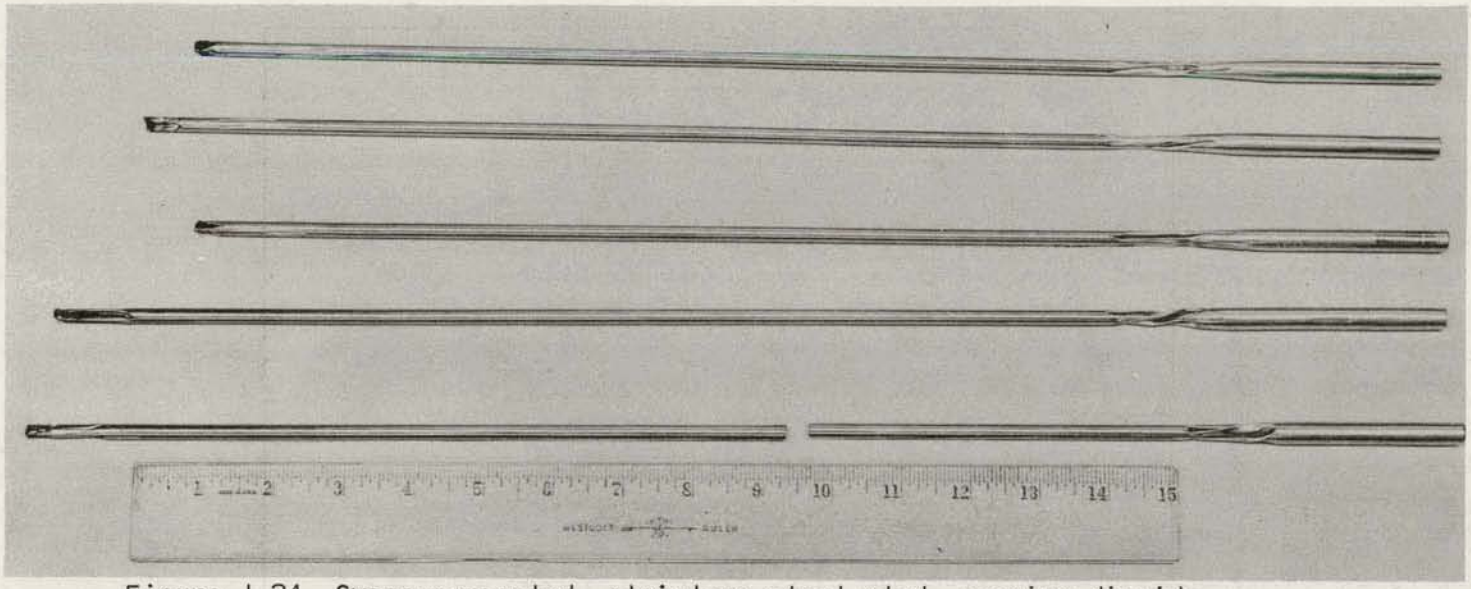

Figure I.24 Swage-compacted, stainless steel clad, uranium dioxide fuel rods. (A-C Photo 210492).

Effect of Powder Particle Size on Swaged Density. A correlation of the powder particle size and swaged density is given in Figure I.25. The highest swaged density of 92.2 per cent of theoretical was obtained using -140+170 mesh fraction powder (sample JK-A33). A density of 90.3 per cent was the highest obtained with as-received powder, seventy per cent of which was -70 mesh (210 u or larger). Four mesh fractions in the 400- to 140- μ (100 to 325 mesh) range yielded swage-compacts of the higher densities. This result is contrary to results obtained by other investigators who have reported the higher densities with the larger particle sizes (125- to 500- μ or 35 to 100 mesh), with other swaging variables constant. As was expected, the finest particle sized powder (-400 mesh) had the lowest swaged density. The fact that the points plotted do not construct a smooth curve is attributed to the relatively wide range of particle sizes within a given mesh fraction.

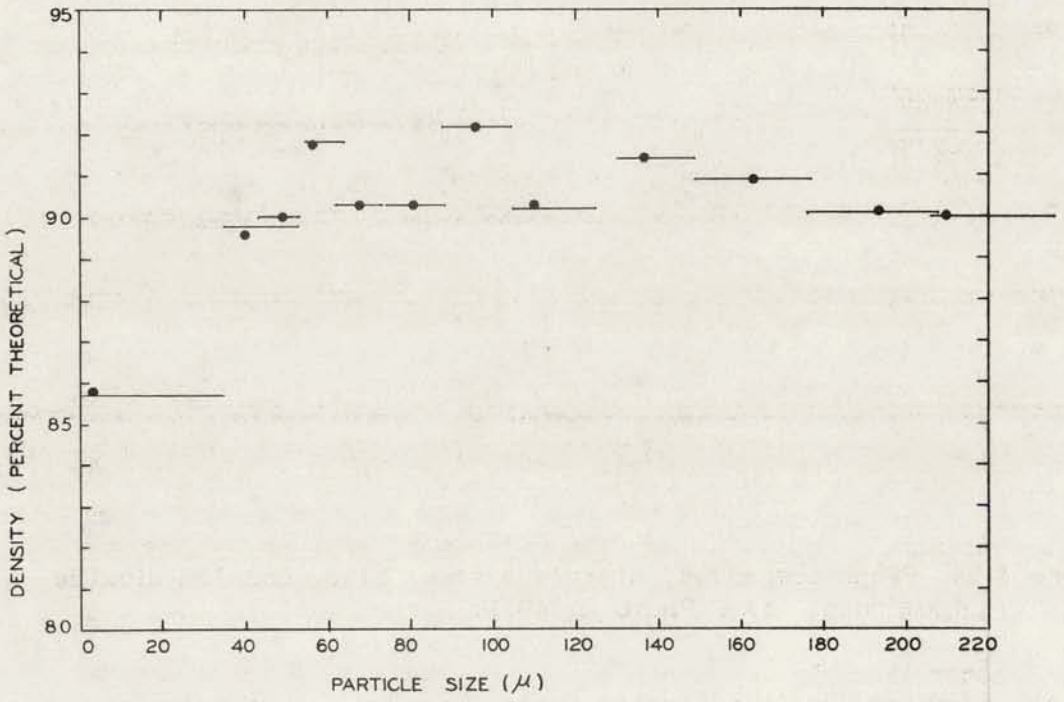

Figure I.25 Swaged density vs. powder particle size.
A-C Dwg. 43-024-362)

Effect of Powder Particle Size on Cladding. Four views of as-received 316L stainless steel tubing supplied by the Trent Tube Co. prior to swaging are shown in Figure I.26. Views of cladding from several swaged rods reported in Table I.8 are shown in Figures I.27 through I.39.

Figure I.27 shows the deformation in the cladding tube wall resulting from the use of powder with larger UO_2 particles. The specimen was swaged with as-received uranium dioxide powder.

Figure I.28 and Figures I.36 through I.38 show that the magnitude of the deformation noticeably decreases as the size of the powder

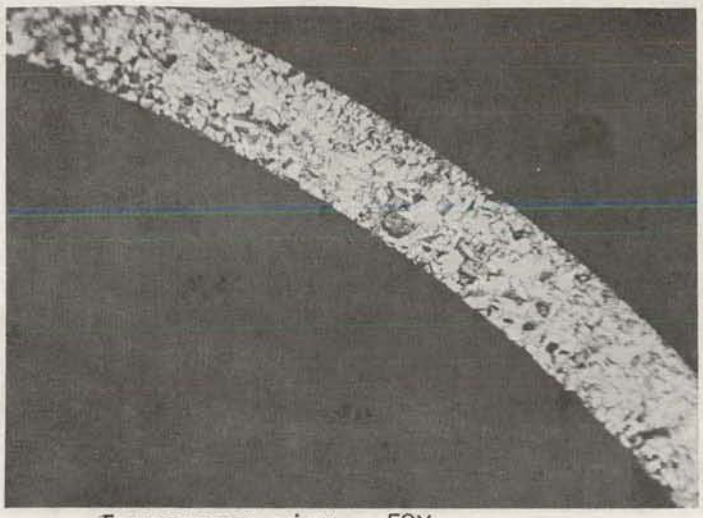

Transverse view - 50X

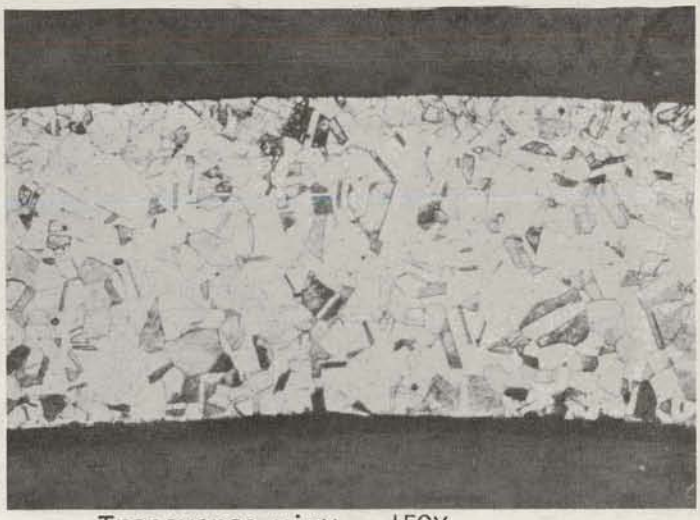

Transverse view - 150X

Longitudinal view - 150X

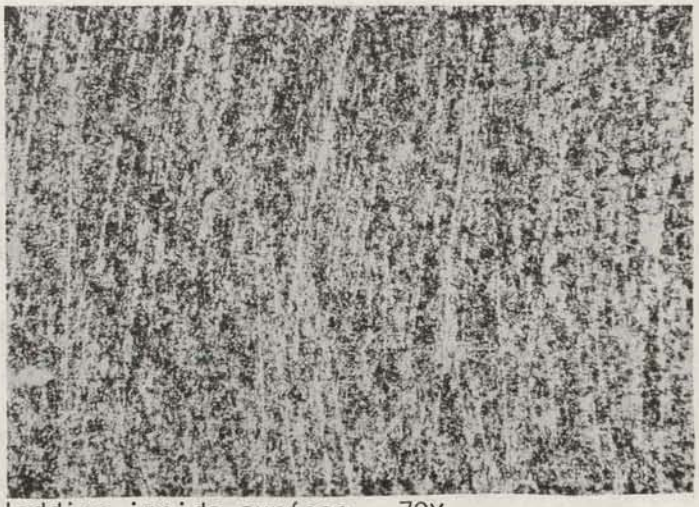

Cladding inside surface - 70X

Figure 1.26 As-received 316L stainless steel tubing 0.010 in. thick used in swaging JK-A series rods. (Trent Tube Co.)
N-P Photos 15A-9-4, -3, -6, -5

particle size decreases. This is further shown in Figures 1.29 through 1.34.

Although the cladding tube containing the smallest particle size powder (-400 mesh), Figure 1.30, was deformed the least; the cladding tube containing the next larger fraction is deformed very little more. The deformation of cladding of the rod with the highest density (Figure 1.35) is intermediate to that for rods containing the largest and smallest particle sized powders. (continued on page 79)

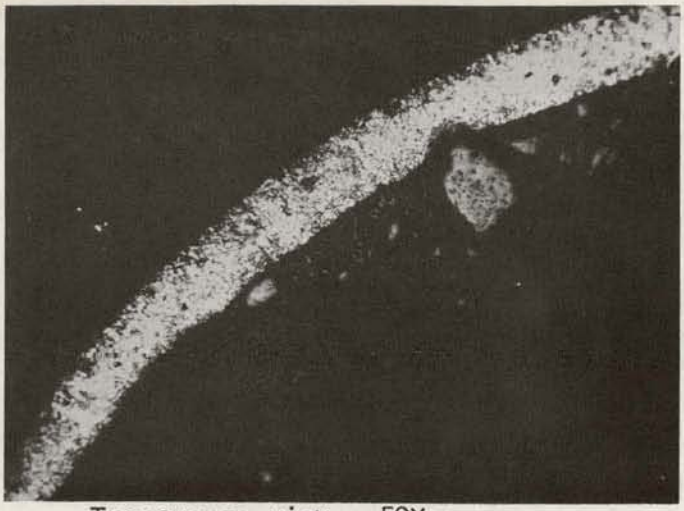

Transverse view - 50X

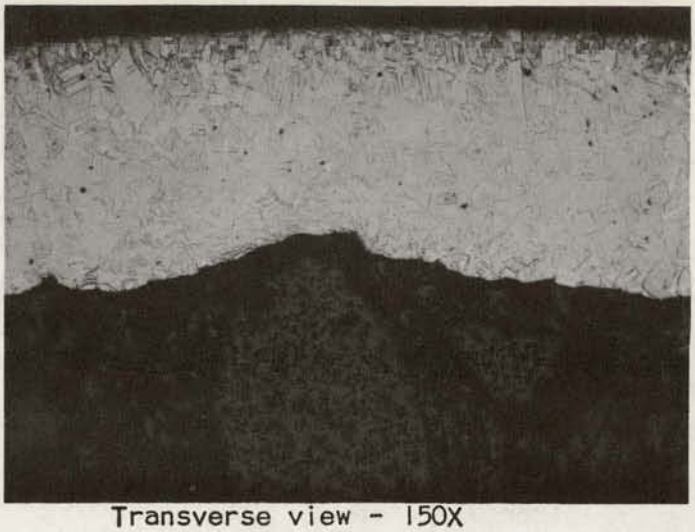

Transverse view - 150X

Figure 1.27 Swage-compacted fuel-rod cladding from samples JK-A1 and -A2 containing as-received Spencer swageable grade uranium dioxide.

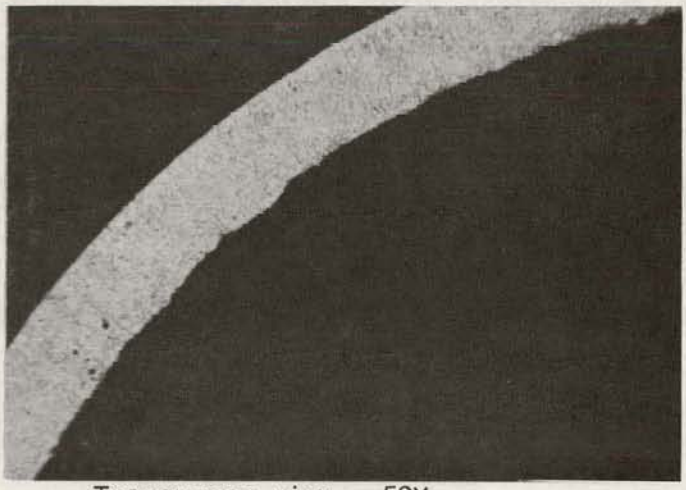

Transverse view - 50X

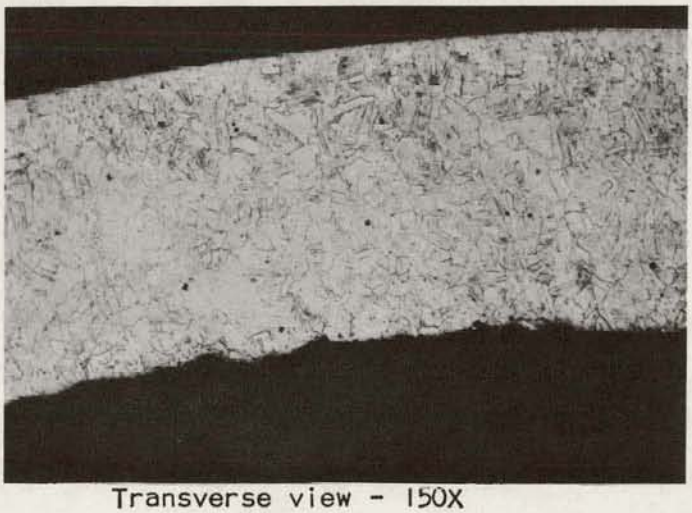

Transverse view - 150X

Figure 1.28 Swage-compacted fuel-rod cladding from samples JK-A3 and -A4 containing -70+200 mesh Spencer swageable grade dioxide.

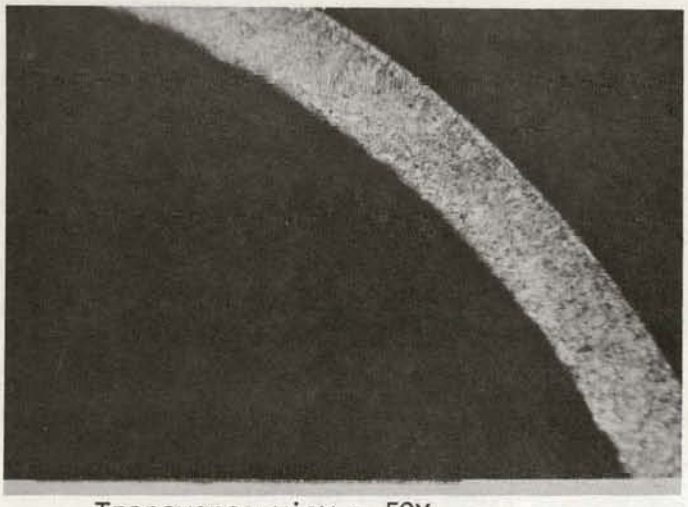

Transverse view - 50X

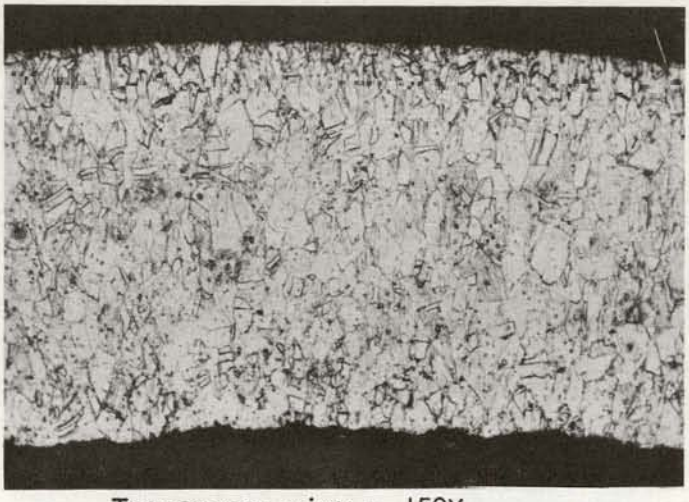

Transverse view - 150X

Figure 1.29 Swage-compacted fuel-rod cladding from samples JK-A5 and -A6 containing -100+325 mesh Spencer swageable grade uranium dioxide.

Longitudinal view - 150X

Clad inside surface - 70X

(NP Photos 15A-14-5, 15A-14-1, 15A-14-2, and 15A-13-6).

Longitudinal view - 150X

Clad inside surface - 70X

(NP Photos 15A-17-5, 15A-16-1, 15A-16-2, and 15A-16-6).

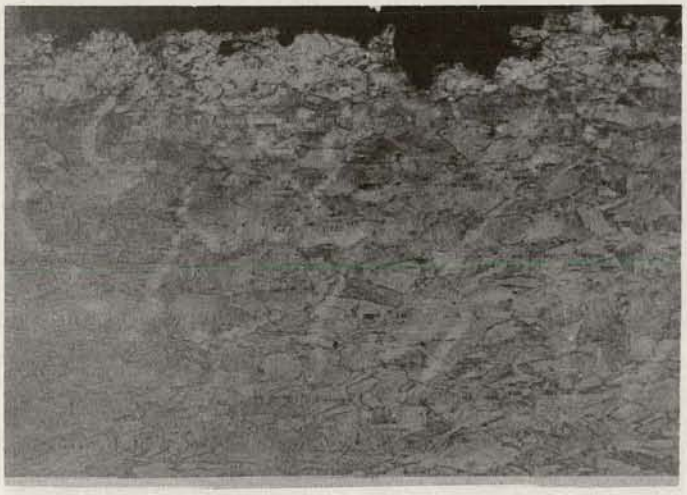

Longitudinal view - 150X

Clad inside surface - 70X

(NP Photos 15A-19-3, 15A-7-1, 15A-19-2, and 15A-19-1).

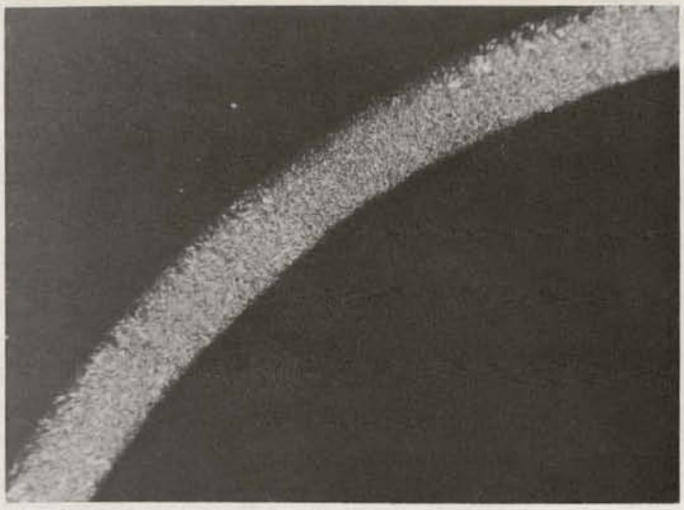

Transverse view - 50X

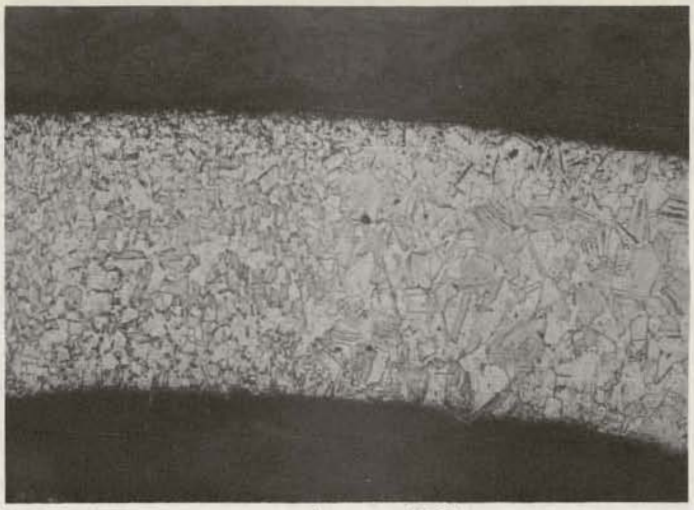

Transverse view - 150X

Figure 1.30 Swage-compacted fuel-rod cladding from sample JK-A7 and -A8 containing -400 mesh Spencer swageable grade uranium dioxide.

Transverse view - 50X

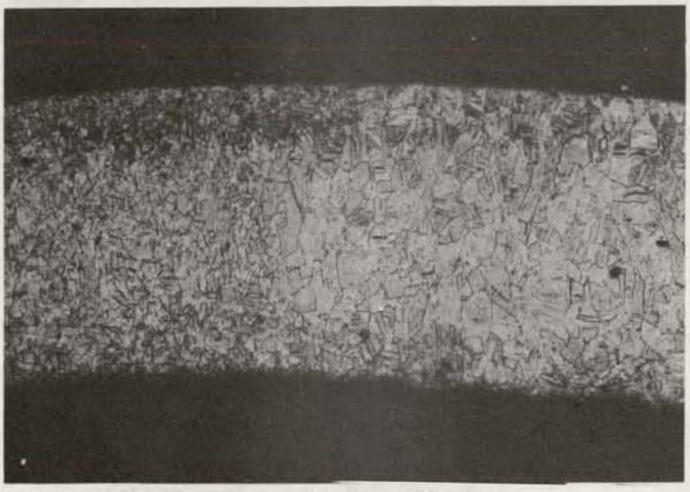

Transverse view - 150X

Figure 1.31 Swage-compacted fuel-rod cladding from sample JK-A9 containing -325+400 mesh Spencer swageable grade uranium dioxide.

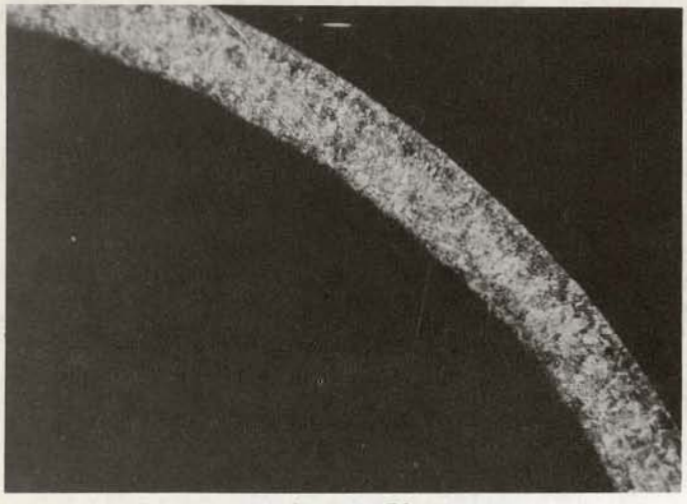

Transverse view - 50X

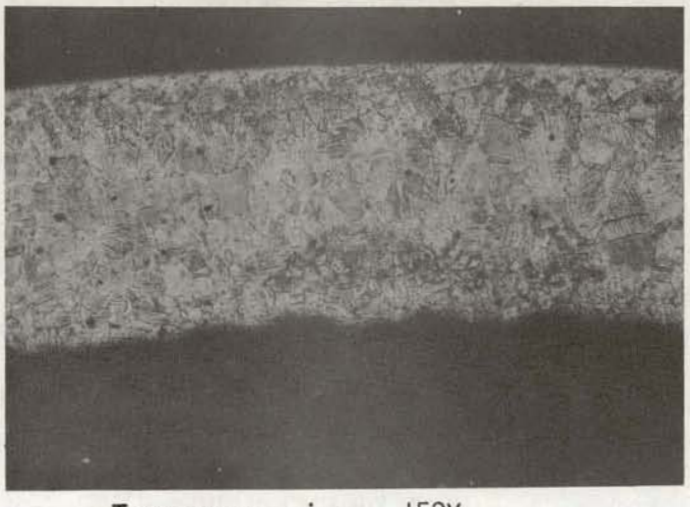

Transverse view - 150X

Figure 1.32 Swage-compacted fuel-rod cladding from samples JK-A10 and -A11 containing -170+325 mesh Spencer swageable grade uranium dioxide.

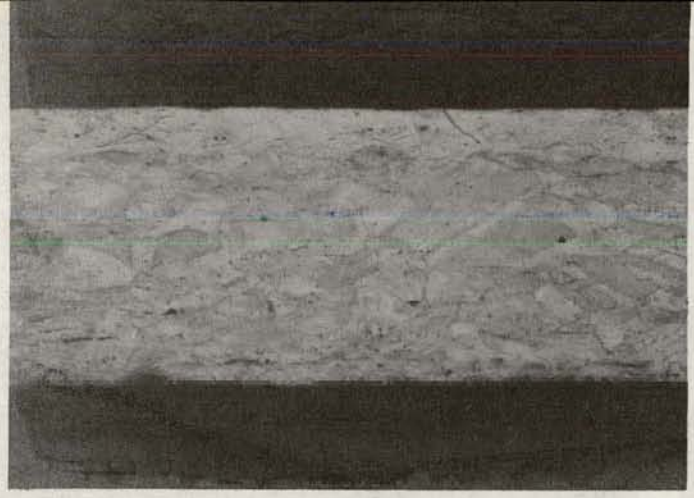

Longitudinal view - 150X

Clad inside surface - 70X

(NP Photos 15A-22-2, 15A-22-3, 15A-22b-1, and 15A-22-1).

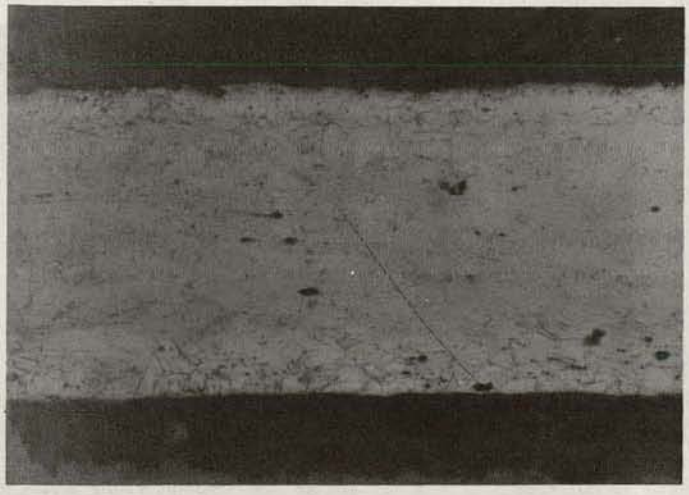

Longitudinal view - 150X

Clad inside surface - 70X

(NP Photos 15A-23-2, 15A-23-1, 15A-23b-1, and 15A-23c-1).

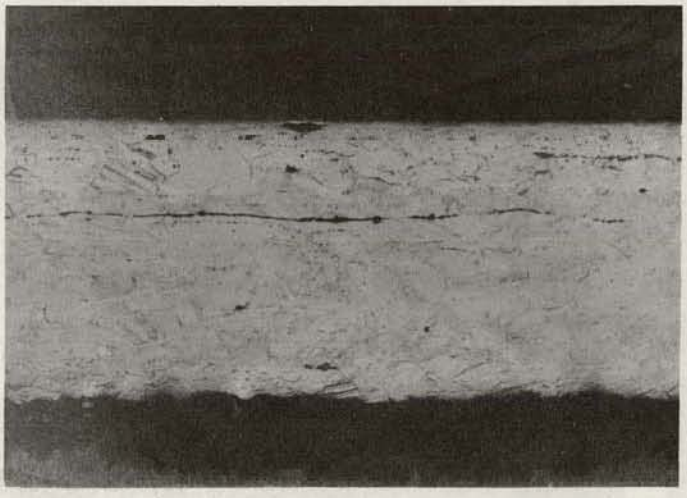

Longitudinal view - 150X

Clad inside surface - 70X

(NP Photos 15A-24-2, 15A-24-1, 15A-24b-1, and 15A-24c-1).

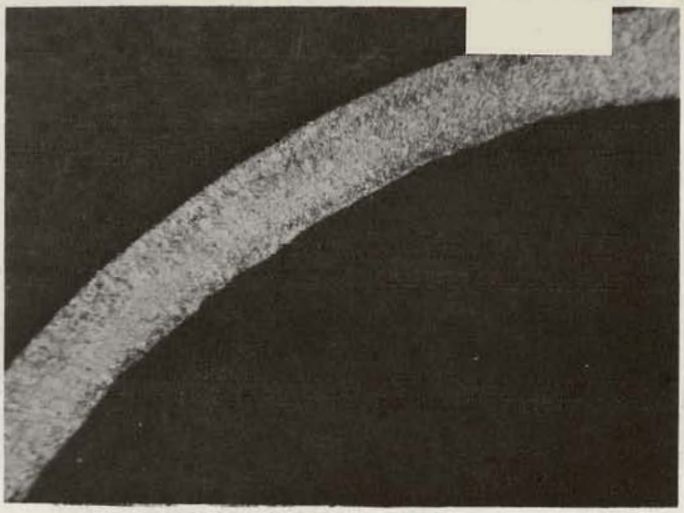

Transverse view - 50X

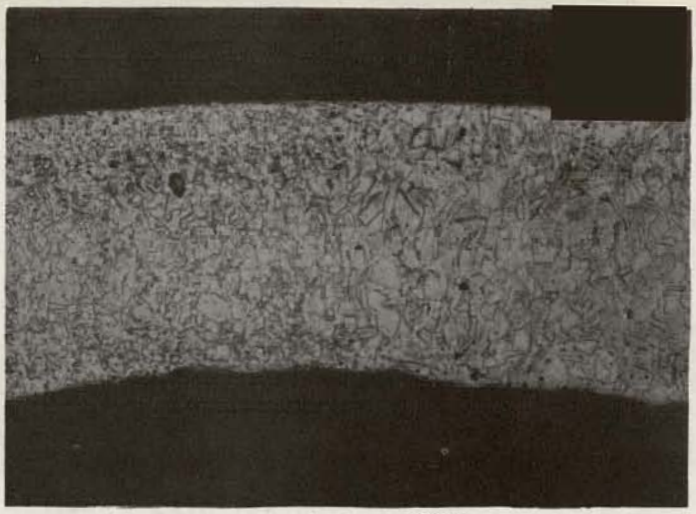

Transverse view - 150X

Figure 1.33 Swage-compacted fuel-rod cladding from samples JK-A12 and -A13 containing -140+325 mesh Spencer swageable grade uranium dioxide.

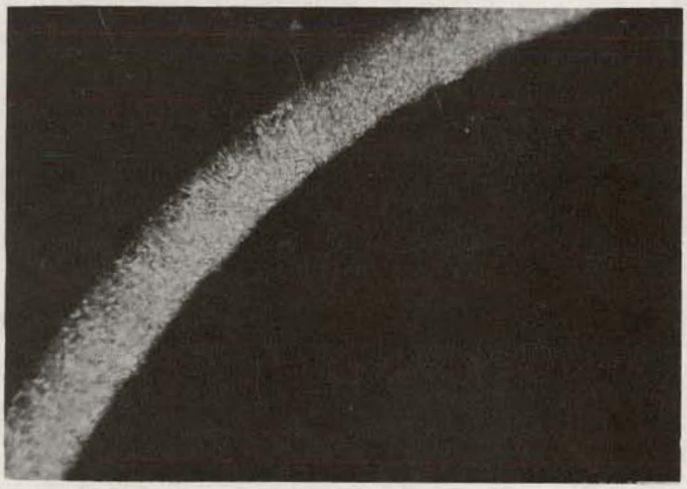

Transverse view - 50X

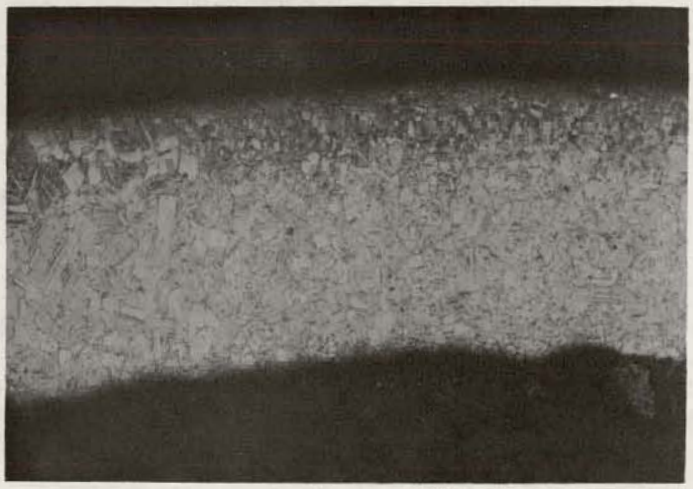

Transverse view - 150X

Figure 1.34 Swage-compacted fuel-rod cladding from samples JK-A14 and -A15 containing -100 +325 mesh Spencer swageable grade uranium dioxide.

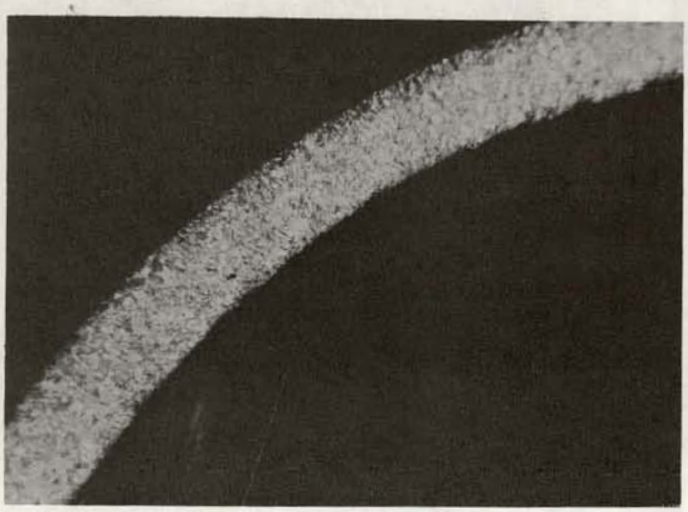

Transverse view - 50X

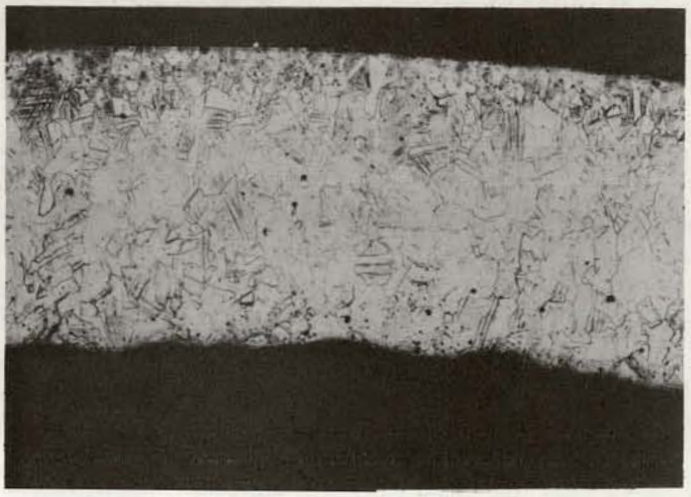

Transverse view - 150X

Figure 1.35 Swage-compacted fuel-rod cladding from samples JK-A16 and -A17 containing -70+170 mesh Spencer swageable grade uranium dioxide.

Longitudinal view - 150X

Clad inside surface - 70X

(NP Photos 15A-27-2, 15A-27-1, 15A-26b-1, and 15A-26c-1).

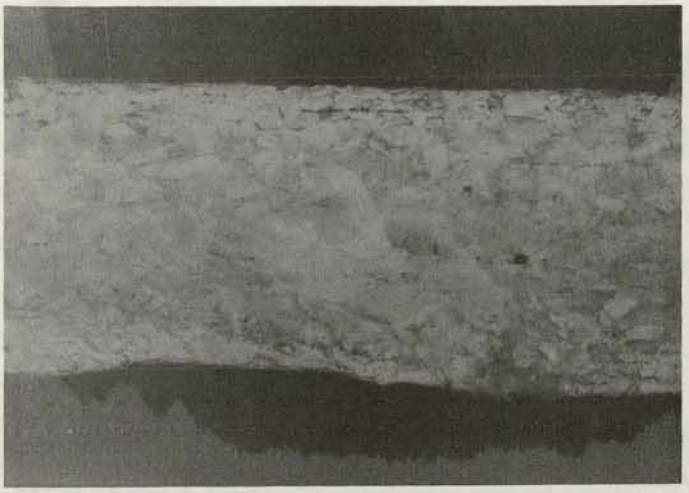

Longitudinal view - 150X

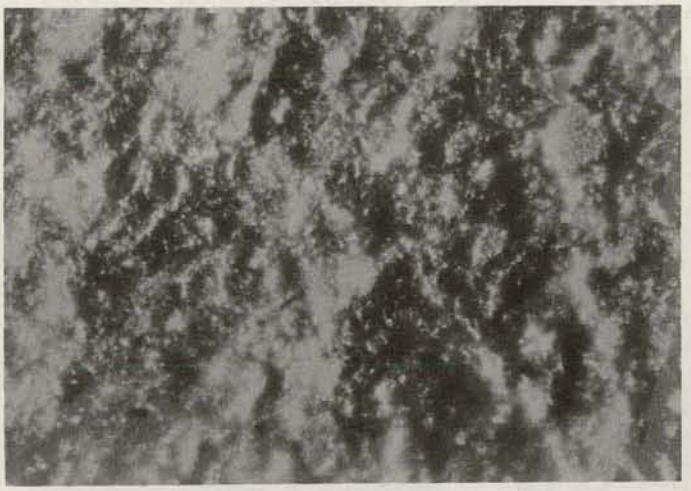

Clad inside surface - 70X

(NP Photos 15A-29-2, 15A-20-1, 15A-28b-2, and 15A-28c-1).

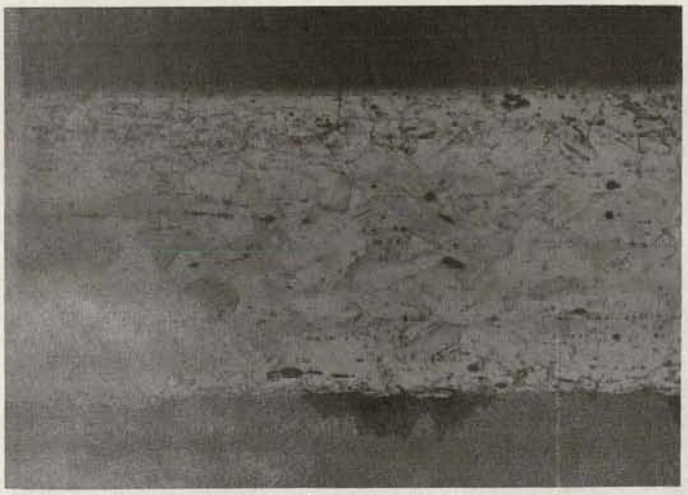

Longitudinal view - 150X

Clad inside surface - 70X

(NP Photos 15A-31-2, 15A-31-1, 15A-31b-2, and 15A-31c-1).

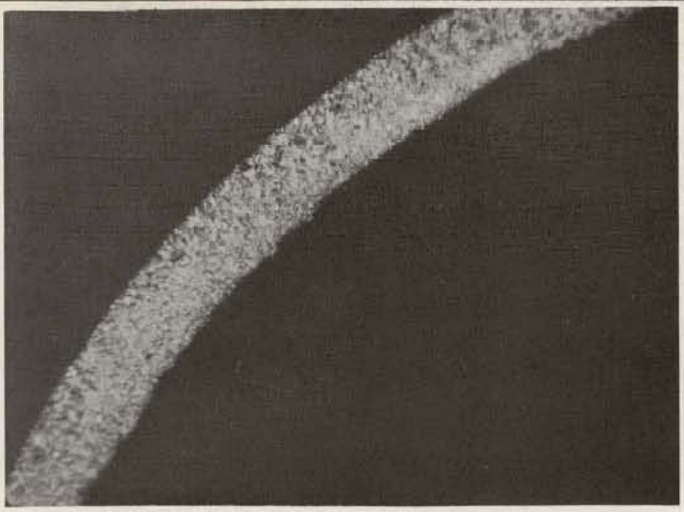

Transverse view - 50X

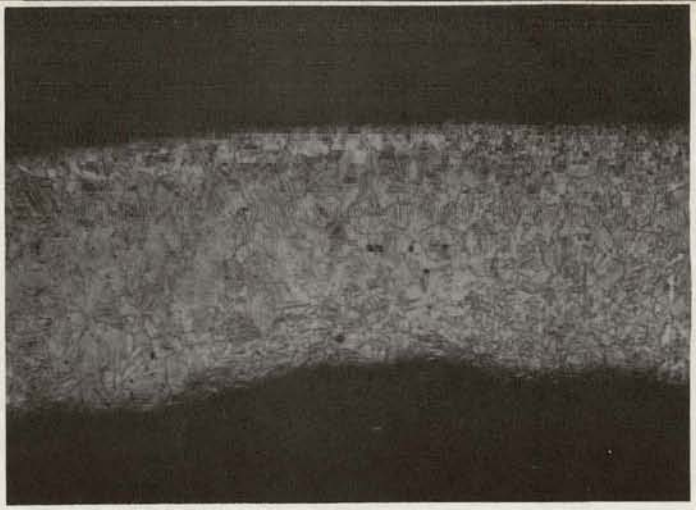

Transverse view - 150X

Figure 1.36 Swage-compacted fuel-rod cladding from sample JK-A18 containing -70+140 mesh Spencer swageable grade uranium dioxide.

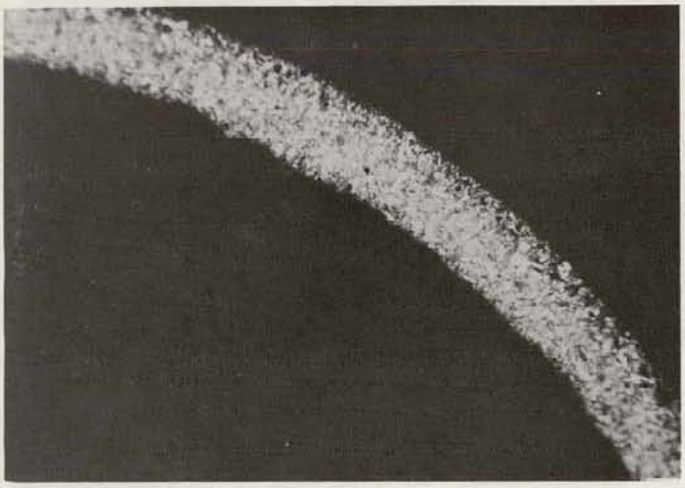

Transverse view - 50X

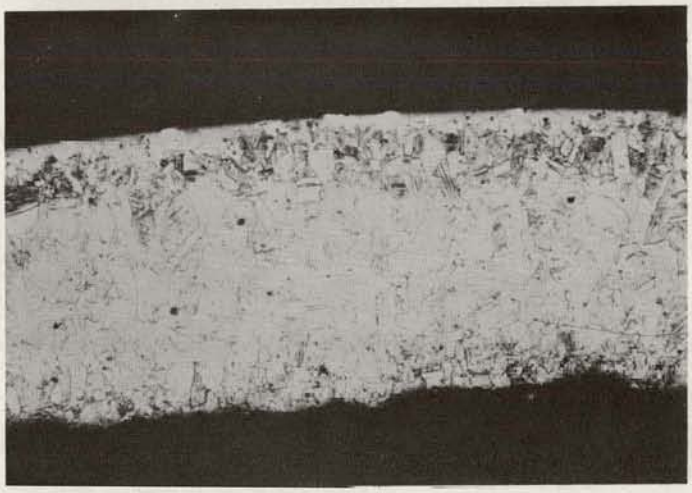

Transverse view - 150X

Figure 1.37 Swage-compacted fuel-rod cladding from sample JK-A19 containing -70+140 mesh Spencer swageable grade uranium dioxide.

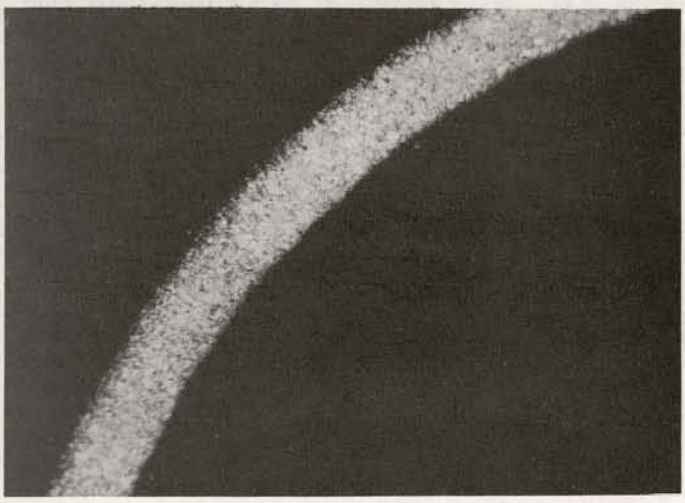

Transverse view - 50X

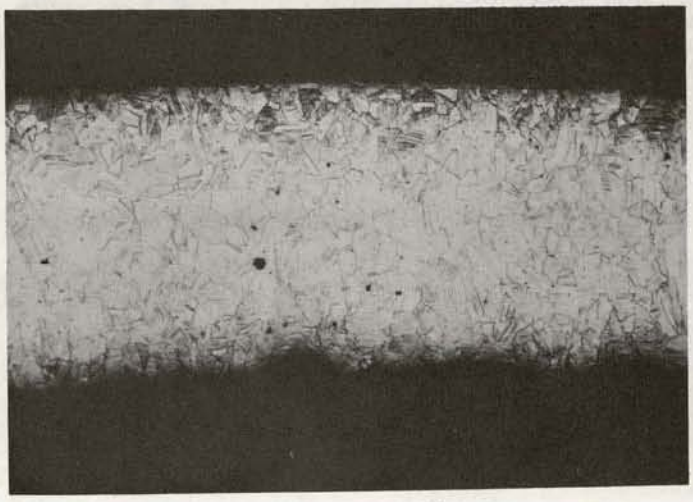

Transverse view - 150X

Figure 1.38 Swage-compacted fuel-rod cladding from samples JK-A20 and -A21 containing -70+100 mesh Spencer swageable grade uranium dioxide.

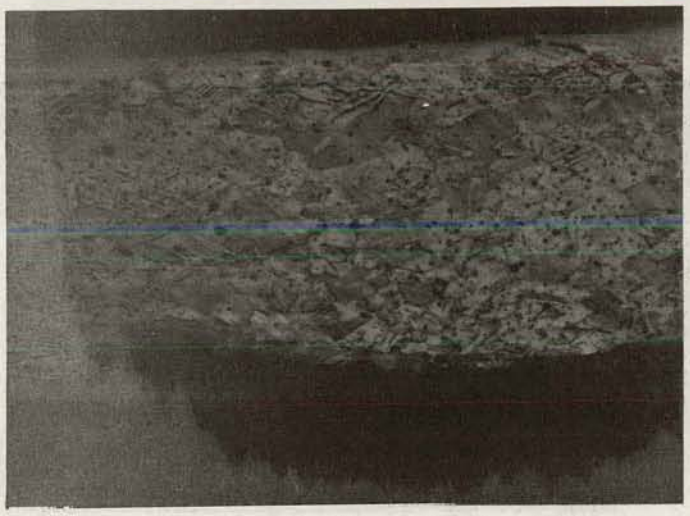

Longitudinal view - 150X

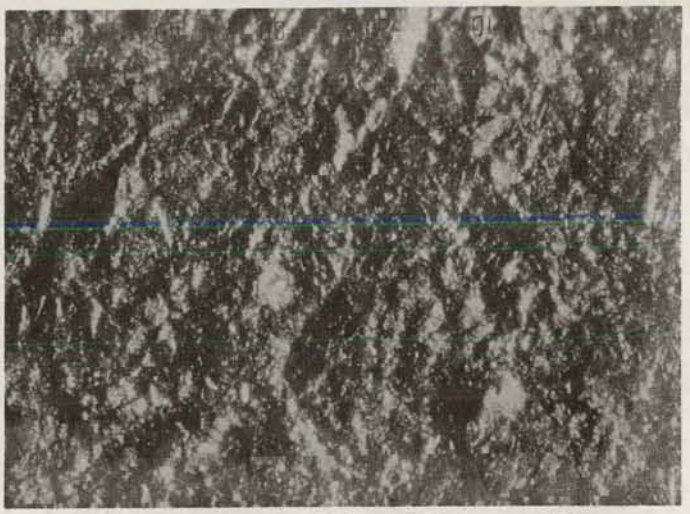

Clad inside surface - 70X

(NP Photos 15A-32-2, 15A-32-1, 15A-32b-1, and 15A-32c-1).

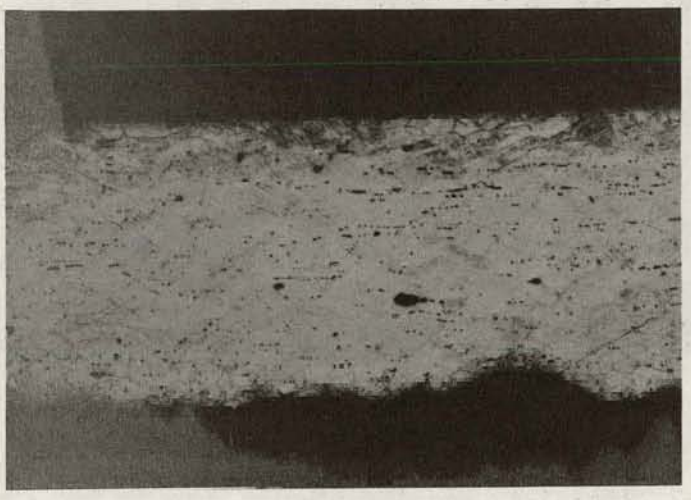

Longitudinal view - 150X

Clad inside surface - 70X

(NP Photos 15A-33-2, 15A-33-1, 15A-33b-2, and 15A-33c-1).

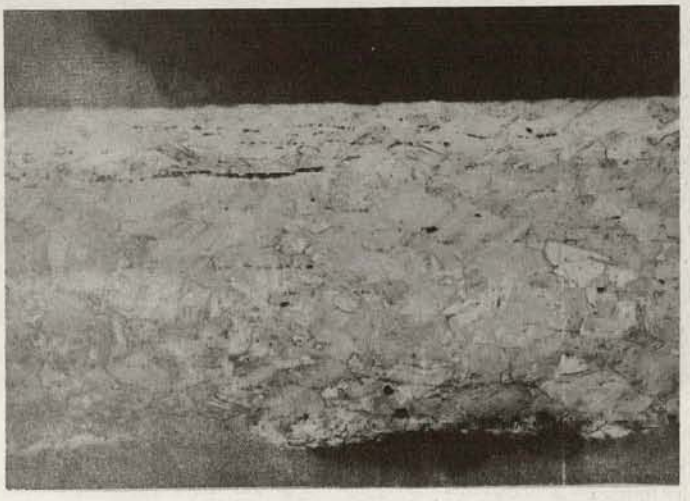

Longitudinal view - 150X

Clad inside surface - 70X

(NP Photos 15A-35-2, 15A-35-1, 15A-35-3, and 15A-35-4).

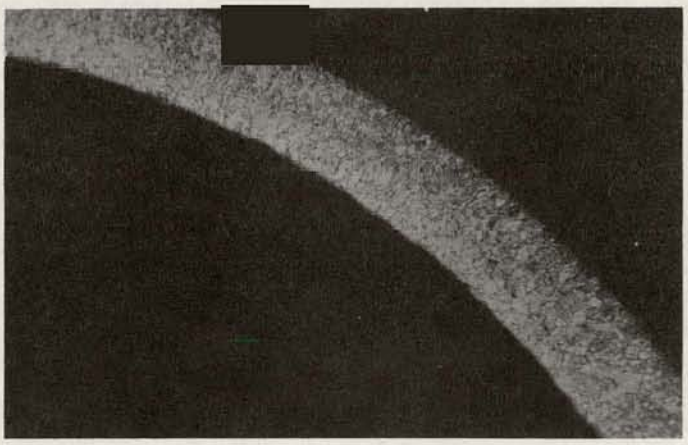

Transverse view - 50X

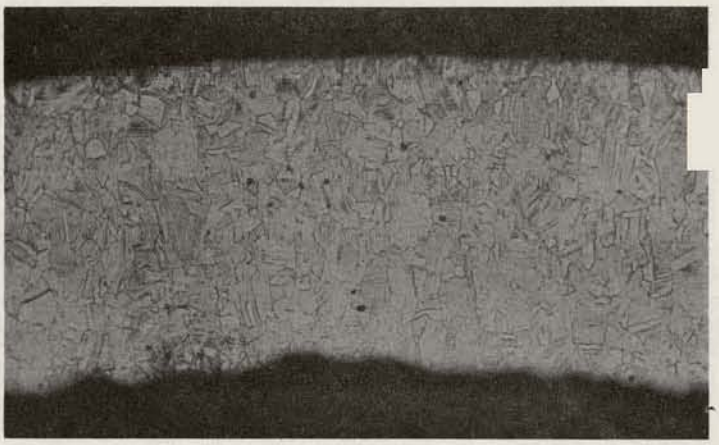

Transverse view - 150X

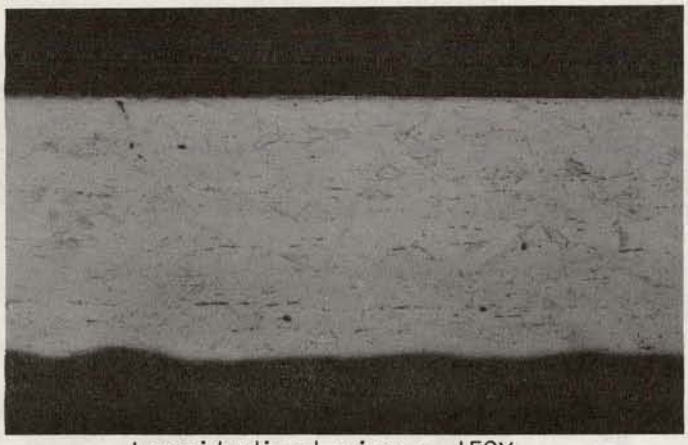

Longitudinal view - 150X

Clad inside surface - 70X

Figure 1.39 Swage-compacted fuel-rod cladding from sample JK-A33 containing -140+170 mesh Spencer swageable grade uranium dioxide. (NP Photos 15A-53-1, 15A-53-2, 15A-53-4, and 15A-53-6)

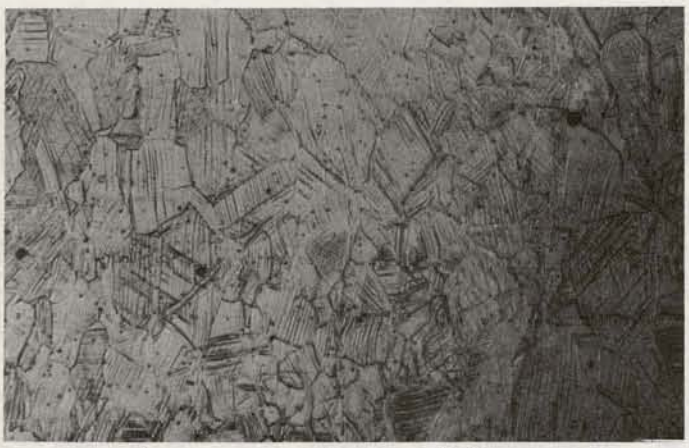

Transverse view - 300X

Longitudinal view - 300X

Figure 1.40 Heavily worked cladding surfaces of sample JK-A33 showing deformation twinning. (NP Photos 15A-53-3 and 15A-53-5).

Metallographic examination of the cladding shows a difference in the grain structure of the inside and outside surfaces from the center of the clad. This is particularly noticeable in Figure 1.35 and 1.37. The surface grains show the largest degree of deformation as is clearly evident by the deformation twinning shown in Figure 1.40. This analysis of the cladding is being continued and will be reported in the next quarterly report.

Effects of the Percentage Reduction in Cross Sectional Area. Two alumina-filled tubes were swaged to determine the gross effects of larger reductions in cross sectional area. One rod was made with 0.350-in o.d. stainless steel tubing with a 0.010-in thick wall. The second rod was made with a 0.370-in. o.d. tube with a 0.010-in thick wall. Both tubes were filled with the same batch of alumina used in previous studies. After crimping the ends, vibratory tap packing, and welding of ends, the tubes were swaged successively through 0.250-in and 0.225-in dies. The final diameter of the swaged tubes was 0.220 to 0.221 in. Further data for the samples is given in Table 1.9.

In addition to the alumina-filled rods, twelve uranium dioxide filled rods 0.370-, 0.350-, and 0.330-in o.d. were reduced to a standard size of 0.220 in o.d. The reductions corresponded to reductions of 64.6, 60.5, and 55.5 per cent in cross sectional area, respectively. The uranium dioxide powder was sized into various mesh fractions. Variables and results are given in Table 1.10.

TABLE I.9 PROPERTIES OF SWAGE COMPACTED AL_2O_3 RODS

Sample Number	JKI-1	JKI-2
Mesh size	as-received	as-received
Reduction in Area	64.6 per cent	60.5 per cent
Original Clad Tube Diameter	0.370 in.	0.350 in.
Final Diameter	0.220 in.	0.220 in.
Elongation	49.4 per cent	35.0 per cent
Surface Appearance	VG	VG

Views of the as-received tubing are shown in Figures I.41 through I.43. This tubing, which was supplied by Superior Tube Co., compares favorably with the tubing supplied by the Trent Tube Co. (Figure I.26). The former, however, has a slightly larger grain size and a slightly rougher inside diameter.

Four views of the 0.370-in o.d. tubing filled with alumina and reduced to 0.220-in o.d. are shown in Figure I.44. The photomicrographs show the clad to be heavily worked. Cracks appear in the 150 transverse view. The inside surface of the clad is relatively rough.

The first four samples containing -400 mesh uranium dioxide were made to determine the effect of increasing the reduction in cross sectional area. The first two samples, 64.6 and 60.5 per cent reduction, had radial cracking, presumably due to the large reduction. The second two tubes were satisfactory.

TABLE I.10 PROPERTIES OF SWAGE-COMPACTED URANIUM DIOXIDE

JKI-A & JKI-B SERIES

SAMPLE NUMBER	MESH SIZE	TAP DENSITY	REDUCT. SCHEDULE [1]	REDUCT. IN AREA	ELONG.	FINAL DIAMETER	DENSITY PERCENT OF THEORETICAL	SURFACE APPEARANCE [2]
		(Percent)		(Percent)	(Percent)	(in.)		
JKI-A1	-400	48.1	4	64.6	-----	0.221	87.65±0.15	TC
JKI-A2	-400	48.1	5	60.5	85	0.221	74.66±0.46	TC
JKI-A3	-400	48.1	6	55.5	60	0.221	74.5±3.2	VG
JKI-A4	-400	48.1	7	55.5	56	0.221	89.3	VG
JKI-B1	-70+80	50.2	8	60.5	-----	0.221	87.9±0.1	VG
JKI-B2	-80+100	54.8	8	60.5	77	0.220	88.0±0.5	VG
JKI-B3	-100+120	51.2	8	60.5	-----	0.220	86.3±0.7	VG
JKI-B4	-120+140	50.4	8	60.5	74	0.220	86.9±0.6	VG
JKI-B5	-170+200	47.6	8	60.5	66	0.220	86.3±0.4	VG
JKI-B6	-200+230	49.1	8	60.5	63	0.220	87.8±0.6	VG
JKI-B7	-270+325	48.5	8	60.5	-----	0.221	87.0±0.8	VG
JKI-B8	-400	48.1	8	60.5	89	0.220	82.8±0.5	VG

1 Reduction Schedules: 4(0.370 to 0.275 to 0.225); 5(0.350 to 0.275 to 0.225); 6(0.330 to 0.275 to 0.225); 7(0.330 to 0.225 electric drill feed); 8(0.350 to 0.250, Annealed to 0.225).

2 Surface Appearance: TC = transverse cracking; VG = very good.

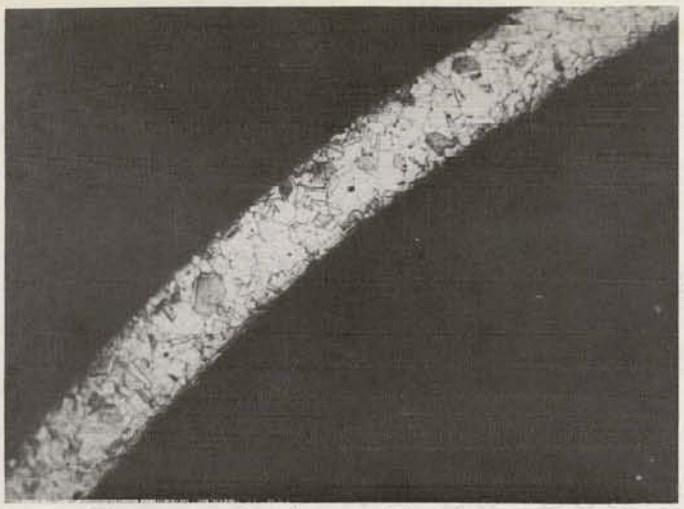

Transverse view - 50X

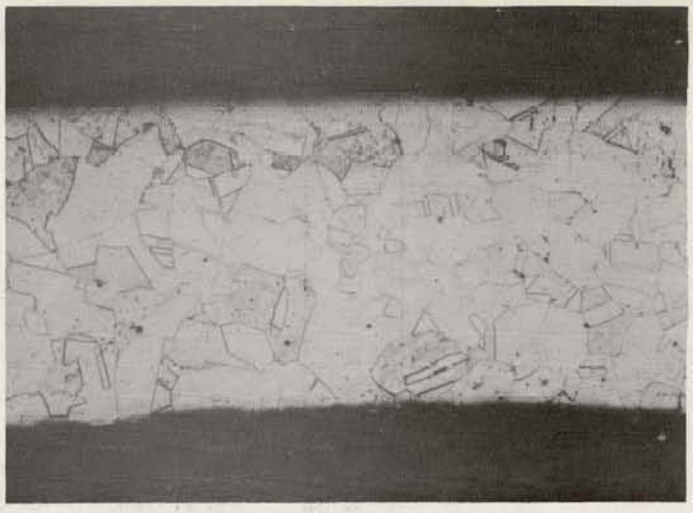

Transverse view - 150X

Figure 1.41 As-received 316L stainless steel tubing, 0.010-in thick wall, 0.370-in o.d. (Superior Tube Co.)

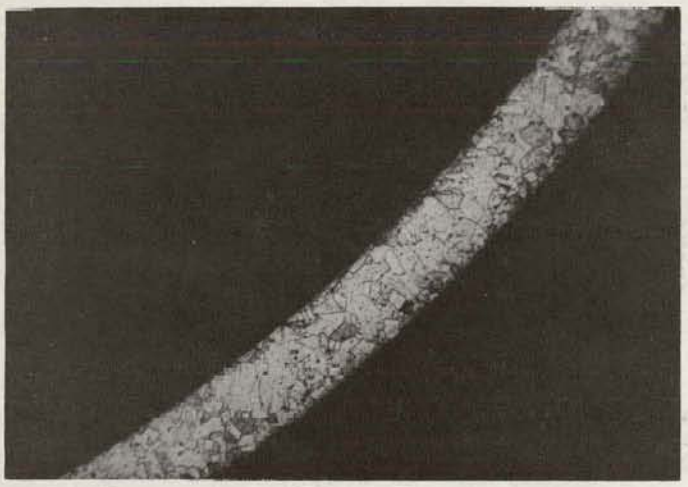

Transverse view - 50X

Transverse view - 150X

Figure 1.42 As-received 316L stainless steel tubing, 0.010-in thick wall, 0.350-in o.d. (Superior Tube Co.)

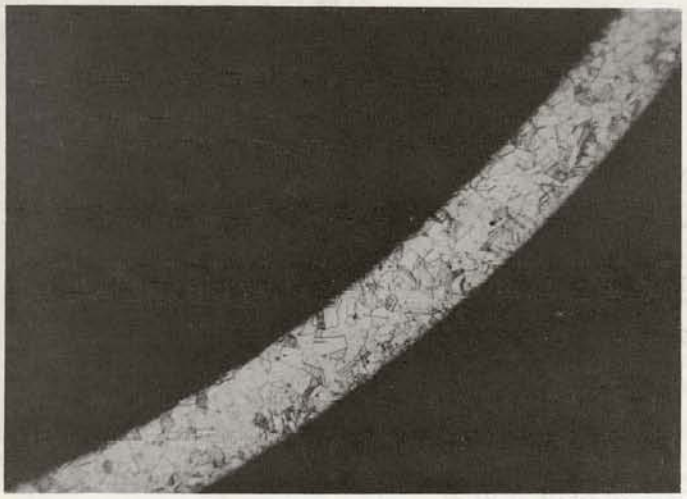

Transverse view - 50X

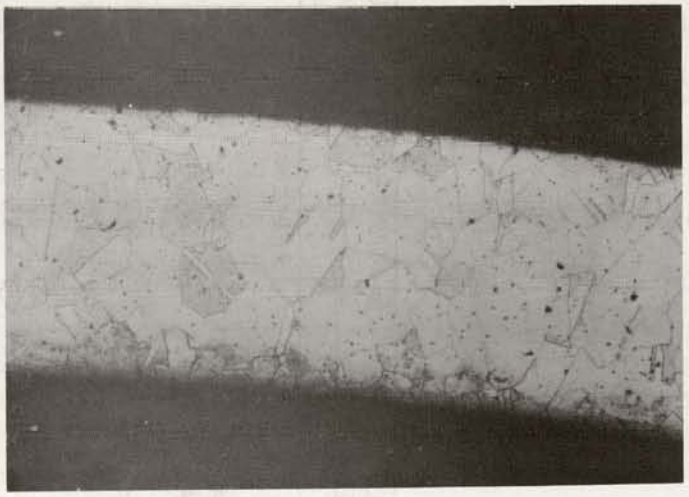

Transverse view - 150X

Figure 1.43 As-received 316L stainless steel tubing, 0.010-in thick wall, 0.330-in o.d. (Superior Tube Co.)

Longitudinal view - 150X

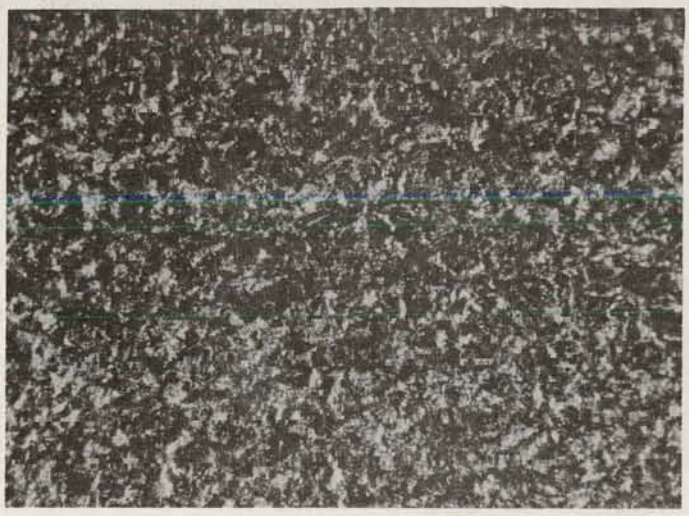

Clad inside surface - 70X

(NP Photos 15A-36-3b, 15A-36-3, 15A-36-3d, and 15A-36-3c)

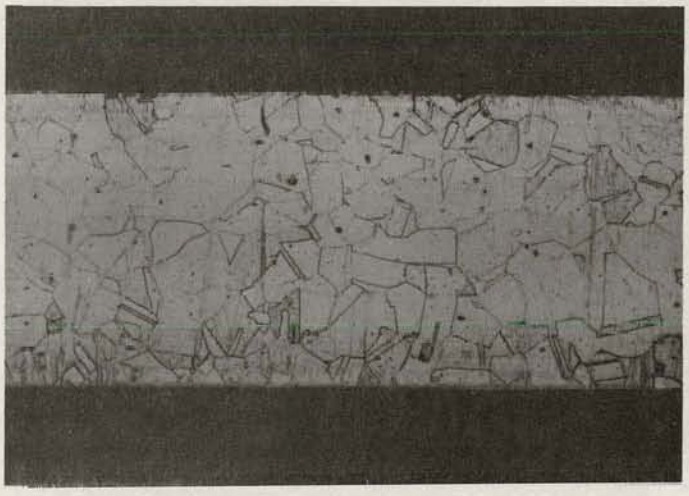

Longitudinal view - 150X

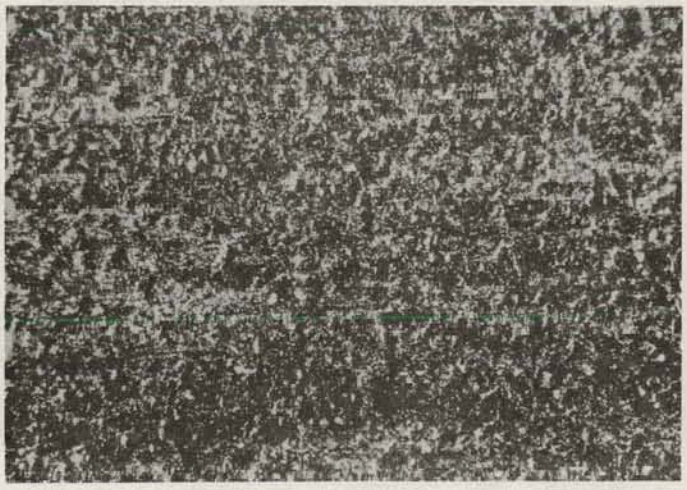

Clad inside surface - 70X

(NP Photos 15A-36-2b, 15A-36-1, 15A-36-2d, and 15A-36-2c)

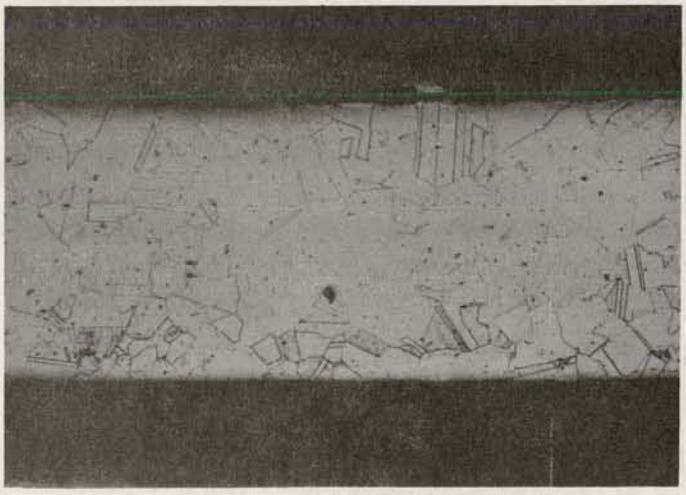

Longitudinal view - 150X

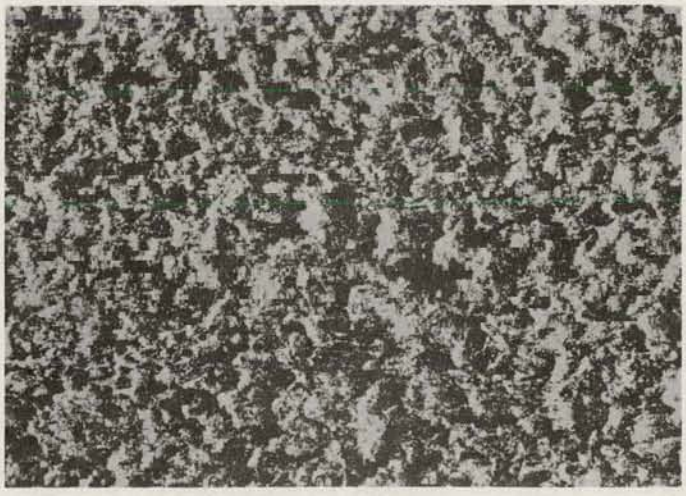

Clad inside surface - 70X

(NP Photos 15A-36-1b, 15A-36-2, 15A-36-1d, and 15A-36-1c)

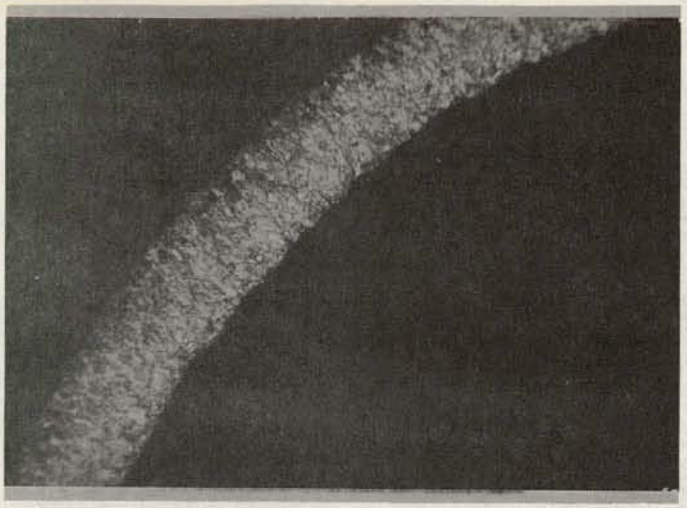

Transverse view - 50X

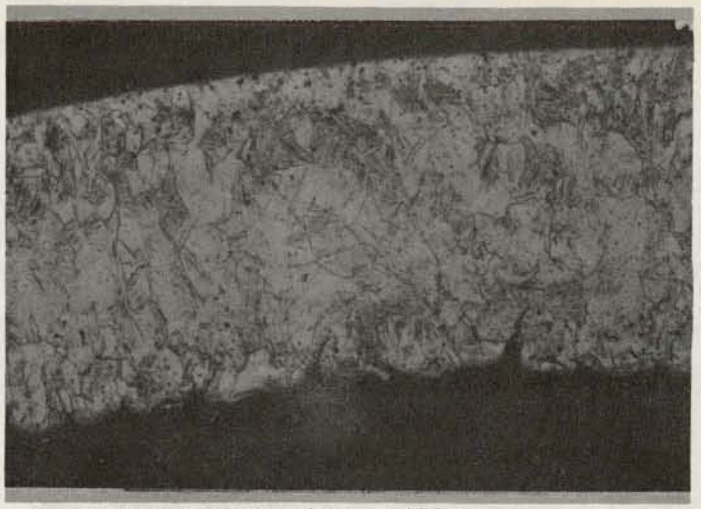

Transverse view - 150X

Figure I.44 Swage-compacted fuel-rod cladding from specimen JKI-I containing alumina and reduced 64.6 per cent.

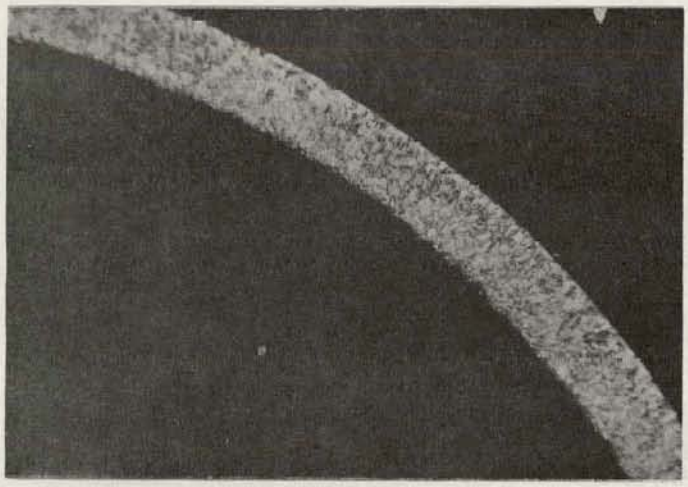

Transverse view - 50X

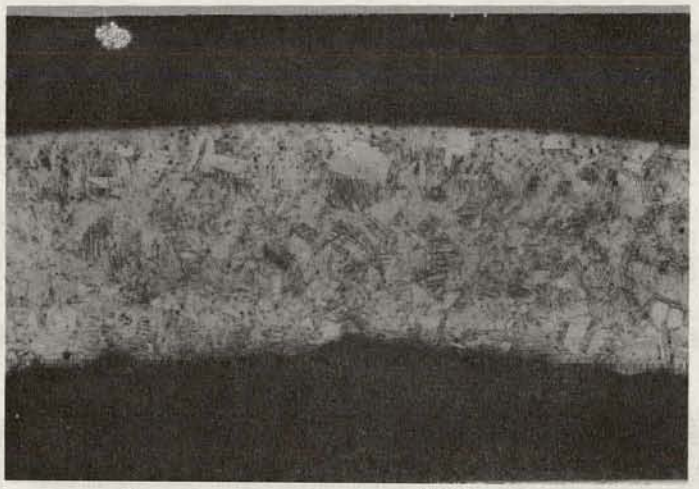

Transverse view - 150X

Figure I.45 Swage-compacted fuel-rod cladding from sample JKI-AI containing -400 mesh oxide swaged to 64.6 per cent reduction.

Figure I.45 shows four magnifications of the effects on the tube reduced 64.6 per cent. Although these photomicrographs do not show any hoop stress or radial cracking, the inner and outer surface of the clad is obviously heavily worked.

The series of tubes designated JKI-B contained uranium dioxide of mesh fractions corresponding to the series JK-A reported in Table

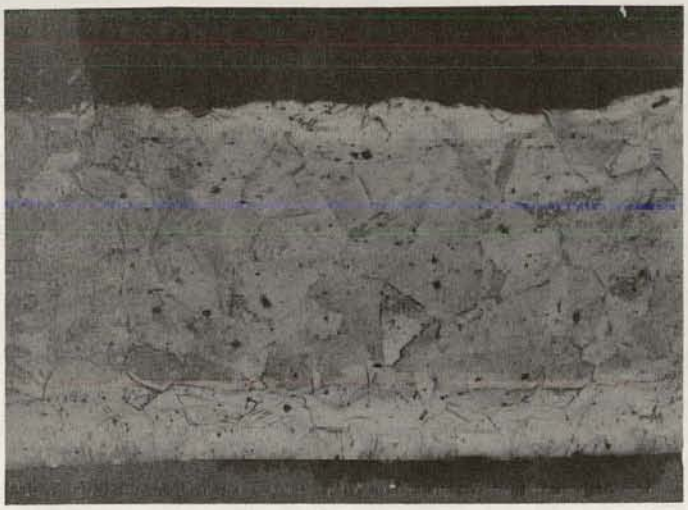

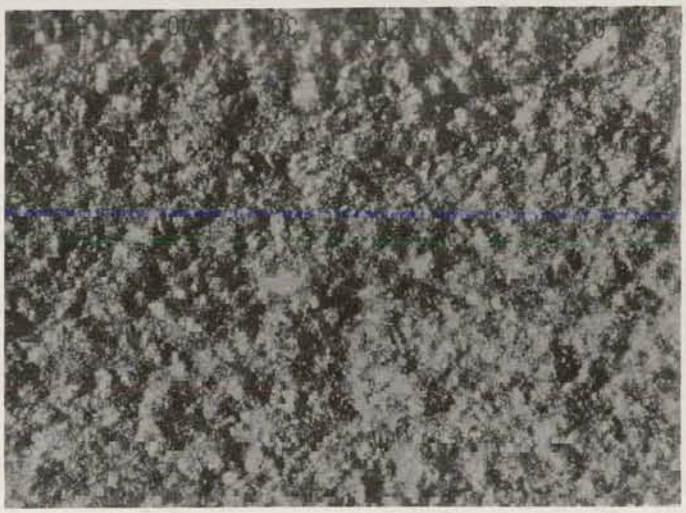

Longitudinal view - 150X

Clad inside surface - 70X

(NP Photos 15A-37-2, 15A-37-1, 15A-37b-1, and 15A-37-4)

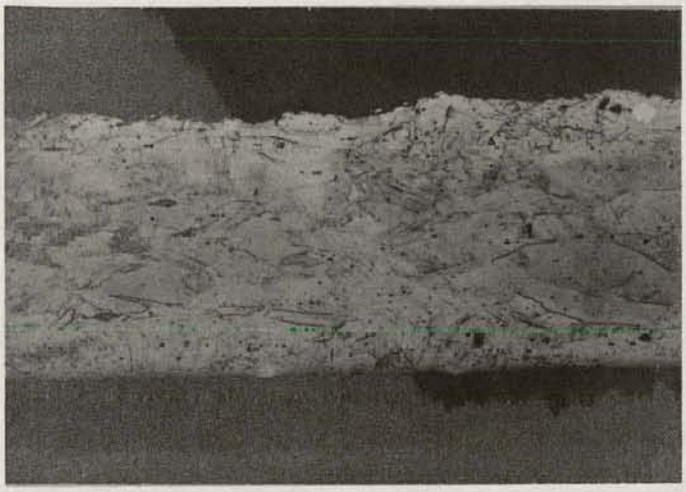

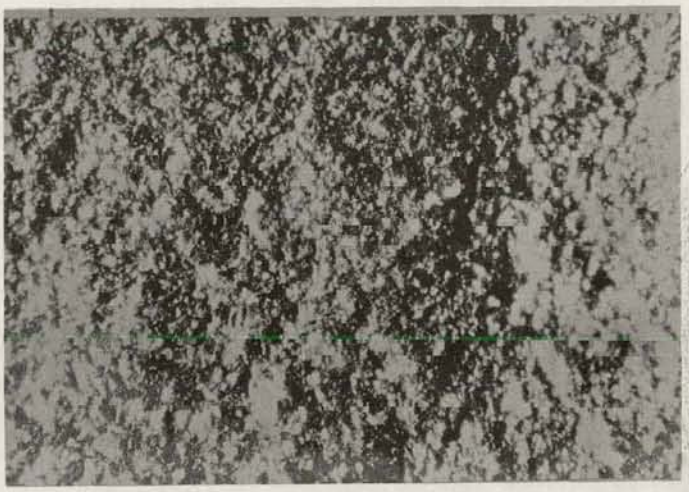

Longitudinal view - 150X

Clad inside surface - 70X

(NP Photos 15A-38-3, 15A-38-2, 15A-38-7, and 15A-38-6)

1.8. The powder was vibratory packed in 0.350-in o.d. tubing and reduced to 0.220 (60.5 per cent). Details of this series is also given in Table 1.10.

Lower swaged densities were obtained with the larger reduction in cross sectional area as is evident by comparing corresponding mesh fractions in Tables 1.8 and 1.10. Metallographic examination of the tubes will be made during the next quarter.

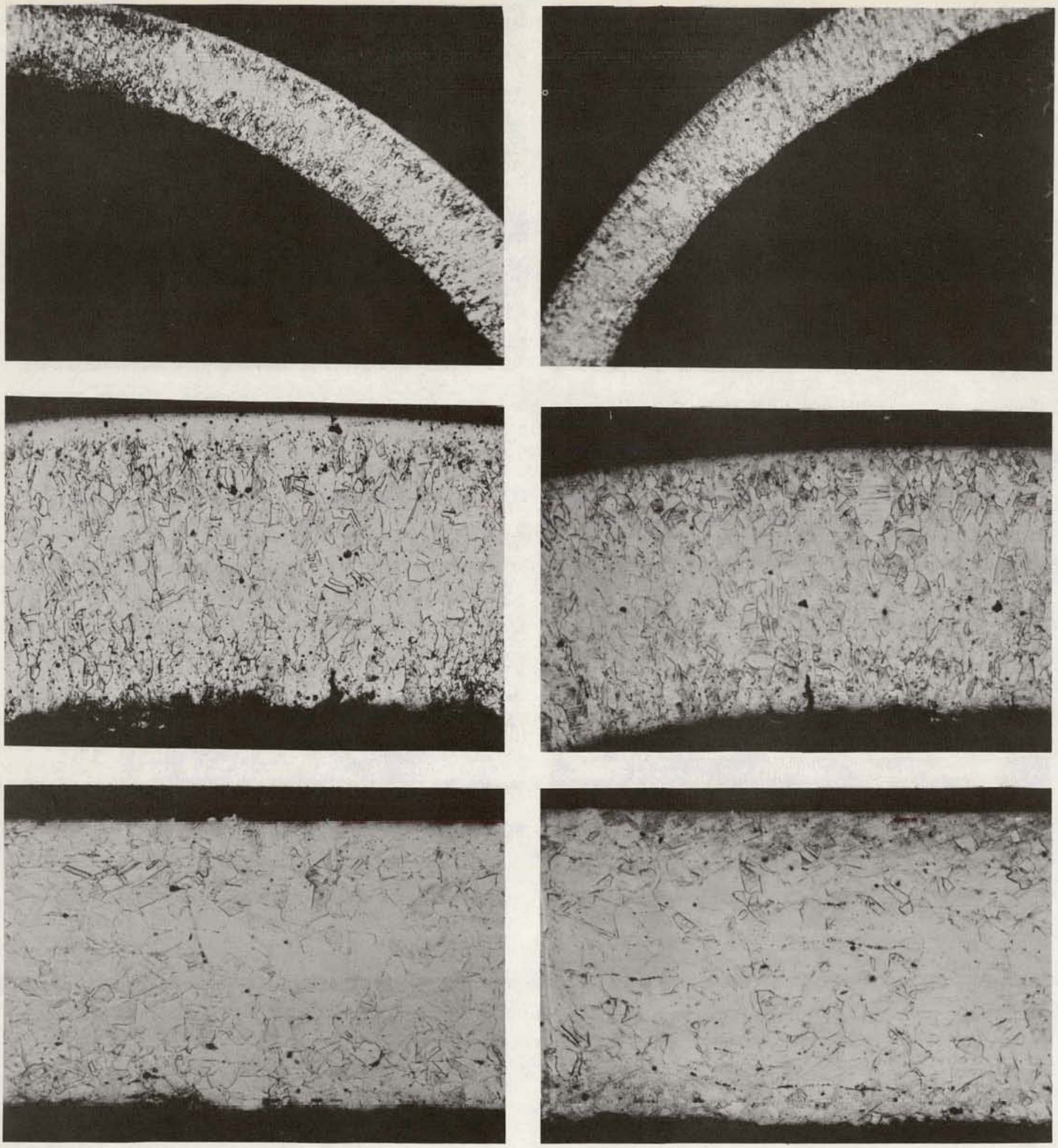

Figure 1.46 Swage-compacted alumina-filled fuel-rod cladding reduced from 0.325 to 0.250 to 0.225 in. o.d. (54.1 per cent) and straightened in 5-roll (left) and 6-roll (right) rotary straighteners. Top to bottom: transverse 50X, transverse 150X, and longitudinal 150X. (NP Photos 24A-3-2, -1, -3 (left); and 24A-9-2, -1, and -3 (right).

Effect of Rotary Straightening on Clad. Before assembly into fuel elements, the fuel rods must be straightened. The effect of rotary straightening on the clad was therefore evaluated. Eight swaged alumina-filled rods were reduced 54.1 per cent. Four were run through a 5-roll rotary straightener; four were run through a 6-roll straightener. Characteristic results are shown in Figure 1.46. Results with the two straighteners is comparable. However, due to the work hardened condition of the cladding tubes following swaging, cracking occurred on the inside clad surface. This indicates that an annealing heat treatment may be necessary prior to straightening.

1.6.4.4. Rare Earth Burnable Poison. A minor effort was continued on the study of a rare earth burnable poison material for the low - enrichment superheater fuel element. The object of the study is to develop a dispersion of gadolinium oxide of closely controlled particle size in a ceramic matrix. The study is being conducted in three phases: 1) a study of any possible high-temperature reactions between gadolinium oxide and alumina matrix material; 2) fabrication of gadolinium oxide of a closely controlled particle size; and 3) fabrication of ceramic alumina pellets.

Reaction between Gadolinium Oxide and Alumina. The high-temperature reaction between aluminum oxide and gadolinium oxide is being studied to determine the suitability of using aluminum oxide as the ceramic matrix. During the quarter two series of four pellets were pressed

and sintered. The first series of four was made from a 80-to-20 weight ratio mixture of gadolinium oxide and alumina. The mixture was mixed with 2 w/o carbowax lubricant-binder and pressed into pellets at 26 tsi. The second series of pellets was made of a layer of gadolinium oxide with a layer of alumina. The relative amounts of powder were 50:50. Each powder was mixed with 4 w/o Carbowax. The alumina was loaded into a die, and the gadolinium oxide was loaded on top. The composite was pressed at 26 tsi.

Both series of pellets were sintered in a hydrogen atmosphere furnace. They were first out-gassed at 250 to 450 C for 12 hr. The temperature was then increased 100 C/hr until reaching 1510C (2750 F). This temperature was maintained for 17 hr. The temperature was then reduced by 100 C/hr to 900 C (1652 F), at which time the pellets were taken out of the furnace.

Pellets in the first series were sound and of good strength. Alumina had been used to cover the pellets in the sintering boat, and some of this alumina had adhered to the surface of pellets. The surface was yellowish-white in color.

The second series of pellets was of lower quality. The gadolinium-oxide half of the pellets shrunk much more than the alumina half. Of the four pellets, three were intact; but one pellet separated at the powder interface during subsequent handling.

The possibility of any mutual solid solubility or high-temperature reaction between the two materials will be determined by metallographic examinations during the next quarter.

Fabrication of Gadolinium Oxide Powder of Closely Controlled Particle Size. The object of this study is to prepare gadolinium oxide of uniform particle size by pelleting as-received powder, sintering, ball-milling, and sieve sizing the powder. Two series of pellets were prepared. The first series (6 pellets) were pressed from as-received powder containing 4 w/o Carbowax at 26 tsi. Green pellets were of high quality with densities of 63.40 ± 0.31 percent of theoretical. The pellets were sintered according to the previously given schedule.

The as-sintered pellets had a yellowish deposit of alumina on the outside surface. A large amount of shrinkage as exhibited by hour-glassing occurred. Metallographic analysis is being made.

The second series (6 pellets) were made in the same way except that 2 w/o Carbowax was used. Green density of 5 pellets averaged 60.57 ± 0.53 per cent of theoretical. The green density of the sixth pellet was 69.06 per cent theoretical, an increase for which there was no apparent reason. These pellets will be sintered next quarter.

Fabrication of Alumina Pellets. Four series of alumina pellets were pressed and sintered. The first series (4 pellets) was made of as-received alumina with 2.0 w/o Carbowax, and pressed at 40 and 50 tsi. All four pellets disintegrated when ejected from the die or in subsequent handling.

The second series were made from as-received powder with 2 w/o Carbowax. Three pellets were pressed at 40 tsi; one was pressed at 50 tsi. The pellet pressed at 50 tsi disintegrated, but the three pressed at 40 tsi remained sound. The green density was 61.23 ± 0.08

per cent. These three pellets were out-gassed for 12 hr at 250 to 450 C. The temperature was increased 100 C/hr to 1510 C (2750 F) where the temperature was maintained for 17 hr. The temperature was then reduced slowly to 900 C (1652 F), and the pellets were removed from the furnace.

Density measurements and metallographic analysis of these pellets is being made. The as-sintered pellets were white in color with only a small amount of bubbled alumina from the sintering boat attached to the surface.

A third series (6 pellets) were made of as-received alumina powder with 4 w/o Carbowax. The pellets were pressed at 40, 50, 60, and 70 tsi. Green densities ranged from 62.2 to 65.0 per cent of theoretical, from the lower to higher forming pressures. The pellets were sintered to the same cycle described above, and were sound. Analysis is now being made.

A fourth series (4 pellets) was made of -325 mesh 99-percent pure alumina powder. This powder, which was retained by the 325 mesh screen, consisted of agglomerated powder. A sub-sieve analysis of the powder gave an average particle size of 3.0 μ.

The four pellets were pressed at 26 tsi using 2 w/o Carbowax. The appearance of all green pellets was good. Green densities were about 63 per cent of theoretical. These pellets will be sintered and evaluated during the next quarter.

2. REACTOR MECHANICAL STUDIES

THIS PAGE

WAS INTENTIONALLY

LEFT BLANK

2.1 VESSEL AND STRUCTURES

The objectives of this project are as follows: 1) to perform extensive studies, conceptual engineering, design evaluations, and tests relative to the reactor vessel and structures, so as to establish reliable, safe, and improved designs for the vessel and structure; and 2) to perform investigations and tests to insure proper hydraulic design.

2.1.1 REACTOR VESSEL SHELL

Fabrication of the vessel shell is well along in the Allis-Chalmers shops. Results obtained to date from the full-scale closure demonstrate the integrity of the closure design. This test is discussed in more detail below.

2.1.2 FULL-SCALE CLOSURE TEST

2.1.2.1 Experimental Stress Analysis of Vessel Head and Flange. Tests at Room Temperature. Test data for a stress analysis of the vessel head and flange at room temperature was taken. The test set-up is shown in Figure 2.1. Strains in the head and flange were measured with electric resistance strain gages with the head bolted-up without and with hydrostatic pressure applied.

Typical measured stresses are plotted in Figure 2.2, along with a stress distribution previously calculated using a digital computer. The points show only a small portion of the data with the head bolted-up but without hydrostatic pressure. Agreement between analytical calculations and the data thus far analyzed is good.

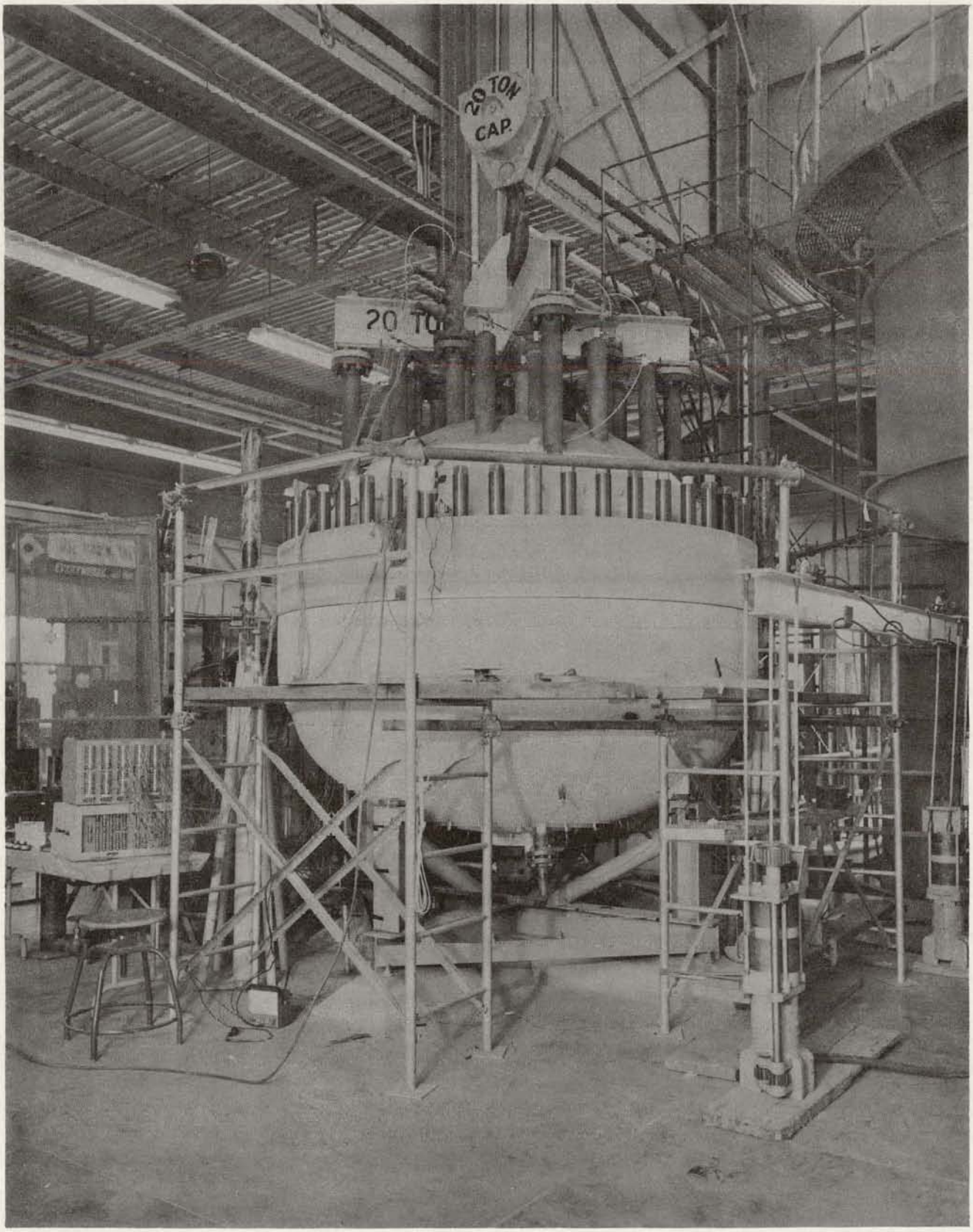

Figure 2.1 Full-scale Closure test, (A-C Photo 210756)

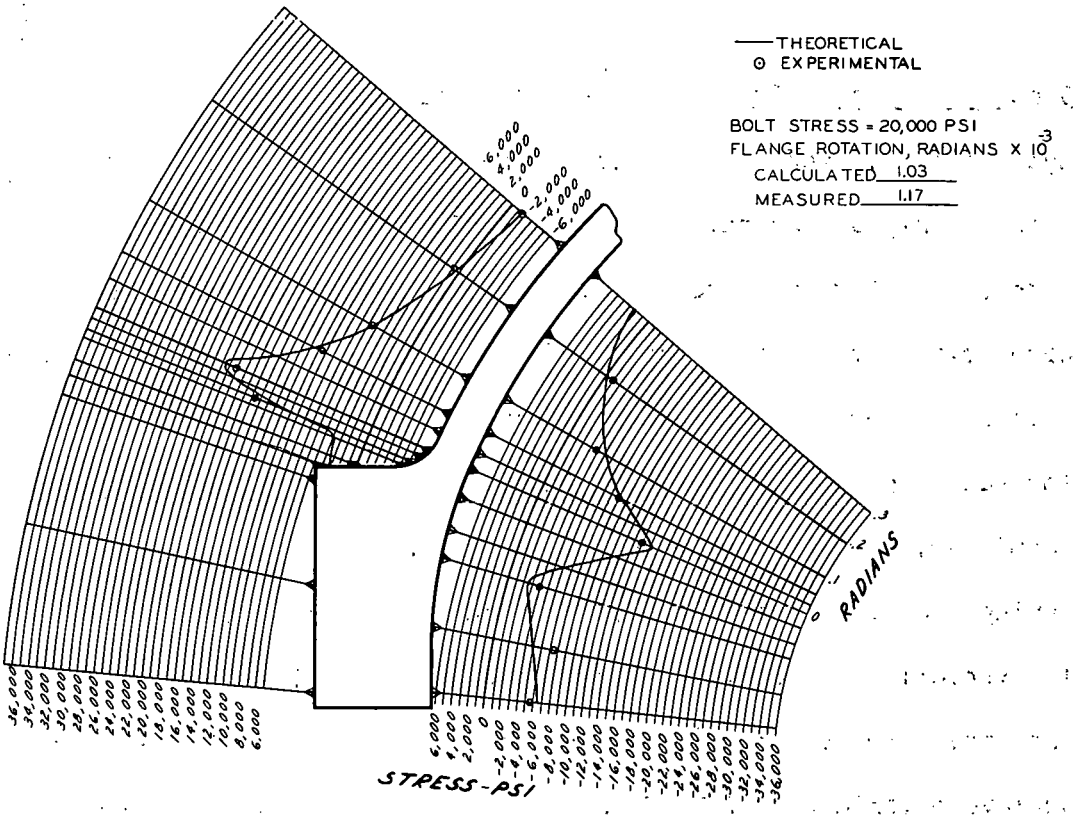

Figure 2.2 Meridional stresses in closure due to bolt load. (A-C Dwg. 43-202-105)

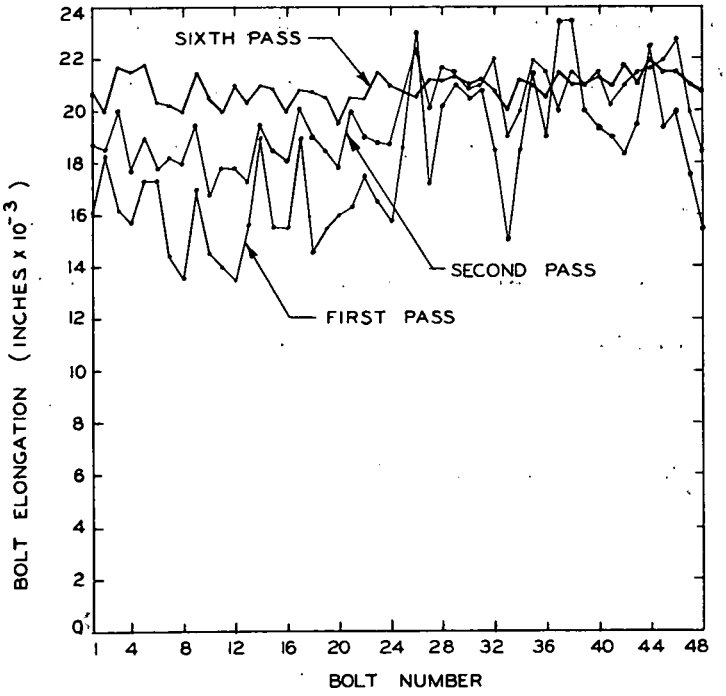

Figure 2.3 Closure test bolting up to 30,000 psi stress. (A-C Dwg. 43-024-369)

Stresses due to Bolt Load. The bolt load is applied using two hydraulic bolt tensioners. These tensioners are suspended from a handling rig and operated simultaneously on two bolts located 180° apart. The time required to make a complete pass, i.e. tightening each bolt once, is about 80 minutes. The number of passes that are necessary depend on the accuracy with which the amount of pre-stress for each stud can be predicted and the amount of deviation that is permitted. Typical variations in bolt stress which were obtained during one of the early bolting-up operations are shown in Figure 2.3. The variation in loading may be reduced by changing the amount of pre-stress for successive bolt pairs during a pass. The goal is to achieve a variation of ± 10 per cent of the desired bolt stress in one pass.

Gasket Leakage. A set of two corrugated stainless steel gaskets with a soft-iron core were used throughout the test. Leakage through the inner gasket was 1/4 cc/hr. of water at 1200 psig hydrostatic pressure. This test pressure is double the reactor operating pressure. To test the outer gasket, a pressure line connecting the intra-gasket channel to the inside of the vessel was installed. This subjected the outer gasket to the pressure within the vessel. The vessel was then pressurized in 50-lb increments, and the outer gasket was visually inspected for leakage. The first sign of leakage was observed at 750 psig internal pressure.

2.1.3 VESSEL-TO-SHIELD POOL CONNECTION

Detailed design calculations are being reviewed and prepared for a design report. A slight refinement was made on the reference design, which will make it easier to install and remove the large expansion-joint assembly. Fabrication drawings for the entire connection are being made.

A thermal analyzer program was run on the computer to determine the temperature of the rubber O-ring seals and to determine the thermal gradient in the large expansion joint support ring. Both the thermal stress level resulting from the temperature gradient and the seal temperatures are adequately low.

A new type of metallic insulation for the vessel head is being investigated. A leak detection system that will notify the operator should a leak develop in the vessel-to-shield pool connection was designed.

2.1.4 STEAM DRYERS

The reference design is being modified to include mesh-type steam dryers to remove moisture from steam entering the superheater. The dryers will be located in the neck of the pressure vessel, which is about 4 ft above the water level. Dryers will be located over the core only, and will be inclined 15 degrees with respect to the horizontal to facilitate draining. The mesh will be made of a material such as Inconel, which resists stress corrosion, and will be fabricated so that the wire will not fray.

2.1.4.1 Tests on Separation of Water from Steam. A schematic diagram of the 19-in o.d. test column used for these tests is shown in Figure 2.4. The test column is constructed of steel pipe with welded fittings to accommodate calorimeter taps, sight-glass flanges, and manometer taps. A perforated plate and a fine-mesh screen are supported in the bottom of the test section to distribute the steam bubbles more uniformly across the pipe. Throttling valves are located on either side of the test section to adjust the steam flow and pressure. A heat exchanger is located in a line parallel to the steam supply to permit adjustment of the liquid level in the test column. Further details of this test set-up were reported last quarter.

Natural Separation. Experiments conducted to date show that natural separation will produce steam of 99 per cent quality or better, provided that the release rate is below a critical value.[18] This critical value is a function of system pressure, temperature, height above the interface, and up to a certain size, the diameter of the vessel. Sterman[19] provides an expression for determining the approximate diameter at which entrainment is independent of vessel diameter:

$$\frac{d}{\sqrt{\frac{\sigma}{\gamma - \gamma''}}} \left(\frac{\gamma''}{\gamma - \gamma''}\right)^{0.2} - 260 \qquad (2.1)$$

18. J. Wilson and M. McDermott, "Moisture De-Entrainment Tests in Two- and Four-Inch Diameter Test Sections," Allis-Chalmers Report ACNP-5921, 1959.

19. L. Sterman, "On the Theory of Steam Separation", J. Tech. Physics, (USSR) 28, 7 (1958).

where,

d = vessel diameter
σ = surface tension
γ = specific wt. of liquid
γ'' = specific wt. of vapor

Typical results of an experiment carried out in a 19-in dia. vessel, which by Sterman's criterion is a large vessel, are shown in Figure 2.5. This shows the relationship between quality measured 33 in. above the interface and the steam release rate for different system pressures. The rapid rise in the quality of the steam after "break" point is reached is typical for all test sections. Thus, if the release rate is below the critical value, very little mechanical separation is required. These results confirm results previously obtained in tests with 2- and 4-in dia. test columns.[18]

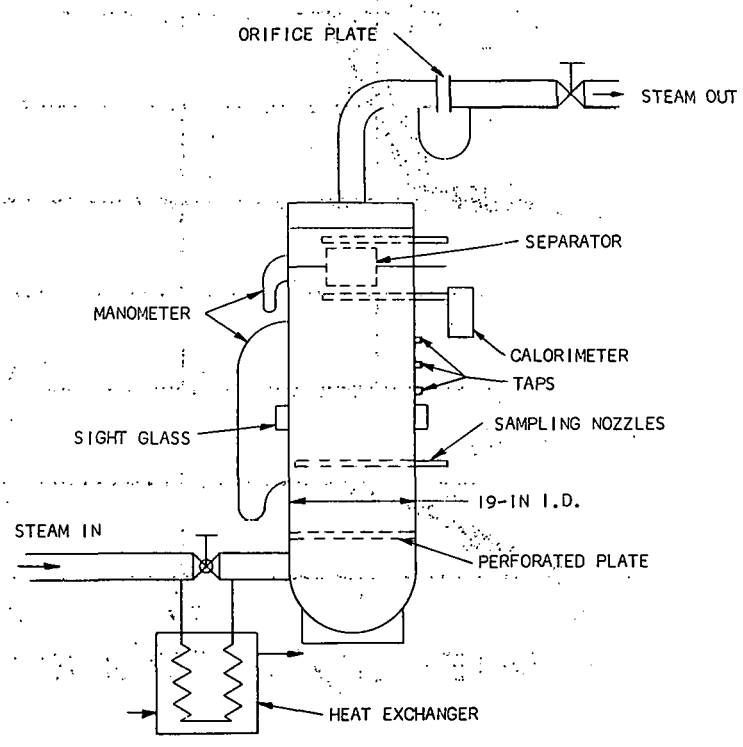

Figure 2.4
Schematic diagram of moisture entrainment test setup.

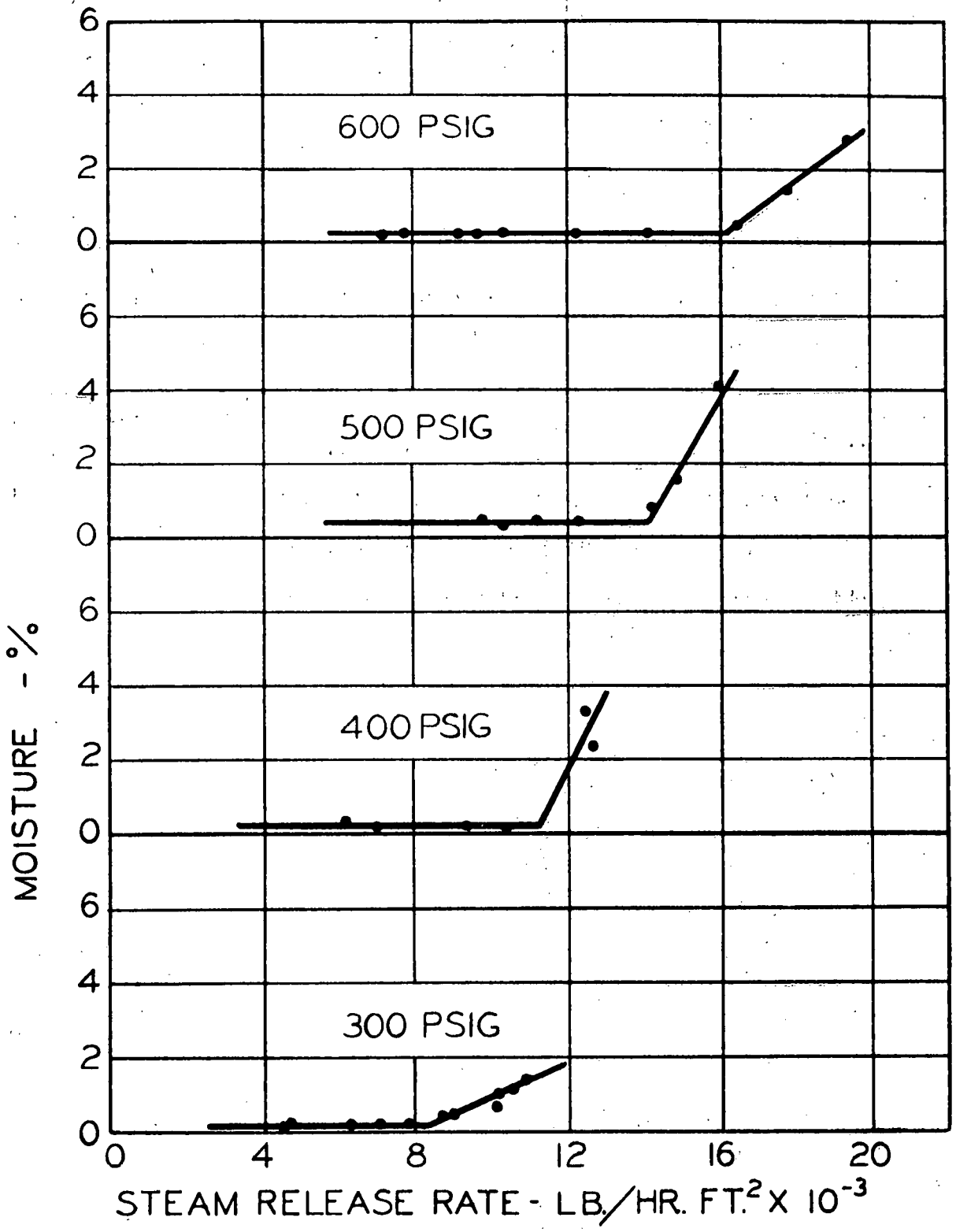

Figure 2.5 Moisture entrained 33 in. above interface in a 19-in diameter test section.

Mechanical Separation: Tests were run on a mesh- and two centrifugal-type dryers. As a result of these tests, it was concluded that the mesh-type dryer is best suited for use in Pathfinder. Parameters considered in making the selection were:

1) separation efficiency, i.e. the outlet quality compared to the inlet quality;
2) separator operating characteristics when overloaded;
3) most efficient use of reactor cross-sectional area;
4) maintenance and cleaning problems; and
5) cost.

Separation Efficiency - Both the centrifugal and mesh-type dryers operate at very near 100 per cent efficiency with the inlet moisture varying from 1/2 to 7 per cent when they are not overloaded. Both produce steam of 99.9 per cent quality at Pathfinder operating conditions.

Overload Characteristics - Tests showed that as the steam flow through the separator is increased, an overload ("break") point is reached. With the mesh-type dryer, this point is characterized by a gradual decrease in outlet steam quality, so that the outlet steam quality approaches the inlet quality. When an overload point is reached with the centrifugal-type dryer, water is sucked up through the drain pipes, which extend below the two-phase interface. This overload condition is very undesirable since additional water is added to the outlet steam.

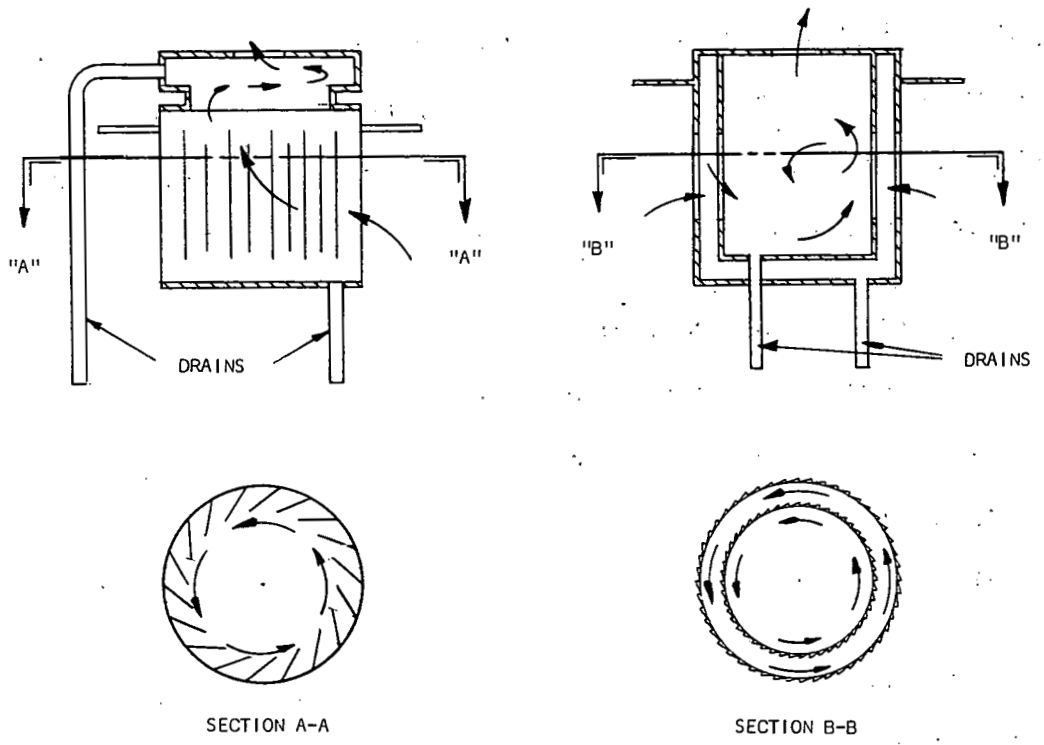

Figure 2.6 Type A (left) and Type B (right) centrifugal steam dryers.

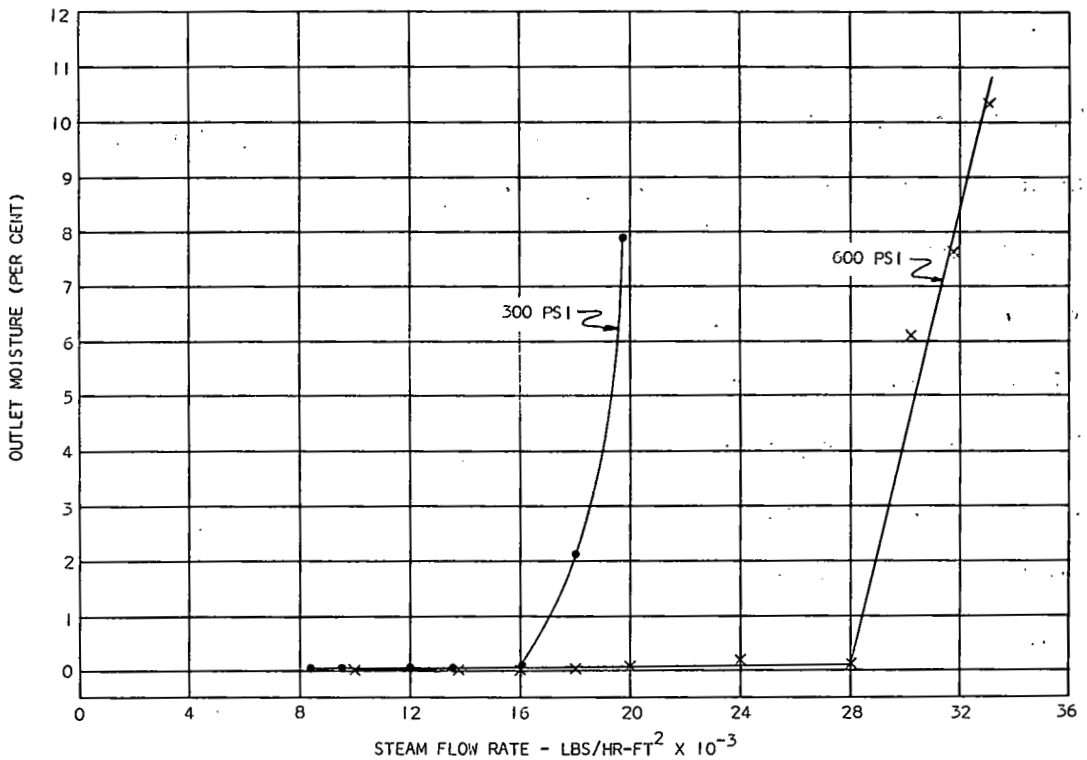

Figure 2.7 Outlet moisture from Type A centrifugal steam dryer.

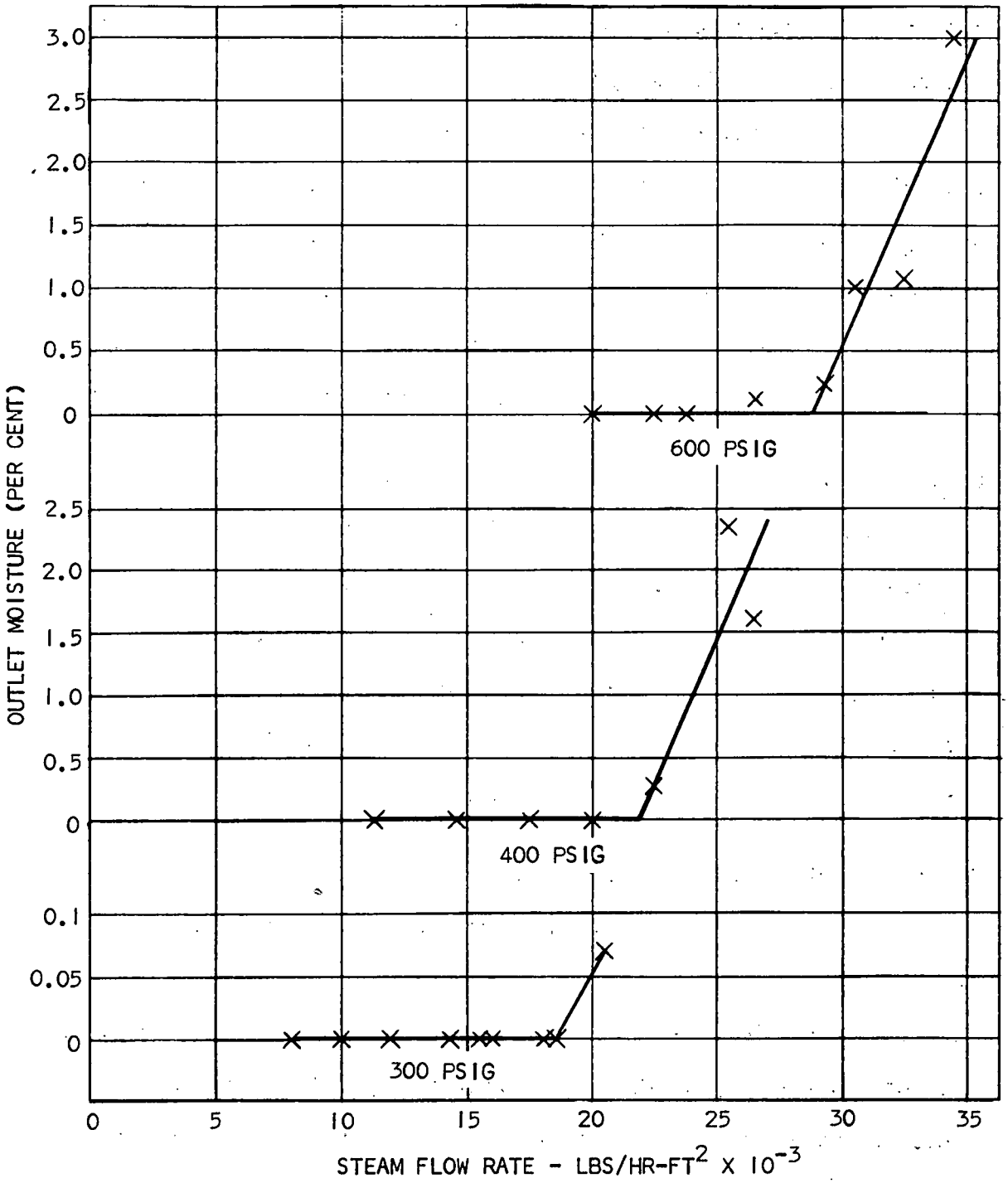

Figure 2.8 Outlet moisture from 6-in thick mesh steam dryer.

The two types of centrifugal dryers tested are shown in Figure 2.6. The results are shown in Figure 2.7 for the Type A dryer. Results obtained with the Type B centrifugal dryer were similar, except that the break point for 600 psig occurred at about 22,000 lb/hr.

The data on mesh-type separators was obtained with a 6-in thick mesh with a density of 5 lb/ft^3. Results of this test are presented in Figure 2.8. Inlet moisture varied from 1/2 to 7 per cent during the test. In all cases below the break point, the outlet steam quality was 99.9 per cent. Note the similarity to the curves obtained for both natural separation and the centrifugal-type dryer.

Efficient Use of Reactor Cross-Sectional Area - In order to establish a basis for comparing efficient use of reactor cross-sectional area, an area requirement was established for each centrifugal dryer. The maximum flow rate before the overload point was reached was divided by the area requirement to determine a permissible unit load factor. For the mesh-type dryer, this factor is 27,500 $lb/hr-ft^2$. For the best centrifugal dryer, the factor is 10,100 $lb/hr-ft^2$.

Cleaning, Maintenance and Cost - Neither the mesh-type nor centrifugal type dryer presents a difficult problem in cleaning or maintenance. The mesh-type will have to be made of a material that resists stress corrosion. Special precautions will have to be made in fabricating the mesh to insure that the wire does not fray. The wire mesh has a cost advantage of approximately 10-to-1 compared to either centrifugal-type dryer.

Conclusion. The reference reactor design is being modified to include mesh in the neck of the vessel above the core only. The separator assembly will be inclined 15 degrees from the horizontal to facilitate draining. This will allow over 4 ft of height between the two-phase interface and the mesh.

Tests on natural separation indicates the permissible steam release, with this much height available for natural separation, is 20,000 lb/hr-ft^2. The actual release rate is only 6,900 lb/hr-ft^2.

The average velocity through the mesh will be approximately 3.8 fps, whereas the tested capacity of the mesh dryer is 5.8 fps.

This design, which is backed up by test results at reactor pressure and temperature, should provide steam to the superheater at 99.9 per cent quality or better.

Future Plans. More mesh-type spearators will be tested to determine the effect of thickness and density of mesh on the operation of the dryer. These tests will be conducted up to the full capabilities of the test loop.

A program to express the operation of the separator in terms of dimensionless constants is underway. With the additional data from future tests, this program can be completed.

Another program to correlate the data on natural separation using the methods of dimensional analysis is underway. This program also uses dimensionless groups, which appear to more closely predict the process of natural and mechanical separation. With these equations, the critical flow rates for any pressure should be predictable.

2.1.5 BOILER CORE STRUCTURE

2.1.5.1 Boiler Core Grid Plate. The boiler core grid plate is being fabricated at West Allis Works of Allis-Chalmers. No difficulties have been encountered in making the necessary welds.

2.1.5.2 Boiler Core Shroud. Fabrication drawings were sent to West Allis Works. Most of the material for fabrication was received.

2.1.5.3 Feedwater Distribution Ring. The reference design of support members was refined to permit easier fitup in the reactor vessel. The ring now will be supported from the vessel by four support members that will be rigidly attached to the ring and bolted to pads welded to the vessel wall. The differential expansion between the carbon steel vessel wall and the stainless steel ring will be accommodated by flexure of the ring.

2.1.5.4 Steam Separator Support Shelf. Fabrication drawings were sent to the West Allis Works. Material was ordered. The final design is shown in Figure 2.9.

2.1.5.5 Upper Baffle and Steam Dryers. This assembly is being redesigned to incorporate the mesh-type steam dryers. The assembly will perform the four following functions:

1) support the upper portion of the superheater manifold;

2) support the steam dryers;

3) direct the steam from the boiler core through the steam dryers and into the superheater; and

4) provide final alignment of the boiler core control rods to facilitate latching.

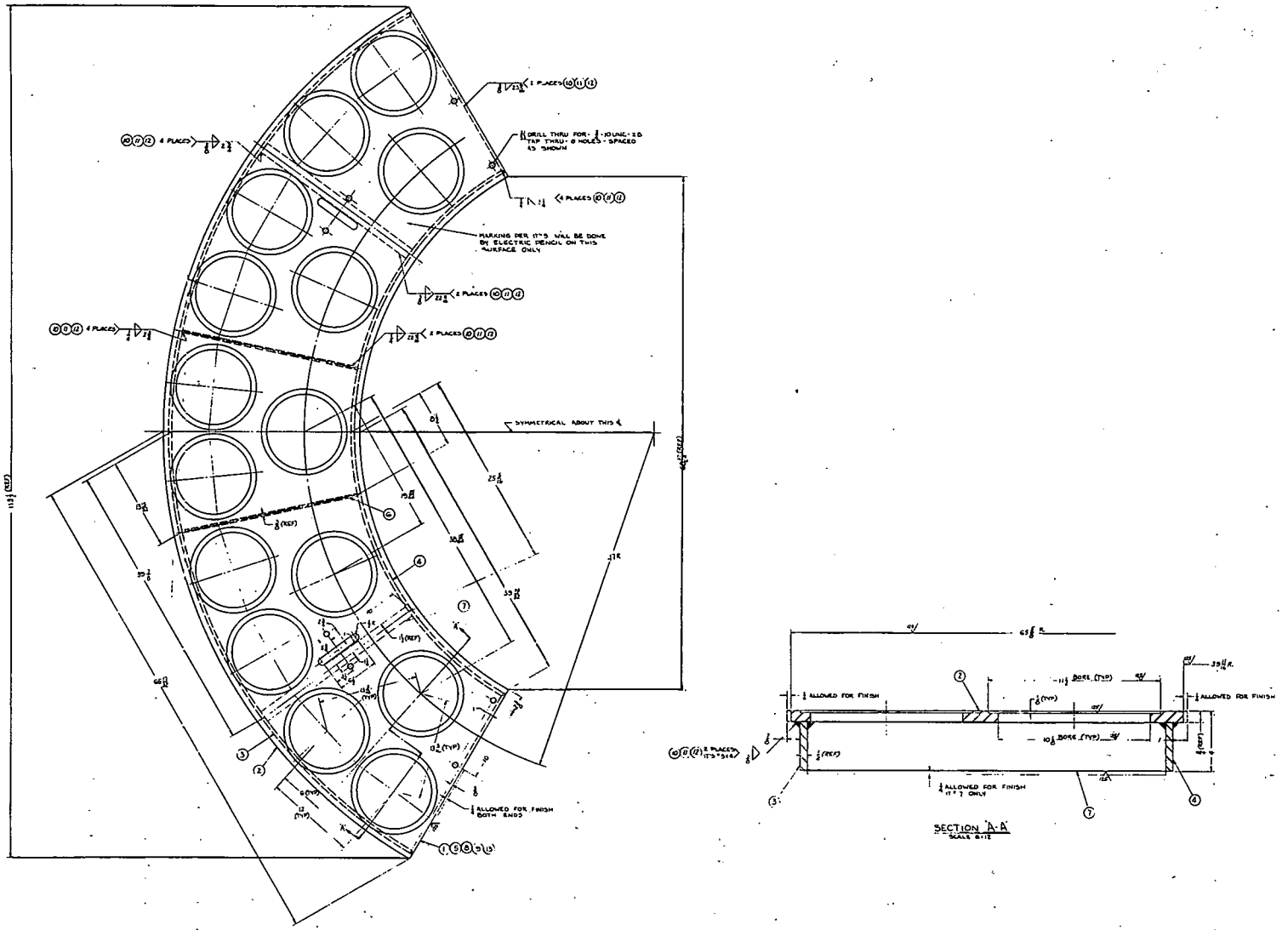

Figure 2.9 Steam separator support shelf.
(A-C Dwg. 43-500-831)

2.1.5.6 Boiler Element Hold-Down Structure. A hold-down structure is needed to overcome the upward hydraulic force across the boiler core and to compress the boiler element springs to hold them rigidly. These two forces total approximately 65 lbs per element. In addition, this structure will support the upper control rod guide tubes and any necessary flow baffles.

Several methods of holding down the elements were investigated. The method selected is a grid which does not locate the element tops; since this requirement is not necessary with the semi-permanent quad-boxes. A layout of the final design will be made during the next quarter.

2.1.6 SUPERHEATER CORE STRUCTURE

2.1.6.1 Superheater Seal Test. The insulating gap between the outer and inner superheater container tubes is sealed at the top grid plate. The outer container tube is fusion welded to the grid plate. An insert which maintains the gap between the inner and outer tubes at the top, is fusion welded to the inner container tube. A seal between the outer tube and insert is accomplished by rolling (expanding) the inner tube and insert into the outer container tube. Tests were conducted to determine whether the rolled joint can be made pressure tight (489 F at 70 psi) and still be readily disassembled.

Sealing austenitic stainless steel tubes in a tube sheet of the same material is difficult since the elastic limit of the tubes is the same as that of the tube sheet. The tubes readily work harden from rolling, and tight joints are not easy to attain even when precise techniques are employed.

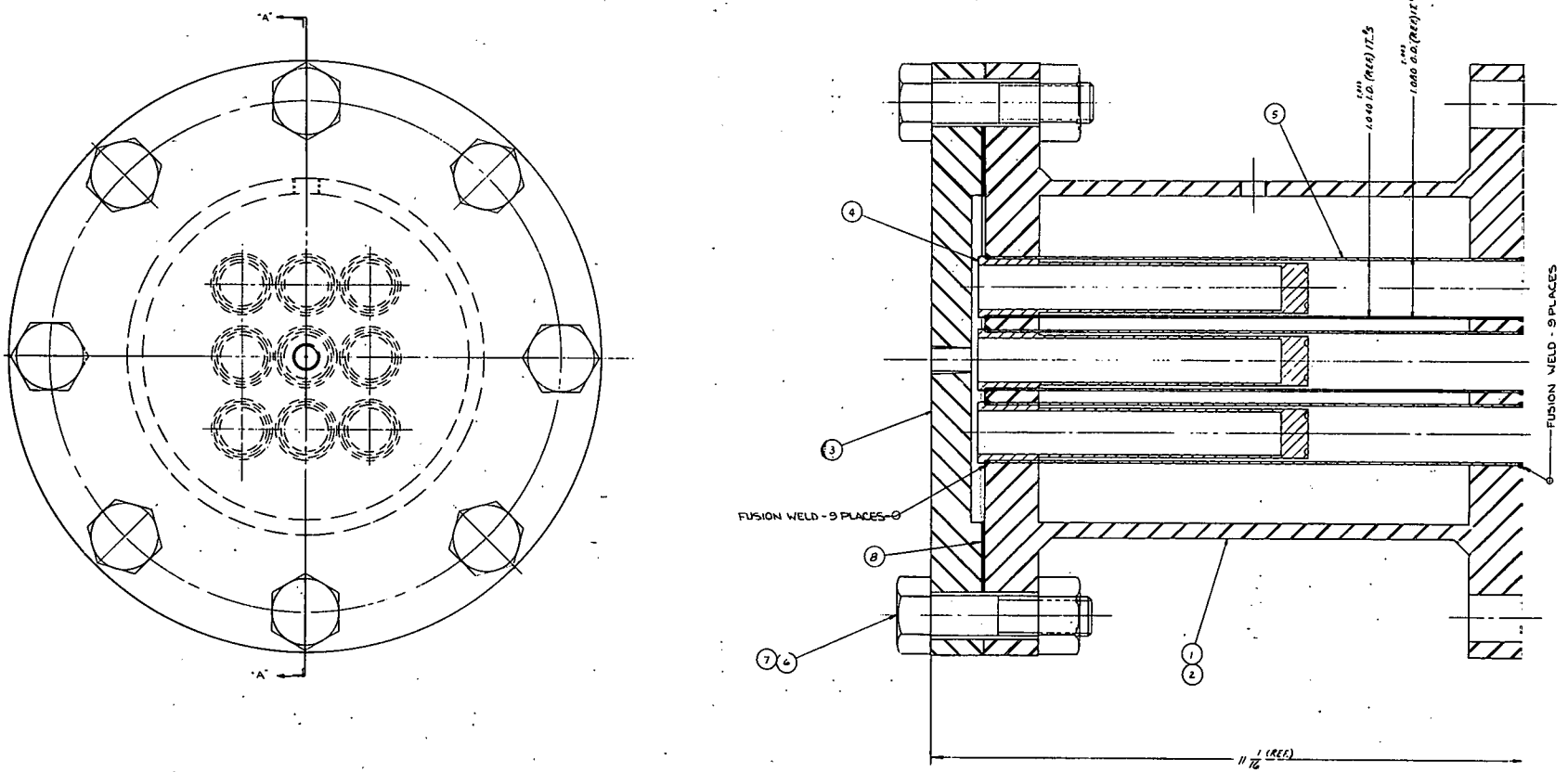

Figure 2.10 Superheater seal test assembly. Code: 2) housing assembly; 3) cover; 4) tube assembly; 5) casing; 8) gasket. (A-C Dwg. 43-401-068)

The test apparatus used in this experiment is shown in Figure 2.10. It consists of a cylinder of 6-in schedule 40 stainless steel welded at both ends to 6-in 150-lb stainless steel flanges; 9 container tubes 1.080 in. o.d. x 0.020 in. thick wall are plugged at one end. The sealing piece is fusion welded to the tubes at the other end.

Test Procedure. The inner tube assemblies were inserted in the outer container tubes and expanded with a conventional condenser tube roller. The torque applied on the tube roller was controlled to produce an optimum radial pressure on the sealing surface in order to insure a pressure-tight seal that could easily be disassembled.

Air pressure at 90 psi was applied on one side of the seal; the seals were tested by immersing the test apparatus in water and checking for bubbles.

In order to simulate thermal cycles encountered in reactor start-up and shutdown operations, the test apparatus was heated to 500 F and cooled at room temperature several times. After each thermal cycle leakage through the seals were checked as described above.

The integrity of the seals under hot conditions was also investigated. The test apparatus was heated to 500 F. The leakage through the seals was checked by immersing the test apparatus in oil at the same temperature and applying air pressure at 90 psi on one side of each seal.

Results. A torque of about 150 in-lb on a conventional tube roller produced pressure-tight seals. Adequate sealing was retained under simulated Pathfinder operating conditions. The optimum torque required for a given configuration depends on the amount of expansion required, the modulus of elasticity, and the moment of inertia of the sealing piece and the inner tube.

Nine seals had the following average dimensions after testing:

Outer tube - i.d. = 1.044 in.

Insert - o.d. = 1.041, i.d. = 0.928

Inner tube - o.d. = 0.926 in. i.d. = 0.886 in.

The average expansion of the sealing piece outside diameter was 0.006 in. All seals were readily disassembled using a conventional condenser tube puller.

2.2 RECIRCULATION SYSTEM

The objectives of this project are as follows: 1) to develop reliable, efficient recirculation pumps that will require a minimum of maintenance; and 2) to develop an efficient shaft seal.

The prototype recirculation pump and motor were completely assembled in July. Initial cold tests were conducted to determine pump head capacity characteristics. The developed head at rated flow of 20,000 gpm was 63 ft including the drop through the suction elbow. The safe NPSH at rated flow was 24 ft. Available NPSH in the reactor at operating conditions is 54 ft. Because of the pressure and temperature difference between the cold test and actual pump operating conditions, the head capacity test will be repeated during hot tests.

The pump was set up in the hot test loop, (Figure 2.11) and hot tests were started in September. This test will include a 200-hr proof test with 5 temperature cycles between 200 and 486 F. The pump will be run 48 hrs at design operating conditions. The hot loop test also provides a thorough proof of the floating-ring shaft seal.

The prototype pump trunnion mounting was fabricated and attached to the pump. When the hot loop test is completed the pump will be mounted solely on the trunnions, and one end of the test loop will be rigidly anchored to simulate reactor piping conditions. Temperature in the loop will be cycled as in hot tests.

The specific purposes of the test are as follows:

1) to observe the functioning of the pump supports under actual operating conditions;

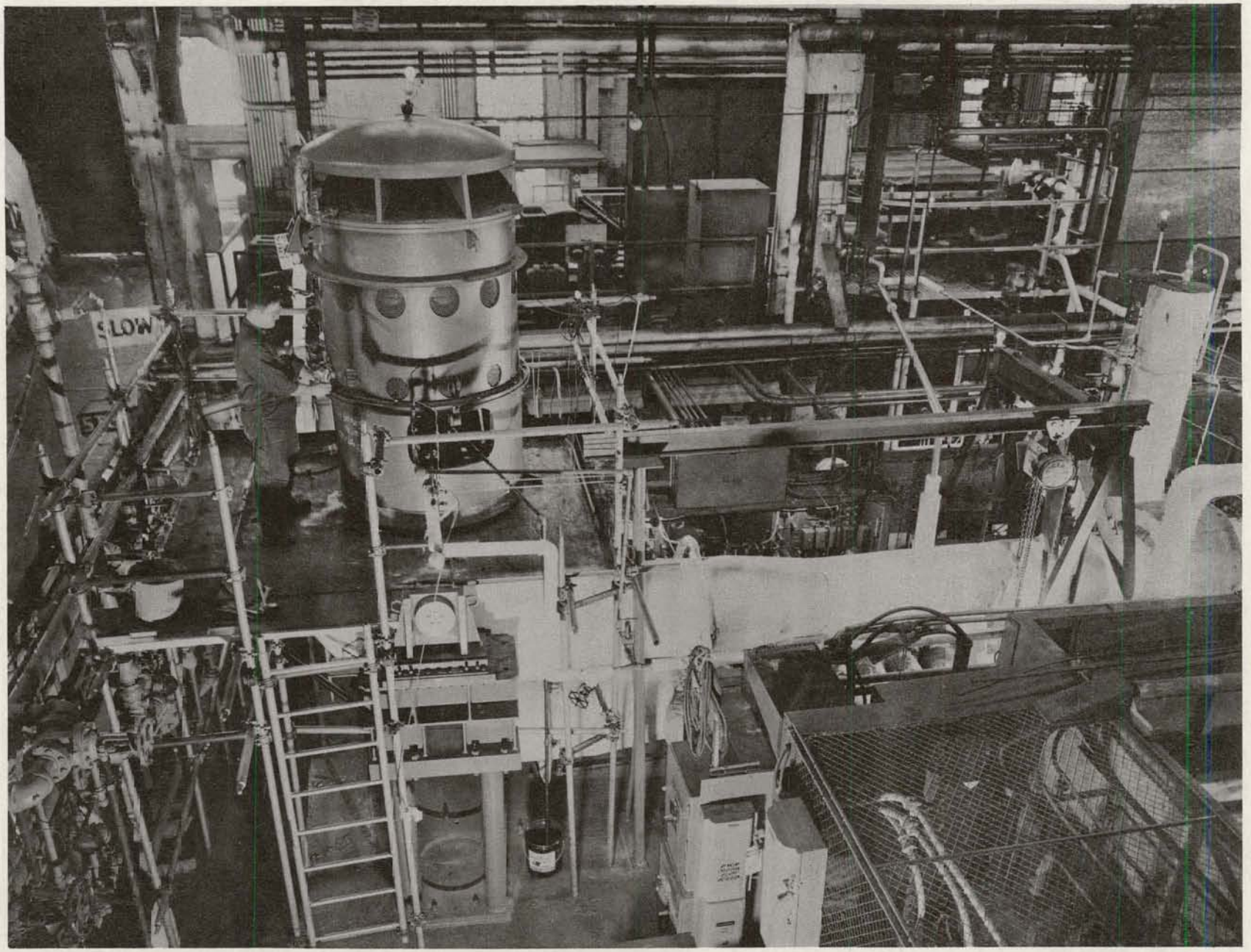

Figure 2.11 Prototype recirculation pump being testec in the hot test loop at reactor conditions. (A-C Photo 211586)

2) to measure the thermal expansion of the pump and piping loop. This would be done to determine whether residual stresses due to welding, fabrication and erection of the loop piping would affect the path of movement of the pump supports;

3) to determine the temperature at various locations in the pump support assembly, especially at the lubrite washer, bushing, and expansion plate;

4) to determine the coefficient of friction of lubrite expansion plate under actual operating conditions;

5) to measure the natural frequencies and amplitude of vibration of the test loop piping when a) the pump supports are externally restrained against lateral motion, and b) the pump supports are restrained only by frictional resistance in the lateral direction.

2.3 CONTROL RODS, GUIDE TUBES, AND CONTROL ROD DRIVES.

The objective of this project is to perform investigations and experimental work in regard to the control rods, control rod guide tubes, and control rod drives leading to fabrication of effective and economical components for the Pathfinder reactor.

2.3.1 CONTROL RODS

2.3.1.1 Superheater Control Rods. Parts for the superheater control rod test described in the last quarterly progress report were fabricated, and assembly is nearly complete.

Detailed design of the control rod has been initiated. Cooling requirements, fabrication, and assembly problems are being considered. Preliminary analysis of coolant requirements for the superheater control rods is being made by calculating control rod temperatures using coolant flow rates of 100 and 125 lb/hr-element.

2.3.1.2 Boiler Control Rods. The boiler control rod was checked for thermal distortion and thermal and impact stresses using various published correlations. In all cases, the rod design proved to be conservative.

Cooling Requirements. The circuit followed by control rod coolant water is up through the control rod coolant inlet sleeve, out into the quad-box bottom plate plenum, through the holes in the bottom plate, through holes in the control rod stub out into the control rod channel, past the inserted control rod, and finally out through slots in the quad-box inner walls. The flow to each control rod is

metered by the size of the holes in the stub, which offer approximately 75 per cent of the total flow resistance.

The criterion used to establish the required coolant flow was that the exit quality from the control rod channel not exceed the average quality of the entire boiler. The maximum average heat generation rate in a boiler control rod will not exceed 3.0×10^6 Btu/hr-ft^3, which results in a minimum required flow of 25,700 lb/hr per rod. The nominal control rod coolant flow has, therefore, been set at 2.5 per cent of the total recirculation flow (24×10^6 lb/hr) or 37,600 lb/hr to each of the 16 boiler control rods.

The maximum heat flux on the control rod surface is 94,600 Btu/hr-ft^2, assuming heat flow out one side only, which is less than the average boiler heat flux; so the mode of heat transfer will always be nucleate boiling. The maximum control rod temperature is 668 F, again with heat flow out one side only; and this temperature is acceptable for the boron-stainless steel material.

Preliminary calculations have indicated that 25 holes in each control rod stub, 0.25 i.d. will deliver the required flow with the rod inserted. If a rod is fully withdrawn, the flow would increase by only about 20 to 25 per cent. The actual hole size will be established following a special hydraulic test of a control rod coolant circuit.

Additional analyses were performed to establish the effect of the control rod coolant flow on the time-displacement of the rod during scram. The analyses treats the rod only to the time it is arrested

by the dash pot. The calculated control rod velocities with and without net coolant flow are shown in Figure 2.12. The coolant flow is calculated to reduce the velocity at which the rod is moving as it hits the dashpot by about 8 per cent.

Boiler Control Rod Stub Test. A special test section was designed in order to experimentally determine the required hole size in the control rod stub and to study the effect of rod position on the coolant flow. The test section is an exact mock-up of the inlet sleeve, quad-box bottom plate, stub, and a short section of a control rod and control rod channel. Three stubs each containing 25 holes of 0.20, 0.25, and 0.3 in. i.d. respectively, will be tested; and the pressure-drop–flow relationships will be determined. The position of the control rod in the control rod channel will be varied and the effect on pressure drop determined. The required hole size will be established by comparing the flow–pressure-drop relations for the three hole sizes with the available pressure drops (calculated) in the core.

2.3.2 CONTROL ROD DRIVES

2.3.2.1 Prototype Control Rod Drive. An oil accumulator was designed and built from Plexiglas to pressurize the motor housing. A pressure of 10 psig is applied using nitrogen, and any drop in oil level can be seen through the plastic housing.

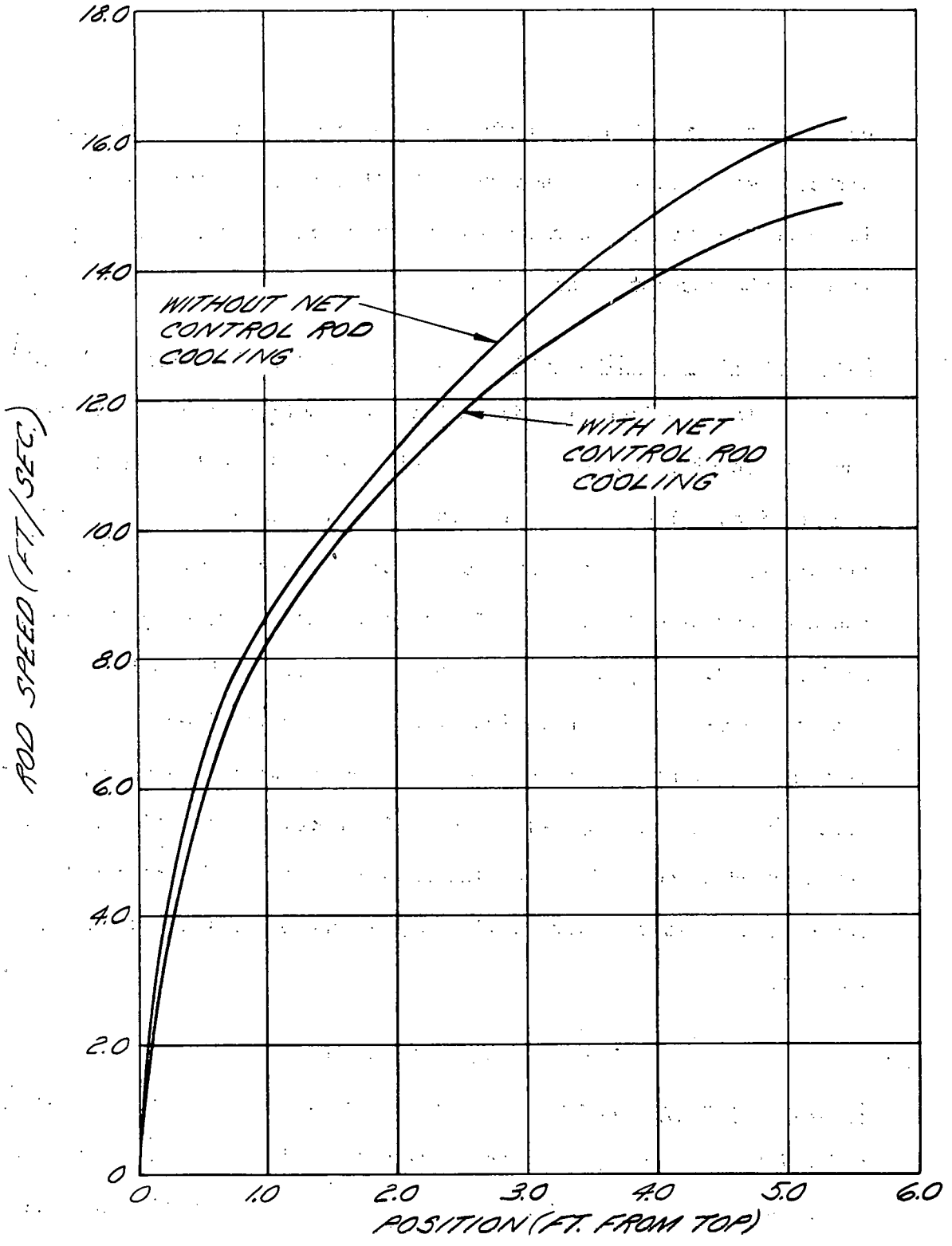

Figure 2.12 Comparison of boiler control rod displacement with and without net coolant flow.
(A-C Dwg. 43-024-339)

Preliminary Testing. The drive was placed in a stand and the accuracy of the synchro-driven position indicating system was checked. The accuracy was within 3/8 in, usually within 1/4-in, with one position receiver. With two position receivers, the accuracy was reduced to 1/2 in and the pointer movement was erratic. A one-receiver system was therefore chosen for the hot tests.

Cold Tests. The drive was bolted into place on the hot test pressure vessel, and the entire assembly was hydrostatic tested at 700 psi. The leakage through the rotary shaft was 12 cc/hr.

When the drive was scrammed with a solid water system with no scram accumulator, the scram time was 3.5 sec. Scram time is reduced to 1.5 sec. by adding the scram accumulator.

During these tests, the 3-3/4-in magnetic clutch began slipping, and was replaced by a 4-1/2-in clutch.

The limit switches and position indicator dial readings became erratic during tests. It was found that a roll pin holding one of the gears had failed. This pin was replaced by a solid pin.

Latching and unlatching were performed many times. The rack was locked in the up position several times. The drive performed these functions very well. When the control rod is latched or unlatched, a definite difference in drive motor current readings can be observed.

Hot Tests. The test was brought up to 489 F, 600 psig. The drive ran very well. The speed was 62 in/min in the up direction and 75 in/min in the down direction.

The time required to bring the test set-up up to temperature and pressure had been excessive, apparently because of excessive heat loss to the simulated shield pool water. This was apparently due to a leak in the steam supply tube for the scram accumulator, since convection currents were noticeable in the region where this tube entered the pinion housing.

When the drive was scrammed, the control rod dropped for about 36 inches and slowly coasted the rest of the stroke. This was also probably due to the leaking steam supply tube. Without the accumulator, the drive will only scram for about 10 in. before slowing down. The scram times were about 5 sec.

Leakage through the high-pressure rotary shaft seal between the pinion housing and rack housing increased to 300 cc/hr. Sodium sulfite rust inhibitor in the pressure vessel began to break down, releasing H_2S and SO_2. The test was shutdown to replace the sulfite rust inhibitor with phosphate rust inhibitors. The set-up will be cycled several more times, before repairing the steam supply tube.

3. NUCLEAR ANALYSIS

THIS PAGE

WAS INTENTIONALLY

LEFT BLANK

3.1 REACTOR PHYSICS (STATICS)

The objectives of this project are as follows: 1) to evaluate the characteristics of the reference core and optimize the design to achieve safe, reliable, and economical performance; and 2) to optimize shielding designs so as to arrive at an adequate and economical design.

3.1.1 ANALYSIS OF CONTROL ROD WORTH

Theoretical analysis of the worth of boron stainless steel control rods in several reactor configurations is in progress. Fast- and thermal-group equivalent diffusion-theory constants were computed for the control rod using the α,β technique described in WAPD-218. This technique assumed diffusion theory outside the rod and blackness theory within. The problem is assumed to be one-dimensional, which is a very good approximation for rods with a 5-in. span. The blackness-theory-corrected material absorption of the rod is then averaged over a flux spectrum characteristic of the reactor. The results provide effective diffusion-theory group constants for the rod, so that when these constants are used in a diffusion theory code, such as PDQ, the same values of K_{eff} are yielded as would be yielded by the actual physical constants of the rod used in a transport theory solution.

Table 3.1 lists a typical set of fast and thermal rod constants for control rods of 2 w/o natural boron stainless steel. Both physical constants and effective diffusion theory constants are listed. The physical constants were obtained by averaging the material cross sections over MUFT and SOFOCATE spectra. The effective constants were also corrected for no mesh points within the rod.

TABLE 3.1 BORON STAINLESS STEEL CONTROL ROD CONSTANTS

	Physical	Effective Diffusion Theory
D_1	0.281	0.969
a1	0.811	0.0676
D_2	0.0568	0.0351
a2	4.94	1.41

These constants were used to calculate two core configurations measured in the critical facility. Using PDQ, the core cross section was described in two-dimensions with control rod water channels as well as the control rods represented explicitly. The cross sections for the fueled regions of the core were obtained using the methods previously described in this report.

The first configuration examined was the 1.8 per cent enriched slab described in ACNP 6006, Section 3.3.6, in which one rod was fully inserted. For this configuration, several control rod representations were examined to develop confidence in the model. Using the constants tabulated in Table 3.1, the rod worth was computed to be 3.4 per cent Δk, in exact agreement with the measured value of 3.4 per cent in Δk.

The second configuration examined was the full core mockup with the superheater voided and 1.89 per cent enriched boiler fuel in the lower and upper lattices of 81 and 64 pins, respectively.

Both the lower and upper regions were represented in detailed X-Y geometry with all control rods either full in or full out. For these X-Y problems, the axial bucklings were obtained from the results of an R-Z calculation. The calculated values for the control rod worth were 13.9 per cent and 13.4 per cent in Δk for the lower

and upper regions, respectively. These values agree well with the measured value of 13.6 per cent.

Currently the same techniques are being used to calculate the control rod worth in Pathfinder.

3.1.2 NUCLEAR CONSTANTS FOR PATHFINDER

Prior to specifying the first core properties of Pathfinder, a completely new set of nuclear constants is being developed. The constants are being obtained at both cold and at operating temperatures. The hot data are also being computed for void fractions up to 50 per cent.

The method used is as follows: 1) The fast group constants are computed by first volume weighting together the materials within a given region of the reactor, such as the lower boiler fuel box. With these homogenized inventories, nuclear constants for the region are obtained using MUFT IV and assuming experimentally measured P_{Fe}^{28} and Doppler broadening data. The axial water gaps were flux weighted into the fueled regions by using results from one-dimensional diffusion theory (WANDA) calculations of the neutron flux along a representative axial traverse. 2) Because of the shorter diffusion length of thermal neutrons greater attention is given to geometric detail in obtaining thermal nuclear constants. The first step is to obtain an

initial thermal spectrum using the SOFOCATE code with the volume weighted inventories for given regions of the core. This initial thermal spectrum is used for transport-theory cell calculations using the P-3 code over the fuel pin, clad, and immediately adjacent water. The results of the P-3 calculations provide flux-weighted constants for the material interior to the zirconium fuel boxes. The zirconium boxes and associated inter-box water channels are flux weighted into the fueled region using results from two-dimensional PDQ cell calculations. Both the pin and box flux weighting factors are then used to provide effective inventories for a final SOFOCATE.

Table 3.2 presents a summary of nuclear data thusly computed for the lower and upper boiler fuel regions at cold and hot operating (no voids) conditions.

TABLE 3.2 BOILER LATTICE CONSTANTS (2.2 PER CENT ENRICHMENT)

	Lower Lattice (Water-to-Fuel = 2.056)		Upper Lattice (Water-to-fuel = 2.931)	
Parameter	cold	operating	cold	operating
k_∞	1.319	1.278	1.308	1.296
ηf_1	.163	.191	.122	.146
p	.7621	.7032	.8188	.7732
ηf_2	1.517	1.546	1.449	1.487
τ	40.67	55.17	38.33	53.42
L^2	2.98	5.76	3.09	6.24

3.1.3 LOCAL FLUX PEAKING

Additional calculations on the reduction of power peaks caused by non-fueled axial regions within the boiler core were performed. Buffer pellets, 1/2 in. long with fuel enrichments ranging from natural to the reference core enrichment and containing a burnable poison, were located adjacent to the non-fueled regions. To prevent a large mis-match between fuel and poison depletion and consequent increase in power peaking with core burnup, dysprosium was selected as the burnable poison. Eighty-three per cent of the effective poison cross section of dysprosium is due to the isotope Dy-164 which has a 2800-b cross section at 2200 m/sec. The poison depletion is therefore due mainly to the burnup of this isotope. The effect of irradiation on the peaking factor was analyzed in the same manner as outlined in ACNP 6007.

The effects of burnup for several cases are shown in Table 3.3. All three cases have the same amount of dysprosium oxide within the 1/2-in. long buffer pellet. The only variation between the cases is the enrichment of the fuel in that pellet. The amount of poison used is compatible with the burnable poison requirements for the boiler core. The residual poison at one year for these cases is approximately 20 per cent.

It can be seen that with no reduction of enrichment in the buffer zone, the maximum power peaking is in the buffer. For an enrichment of 1.55 per cent, it is in the adjacent fuel. With an enrichment of 1.8 per cent, the two factors become about equal and minimum. It should be kept in mind that these factors are superimposed on the

TABLE 3.3 POWER PEAKING AT AXIAL GAPS

Reactor Operating Time (mo.) (Full Power)	2.2 Per Cent Enr.* Peaking Factor 1**	Peaking Factor 2**	1.85 Per Cent Enr. Peaking Factor 1	Peaking Factor 2	1.55 Per Cent Enr. Peaking Factor 1	Peaking Factor 2
0	1.270	1.068	1.117	1.090	0.957	1.115
2	1.385	1.165	1.240	1.184	1.072	1.215
4	1.448	1.230	1.284	1.250	1.153	1.269
8	1.470	1.288	1.307	1.303	1.221	1.328
12	1.440	1.292	1.284	1.304	1.212	1.321

* Fuel enrichment in buffer pellet. 2.2 per cent is reference enrichment for core.

** Peaking Factor 1 = ratio of maximum power in buffer pellet to average power in fuel.
Peaking Factor 2 = ratio of maximum power in fuel to average power in fuel.

normal axial flux distribution but the peak of this distribution would not normally occur at the gap location. Also, there is some decrease in other hot-spot factors before the time this gap peaking reaches a maximum.

3.1.4 CORE BURNOUT

The superheater power fraction was calculated as a function of the superheater fuel loading and burnable poison content. These calculations are extended over the core life. The results are shown in Figure 3.1. The three curves in the figures represent different concentrations of burnable poison within the superheater. For all three curves, the boiler core had the reference enrichment with a fixed burnable poison loading.

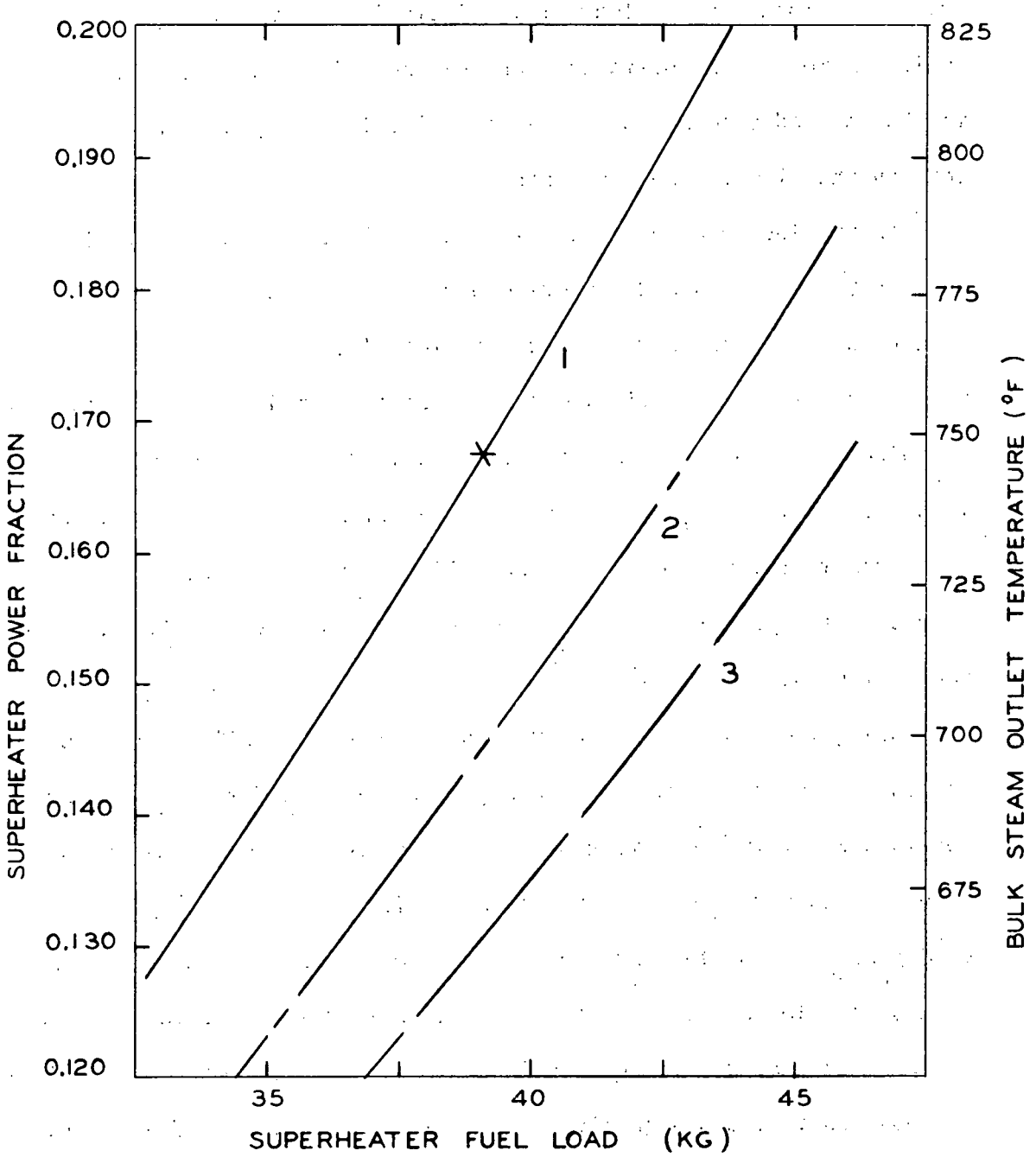

Figure 3.1 Superheater power fraction for various fuel and burnable poison loadings. Curves 1, 2 and 3 represent different burnable poison loadings in the superheater

It can be seen that there are many combinations of superheater fuel and poison loading that will satisfy the initial design requirements. However, the different burnout characteristics between the boiler and superheater cores determine the acceptable range to satisfy the lifetime requirements.

In the last quarterly report, ACNP 6007, the flux distribution in an X-Y plane with and without control rod insertion was given. With no superheater control rods inserted, the flux distribution in the superheater is relatively flat. Because of this, it would be advantageous to operate the reactor with little or no control rod insertion in this region. To do this, however, the mis-match between the burnout of the superheater and boiler core must be minimized. Because the superheater core is highly enriched, most of the burnable poison must be located here.

Using the Candle II burnout program, operation with no control rod insertion in the superheater region was analyzed for Pathfinder. For this analysis the option of a poison search for criticality was used with only the boiler core as the uniform control region. Results in Figure 3.2 show the integral superheater power fraction as a function of reactor operation. It can be seen that there is very little change in power fraction during the first nine months operation. This corresponds to the design lifetime for the superheater. The initial conditions for this superheater core correspond to those marked with an X in Figure 3.1.

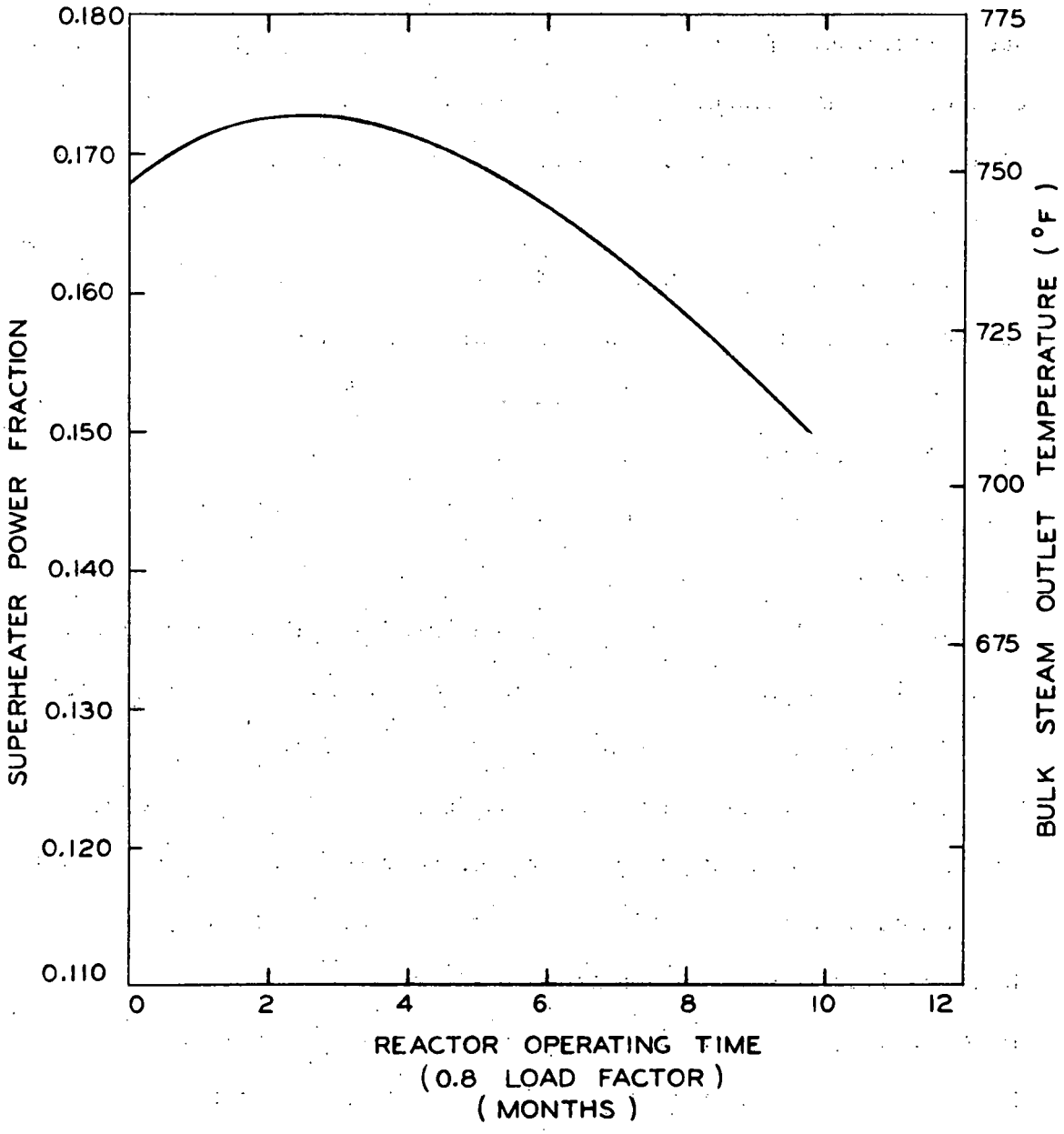

Figure 3.2 Superheater power fraction as a function of reactor operation.

3.1.5 SHIELDING

The dose from the fuel storage pool pre-filters and demineralizers was calculated. The dose could be near zero or as high as 2 R/hr. depending on the amount of crud collected on them. Sufficient room will be left around these items so that shielding can be added later if it is needed.

The dose levels at the fuel transfer carriage access manholes was calculated assuming a spent element in the transfer tube. The dose at the 4x7-ft equipment manhole is 1×10^4 R/hr without shielding. After the equipment is in place, a concrete slab will be placed near the bottom of the manhole and covered with earth fill. This will reduce the above dose to a tolerable level.

The dose at the top of the manhole used to gain access to the equipment is 500 R/hr. This dose will be reduced by a 2-ft concrete manhole cover, or by a slab shield over the transfer tube itself. With the shielding in place, the dose on top of the manhole cover is 5 R/hr, or 80 mr assuming a 1-min transit time for the spent fuel.

Calculations show that due to streaming of gamma rays, four ventilation-duct penetrations will require shielding. The penetrations will be shielded by shadow shields placed under the plug floor covering the penetration. The dose at the penetration near the periphery of the biological shield is 1 R/hr. A 2-ft concrete shadow shield under this penetration will reduce the dose to normal levels on the plug floor. The dose at the other three penetrations near the periphery of the reactor building is 130 mr/hr. Twelve-inch concrete

shadow shields under these penetrations will reduce the dose to normal levels on the plug floor.

Gamma and neutron streaming down the instrument tubes in the biological shielding result in a dose of 8 R/hr at the end of the tubes. Thirty-six inches of concrete is needed to reduce this dose to 2 mr/hr.

A final shielding report to include all dose calculations for Pathfinder is being compiled.

3.2 REACTOR AND SYSTEM DYNAMICS ANALYSIS

The objectives of this project are as follows: 1) to determine analytically the dynamic behavior of the reactor and related systems under normal and abnormal conditions, and 2) to determine the effectiveness of the reactor control systems and the nuclear instrumentation requirements.

3.2.1 SIMULATION OF PRESSURE CONTROL SYSTEM

The pressure control system described in the previous quarterly report (ACNP-6007) was simulated in detail on the Pathfinder Transient Simulator. The voltage levels, amplifier gains, proportional-plus-reset controller and bias voltages correspond exactly to the actual control system. The electrical, pneumatic, and mechanical components were simulated using the best information available. Rate limiters and function generators were used to simulate the turbine inlet valves, regulating dump valve, and the turbine stop valve. The computer can thus simulate turbine trip and turbine overspeed as well as normal operation of the plant.

3.2.2 SIMULATION OF TEMPERATURE CONTROL

A limited amount of experimenting with superheater temperature control was done during the quarter. As was anticipated, some degree of temperature control greatly reduces operational transients, especially the superheater hot-spot temperature. Since superheater temperatures are directly related to the reactor power-to-flow ratio, the temperature control system increases the response of steam flow to reactor power. With the method tried, the superheater steam outlet

temperature signal (T_2) is sent through a proportional-plus-rate amplifier, This output signal is then added to the existing steam line pressure signal (P_2), and the sum is fed to the existing control system. Thus, this simple T_2 control system sends an additional control signal to the turbine inlet valves. More experimenting with T_2 control will be done during the next quarter, and its necessity and practicality will be determined.

3.2.2 SIMULATION AND SELECTION OF REGULATING DUMP VALVE

Extensive testing was done to determine the best flow characteristics for the regulating dump valve. A linear valve was selected and its results were compared with those of a standard equal-percentage valve for the two cases of turbine trip (turbine stop valves close in 0.35 sec) and turbine runback (turbine inlet valves close in 0.6 sec.). These transients should impose the most demanding operation on the dump valve. Computer results are shown for both the linear and equal-percentage dump valve operating during turbine runback and turbine trip with the turbine initially at full capacity. Turbine runback with an equal percentage valve is shown in Figure 3.3 with a P_2 rise of about 30 psi. Figure 3.4 shows that a turbine runback with a linear dump valve causes a P_2 rise of about 15 psi. Turbine tripout with an equal percentage valve is shown in Figure 3.5 causing a 35-psi drop in P_2. Figure 3.6 shows that a turbine trip with a linear dump valve causes a 55 psi drop in P_2.

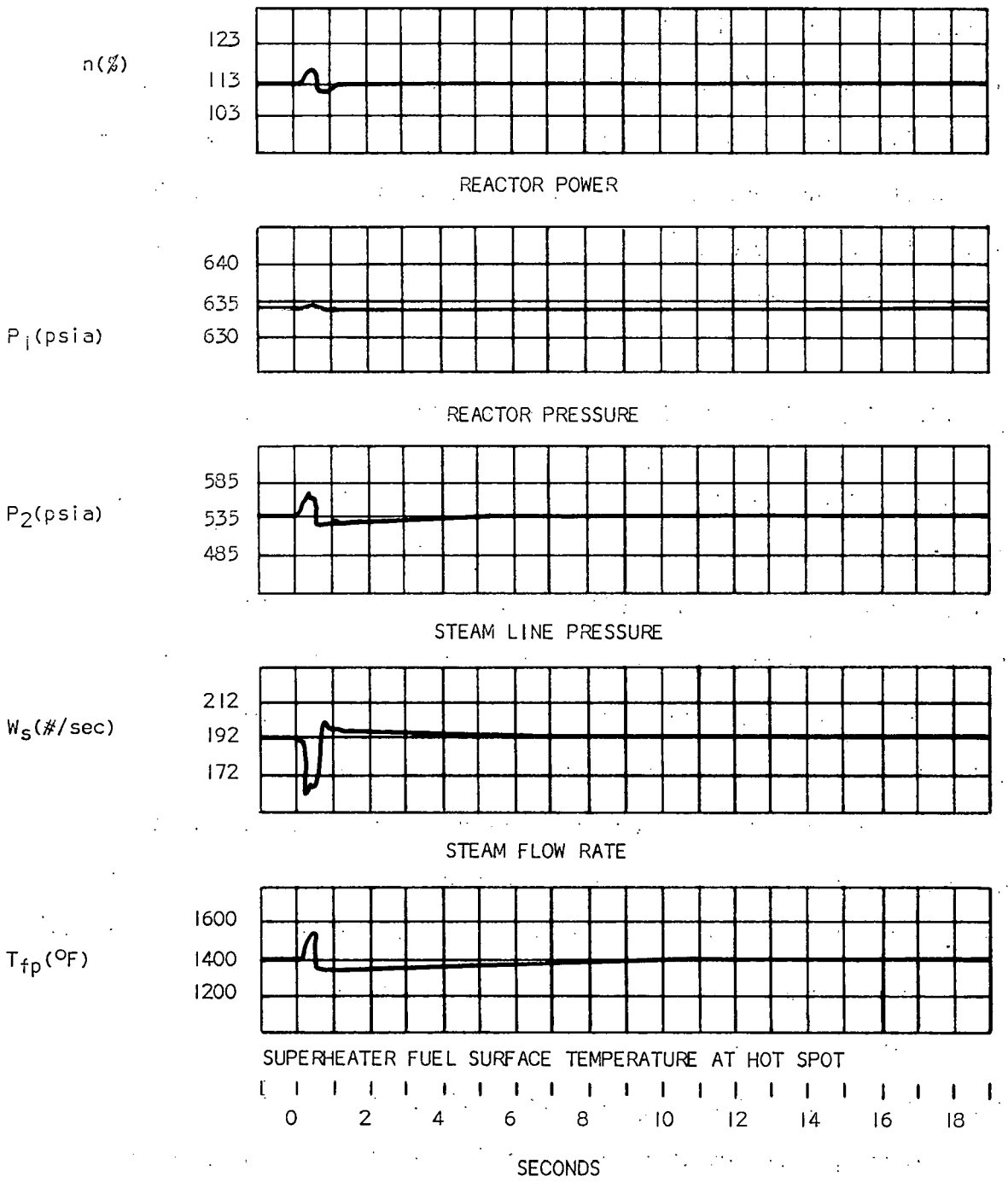

Figure 3.3 Turbine runback when inlet valve is wide open and closes in 0.6 sec. - automatic actuation of by-pass valve (equal percentage). (A-C Dwg. 43-024-305).

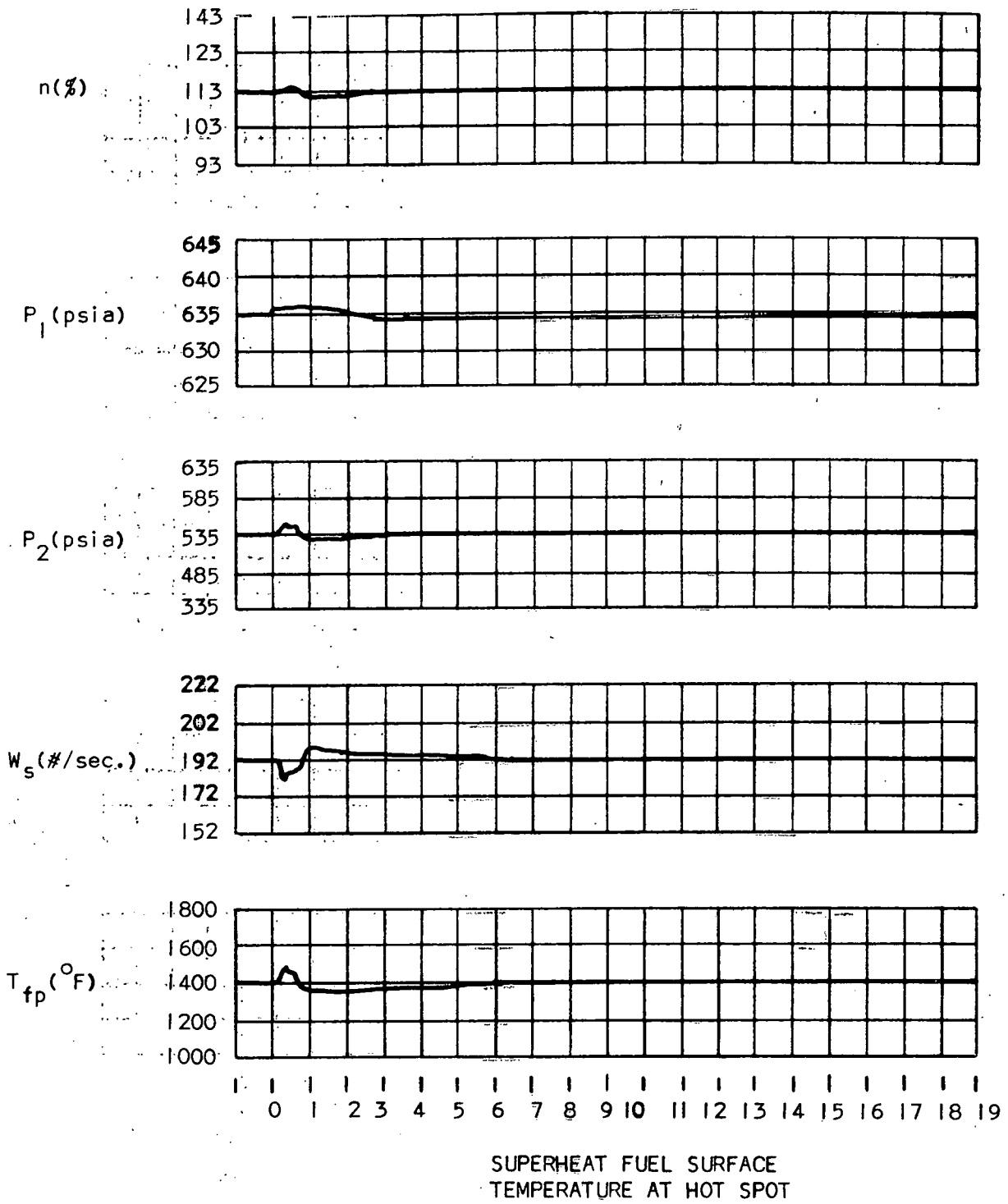

Figure 3.4 Turbine runback when inlet valve is wide open and closes if 0.6 sec.- automatic actuation of by-pass valve (linear). (A-C Dwg. 43-024-300).

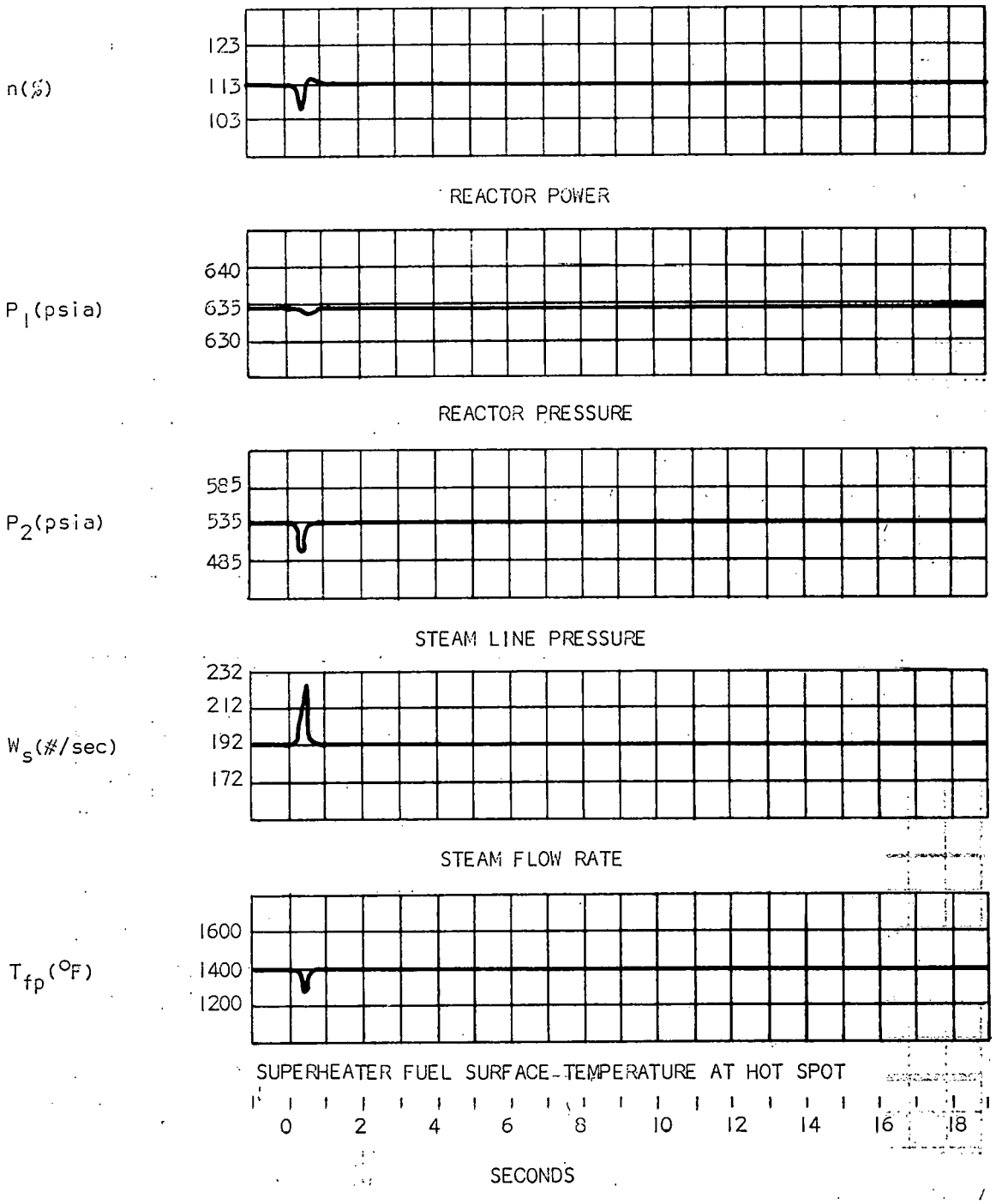

Figure 3.5 Turbine trip when inlet valves are wide open - automatic actuation of bypass valve (equal percentage). (A-C Dwg. 43-024-303)

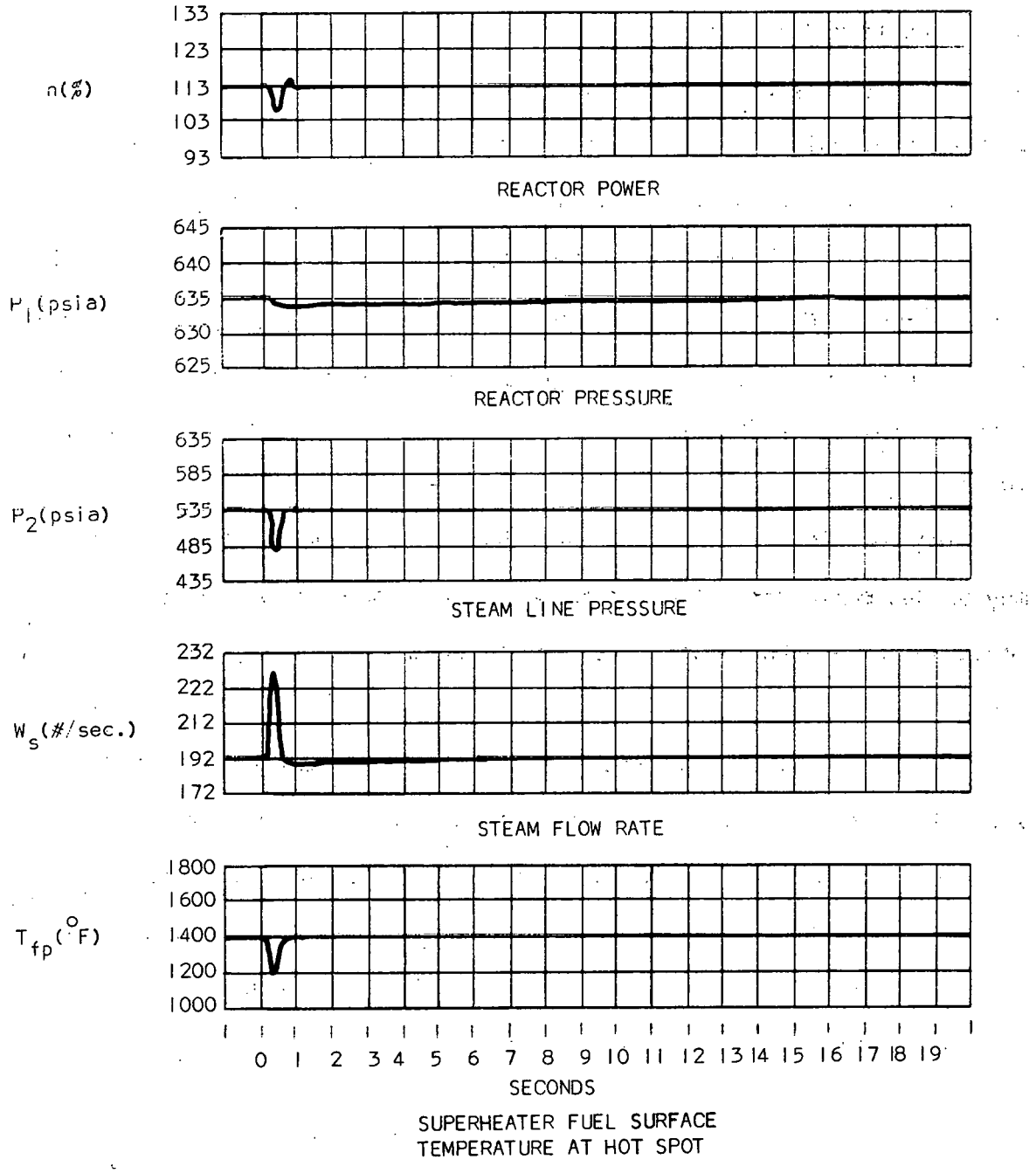

Figure 3.6 Turbine trip when inlet valves are wide open - automatic actuation of bypass valve. (A-C Dwg. 43-024-299).

Some general comments can be made as a consequence of these results:

1) A pressure drop will always occur in the steam line following a turbine trip. Any lags inherent in the control system, however, will tend to reduce the pressure change.

2) A pressure rise will always occur during turbine runback if the inlet valve position is the controlling signal to the dump valve. Any additional lags will tend to increase the disturbance.

3) If the dump valve were operated identically on turbine trip and runback, a P_2 decrease (instead of an increase) will also accompany a turbine runback. This mode of operation would be more desirable from a safety-valve standpoint since too great a P_2 rise would trip safety valves.

The computer results have thus shown that an equal characteristic may be desirable for a turbine tripout not caused by overspeed but would definitely be undesirable for all other modes of operation because:

1) A linear characteristic is better from a control and stability standpoint for normal regulating dump valve operation.

2) A linear characteristic is a better match for the closing inlet valves during a turbine runback. The rate of change of steam flow with stroke is lower than a linear valve at small openings but much higher at high flows.

3.2.4 SIMULATION OF RELIEF-SAFETY VALVES

The four relief-safety valve characteristics were also included in the simulator. The valves were simulated with different opening and closing characteristics (valve flow vs pressure at the valve inlet) and variable popping and reclosing pressures.

The purpose of this simulation is to 1) study the superheater temperature response to popping of these valves under a variety of conditions; 2) determine the largest lag tolerable in the regulating dump valve during turbine runback and trip without popping of the safety valves; and 3) establish the optimum closing time for the main steam isolation valve.

3.2.5 SIMULATION OF ISOLATION VALVE

An isolation valve assembly in the steam line was proposed for Pathfinder and will have primarily two functions:

1) Fast closure for complete isolation of reactor building upon reaching a specified high radiation level.

2) Control valve for pressurizing the reactor vessel and admitting the steam to the turbine (or main condenser) during reactor startup.

The isolation valve assembly which was simulated, included:

1) A 16-in main steam isolation valve to close in 15 sec (nominal) after receiving a signal.

2) An isolation bypass valve in parallel with the 16-in valve to close in 2 min (nominal) after receiving a signal.

An Allis-Chalmers Roto-Valve was selected for the main steam isolation valve, and its flow coefficient vs. time was simulated. The isolation bypass valve was assumed to receive its signal to close instantaneously with the main valve, and then close linearly in 2 min. It was also decided that all main-steam isolation-valve closures will interrupt control rod magnet power, thus automatically scramming the reactor.

The simulation of the two-valve assembly will then be used to evaluate the following:

1) Reactor isolation with automatic scram.

2) Reactor isolation without scram with subsequent blowing of relief-safety valves.

3.2.6 SIMULATION OF BOILER HEAT TRANSFER

3.2.6.1 Transfer Function. The simulation of the boiler-fuel-element heat-transfer thermal lag was revised to correspond to the new stepped (2-diameter) Zircaloy-clad fuel pins. The heat capacity of the Zircaloy cladding was neglected with respect to that of the uranium dioxide, but its thermal resistance is included. An overall heat transfer coefficient from the edge of the fuel pellet to the coolant channel was again used, and a method of analysis similar to that of Iriarte*[19] was used. The heat transfer coefficient was approximated

19. M. Iriarte, "An Accurate Transfer Function for the Dynamic Analysis of the Temperature and Heat Release in Cylindrical Fuel Element," Nuclear and Science & Engineering, V. 7, No. 1, p. 26, Jan. 1960.

at 2100 Btu/sec-F-ft^2, and in the pellet the density is 636 lb/ft^3, the specific heat is 0.073 Btu/lb-F, and the thermal conductivity was assumed at 0.9 Btu/sec-F-ft. Assuming that 3 per cent of the power is gamma heating and appears immediately in the coolant channels, the revised transfer function becomes:

$$K_1 \frac{\dot{Q}_B}{n}(s) = \frac{0.766}{1 + 6.1s} + \frac{0.144}{1 + 1.2s} + \frac{0.06}{1 + 0.48s} + 0.03 \qquad (3.1)$$

where,

$\dot{Q}_B$ = Boiler heat appearing at fuel pin surface

n = neutron population

s = Laplace variable

K_1 = appropriate constant

3.2.6.2 Superheater and Boiler Heat Balance. The simulator was modified to include the steam generated separately in the superheater instead of lumping it with the boiler steam generation. The boiler thermal power contribution to the recirculation water at full power was established at 157.2 mw. The thermal power going to heat the superheater moderator flow is 2.7 mw, and the superheater power going to superheating steam is 39.7 mw. The thermal lag associated with the 157.2 mw is given in Eq. 3.1. The transfer of the 2.7 mw is assumed prompt (no lag), and the transfer function associated with the 39.7 mw is still:

$$K_2 \frac{\dot{Q}_s}{n} = \frac{L}{(1 + 0.95s)(1 + 0.15s)} \qquad (3.2)$$

where,

$\dot{Q}_s$ = superheater heat appearing at fuel surface

K_2 = appropriate constant

3.2.7 DOPPLER COEFFICIENT

The Doppler coefficient, relating reactivity changes to boiler fuel temperature, $\partial k_D / \partial \bar{T}_F$, was recalculated at 0.93×10^{-3} per cent $K_D/^oF$, corresponding to the revisions in the boiler core. The coefficient is linear over a wide range of operating temperatures, but will increase by a factor of 1.7 at reduced fuel temperatures, 60 to 100 F. This change in the coefficient will be taken into account in future accident studies at low power.

3.2.8 RESULTS ON SIMULATOR

Figures 3.7, 3.8, and 3.9 show further studies completed on the simulator with the reference pressure control system. Figure 3.8 shows that superheater pressure drop increases rapidly to about 190 psi if the bypass (dump) accidentally opens at full power. The annular 26-mil superheater fuel tubes can easily withstand this increased differential pressure, however, since test results have shown collapsing pressures to be about 800 psi.

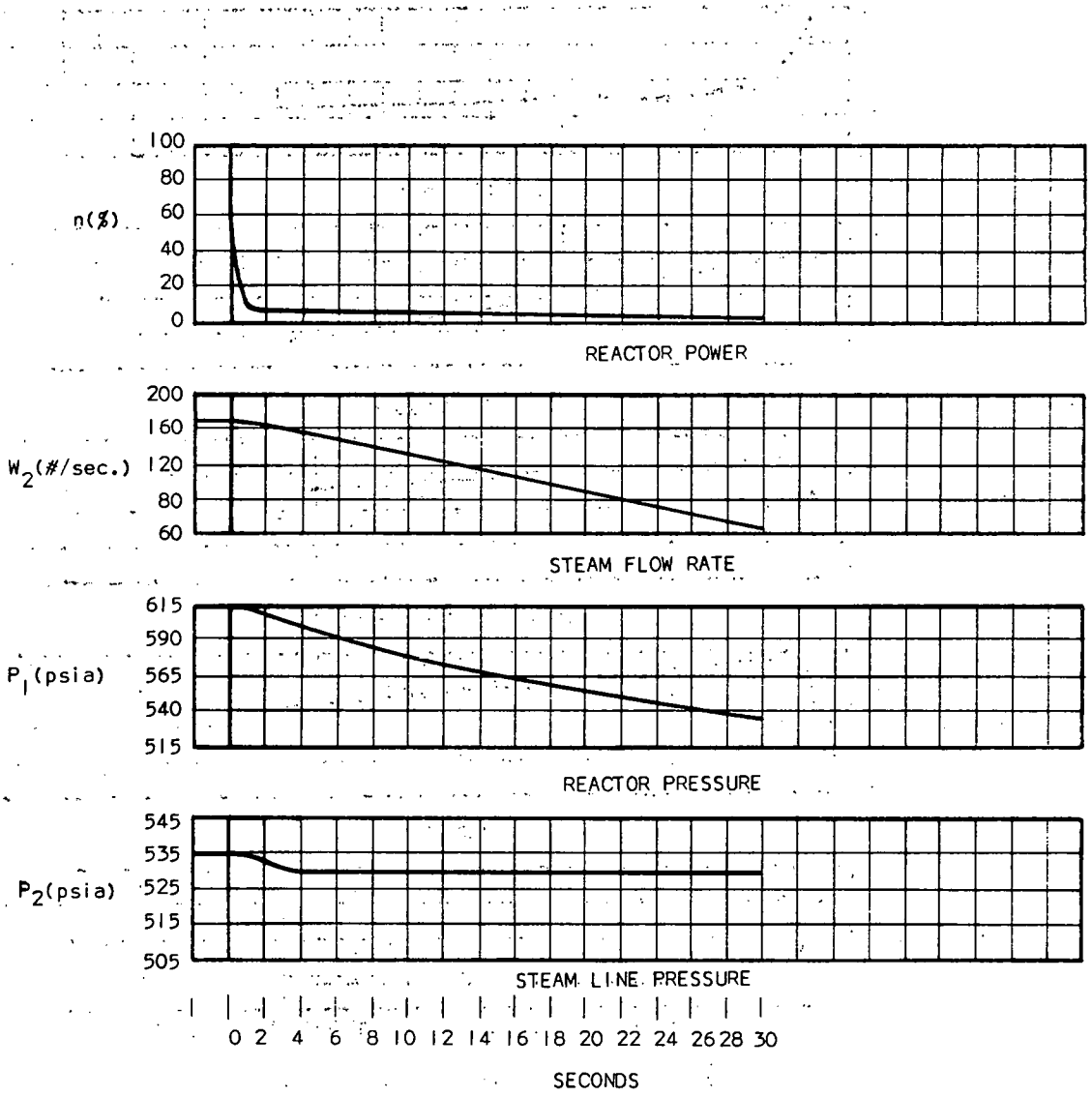

Figure 3.7 Reactor scram from 100 per cent power level with 10 dollars negative reactivity assumed in scram rods (A-C Dwg. 43-024-302)

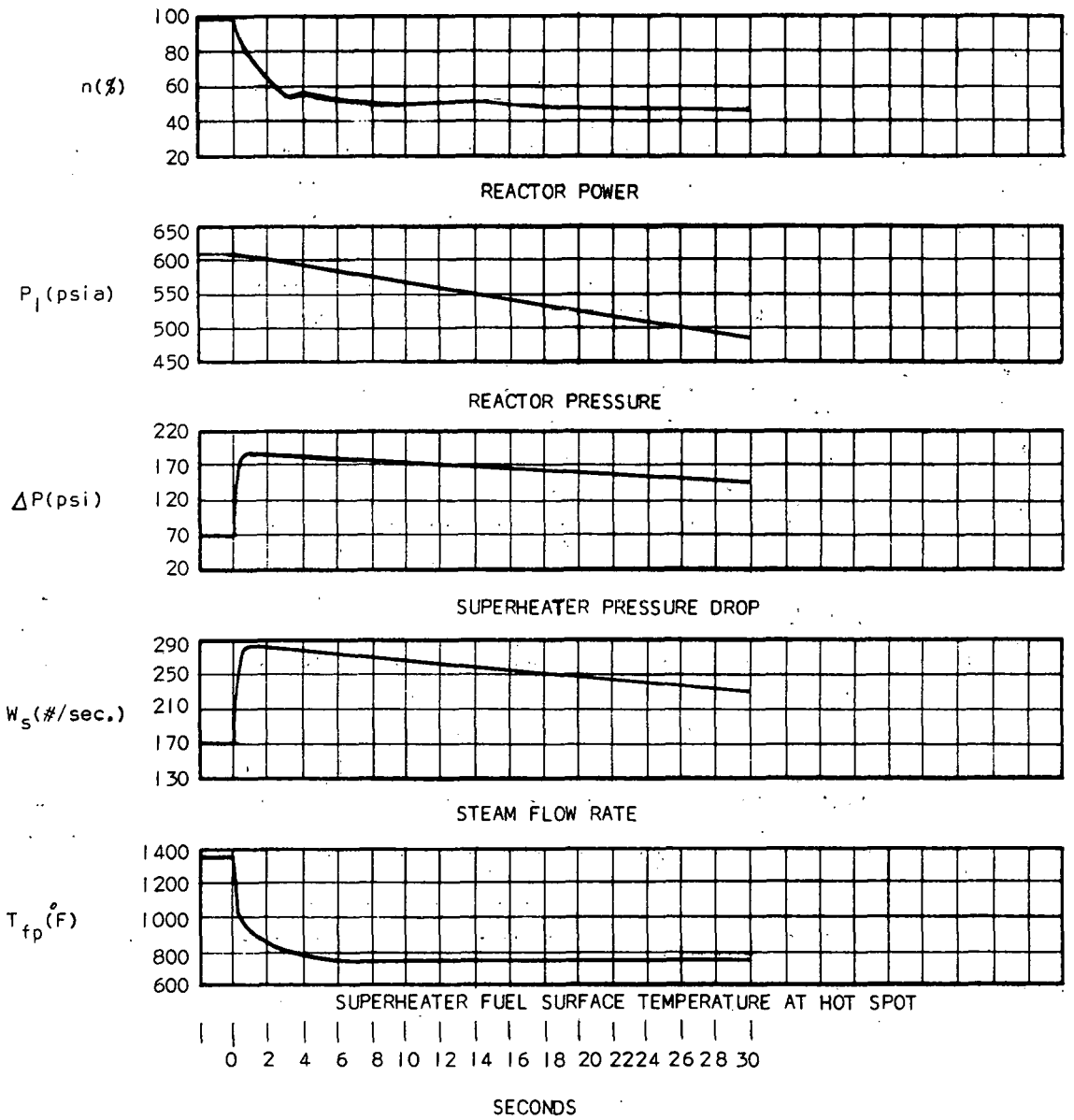

Figure 3.8 Accidental bypass valve opening with no automatic pressure control. (A-C Dwg. 43-024-301).

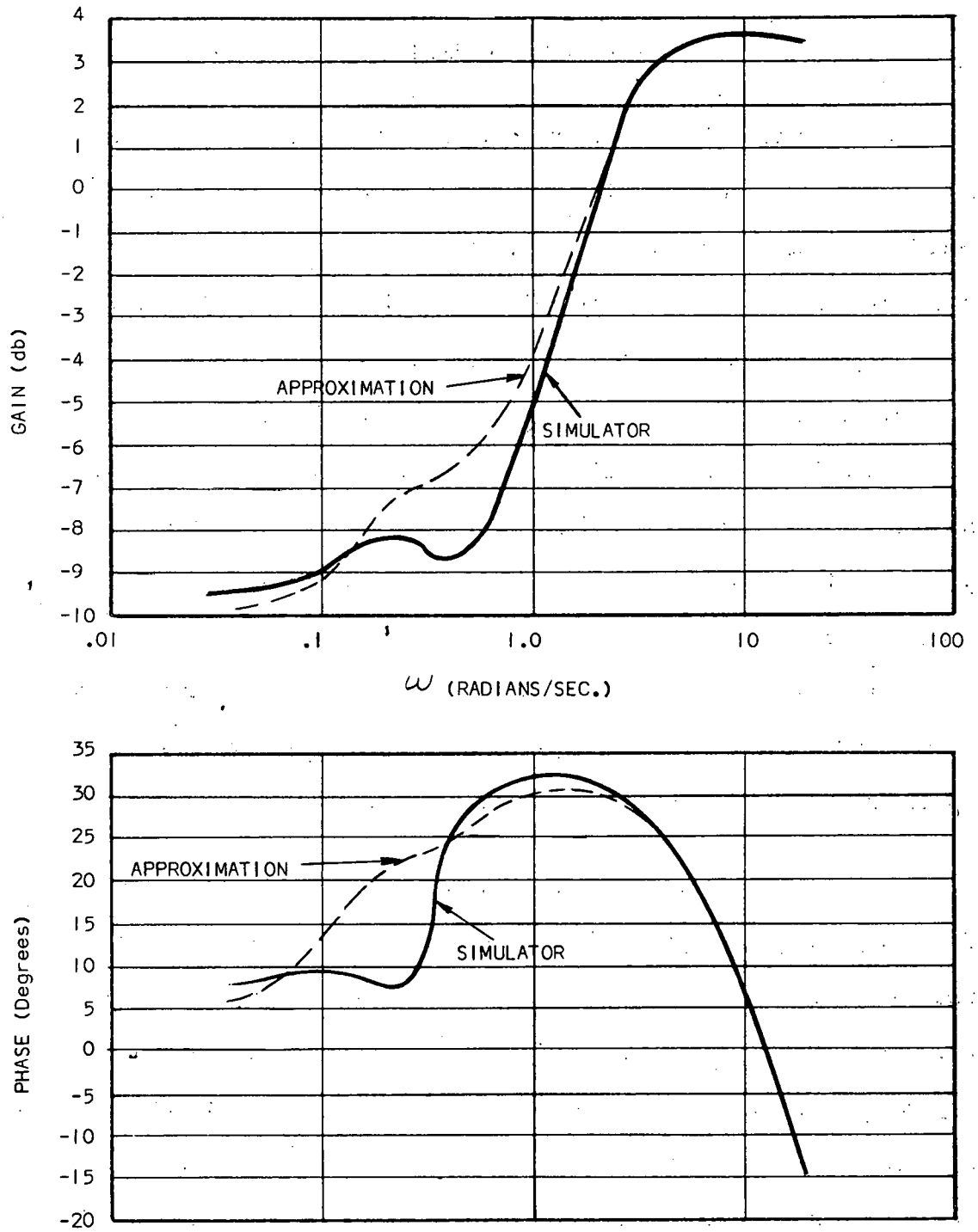

Figure 3.9 Pathfinder closed-loop frequency response.
(A-C Dwg. 43-024-298)

3.2.9 SIMPLIFICATION OF PATHFINDER SIMULATOR

In order to gain a clearer picture of the effects that various system parameters have on the system response, the complex system model was linearized and simplified so that an analytical study would be possible. Such a simplified model also aids stability studies.

Figure 3.10 shows the system block diagram after linearization and several assumptions. The closed-loop transfer function of this representation compares quite favorably with that from the complex simulator model, as is seen in Figure 3.9. The discrepancy is due to the fact that the transport lag in the recirculation loop was approximated as a first order lag.

This approximate mathematical system model will be applied to operating reactors in an attempt to verify experimentally the basic model from which the Pathfinder simulator was built.

3.2.10 HAZARDS CALCULATIONS

3.2.10.1 Superheater Draining Accident. The Pathfinder superheater was designed with a positive draining coefficient of reactivity. As a result, there is the possibility of an excursion upon accidental superheater draining during startup. In order to investigate the type of startup accident, the reactivity as a function of draining level in the superheater was found with a two-dimensional PDQ calculations.

Superheater draining rate is being calculated for several different conditions: draining through the relief valves, draining via

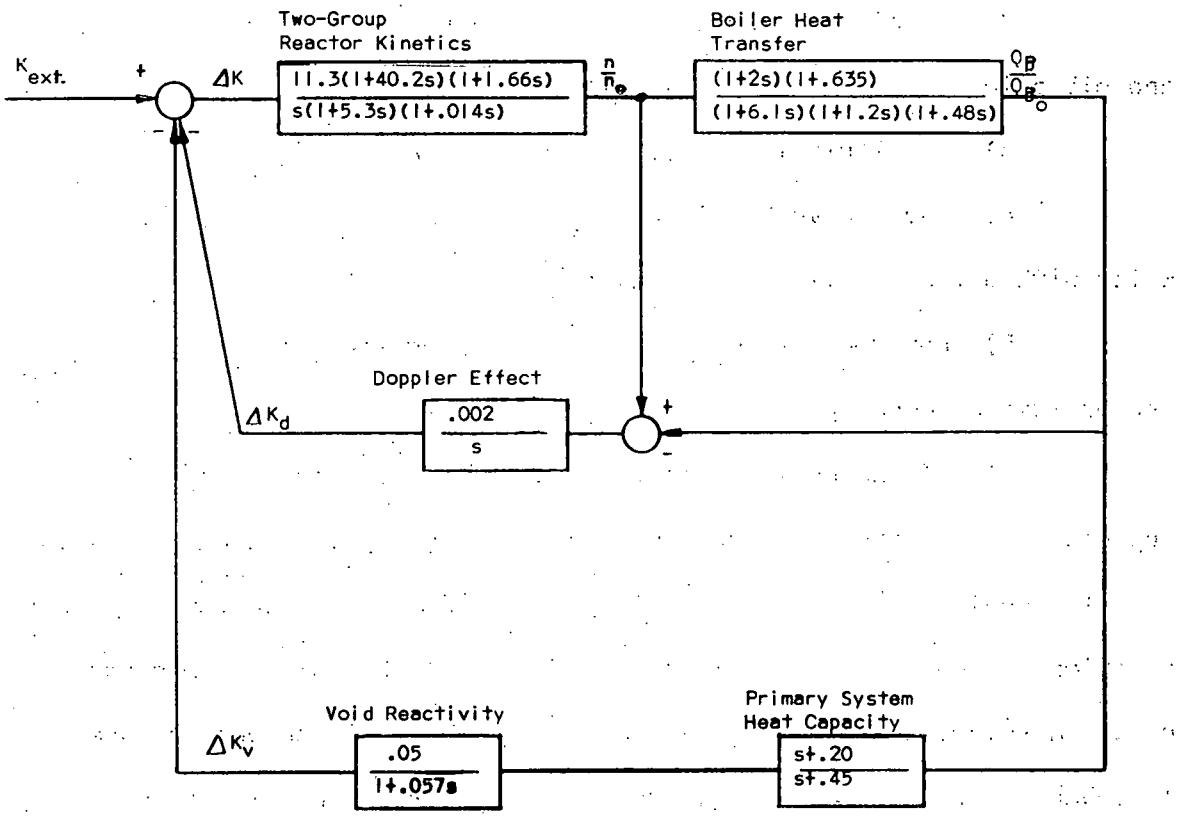

Figure 3.10 Linearized block diagram of reactor core dynamics. (A-C Dwg. 43-024-296).

the purification system, and draining through the main steam line isolation valve. As soon as these calculations are completed, a reactivity insertion rate for superheater draining will be obtained. This will then be used to investigate the power excursion during the accident.

3.2.10.2 Startup Accident. A generalized reactor startup accident was postulated consisting of a large positive reactivity addition causing a rapid pressure and power rise in the vessel, where:

1) the reactor is initially critical,

2) reactor pressure is initially anywhere between atmospheric and 615 psia,

3) recirculation pumps are forcing water through the core,

4) reactor vessel is practically filled with subcooled water with a very small steam (gas) dome, if any,

5) reactor can scram only due to high flux (low period causes automatic rod runback only),

6) if the reactor does not scram, relief safety valves at superheater exit are assumed to blow at about 615 psia and pass water.

The analysis of this accident consisted mainly of deriving a relation between the core heat release rate and the rate of pressure rise. Assumptions are being made regarding net steam generation due to subcooled boiling and the distribution of heat within the reactor vessel. It is assumed that the Doppler effect will be the only shutdown mechanism present; i. e., the negative reactivity due to void formation will be neglected.

3.2. II REACTOR PERFORMANCE AT REDUCED RECIRCULATION RATES

A study was initiated during the quarter to determine the transient performance of the reactor over a wide range of operating and startup conditions taking into account:

1) variable two-phase friction factor using a modified-Martinelli correlation,

2) variable recirculation pump head using results of recent hot loop pump tests.

3) variable void reactivity coefficient at lower void volumes.

Results of 1) and 2) will yield a relation describing the recirculation flow as a function of time, while 3) will determine reactor power as a function of time.

3.2.12 TIME DEPENDENT NEUTRON FLUX DISTRIBUTION

Using the void feedback model developed earlier for the simple one-dimensional model, a two-node hand analysis and a five-node analog computer analysis were made which show that no oscillations in flux shape will occur because of void formation and void transport up a coolant channel. A harmonic analysis, wherein neutron distribution and void distribution were expanded in a series of orthogonal functions, also showed that no oscillations of flux shape will occur in a boiling water reactor because of void formation and transport.

3.3 CRITICAL EXPERIMENTS

The object of this project is to perform the necessary critical experiments to check the theoretical calculations and provide a means of correlating theoretical and experimental results.

3.3.1 CONTROL ROD WORTH MEASUREMENTS

The first part of the control rod worth measurement was discussed in the last quarterly report, ACNP-6007. In summary, the core loading for this measurement consisted of 96 boiler elements with an average enrichment of 1.89 per cent. The superheater was fully loaded with 428 fuel elements, each element containing two fuel tubes but no poison rod. The lattice was a "cold clean" mockup. It was found that 950 grams of natural boron, uniformly distributed in the boiler core, was required to hold down the excess reactivity. The reactivity worth of this boron poison was determined to be 10 per cent, by incremental worth measurements and two-dimensional diffusion calculations.

The uniform boron poison was then replaced with 2 w/o boron-stainless steel control rods in a pattern as shown by Figure 3.11. Criticality was achieved with all rods either fully withdrawn or fully inserted, as noted, except for one regulating rod at about core midplane. Therefore, the worth of the 13-1/2 inserted rods is 10 per cent ΔK. The total control rod worth is the sum of this 10 per cent ΔK and the worth of the 6-1/2 rods required out for criticality. The worth of the 6-1/2 rods, as measured by the rod drop

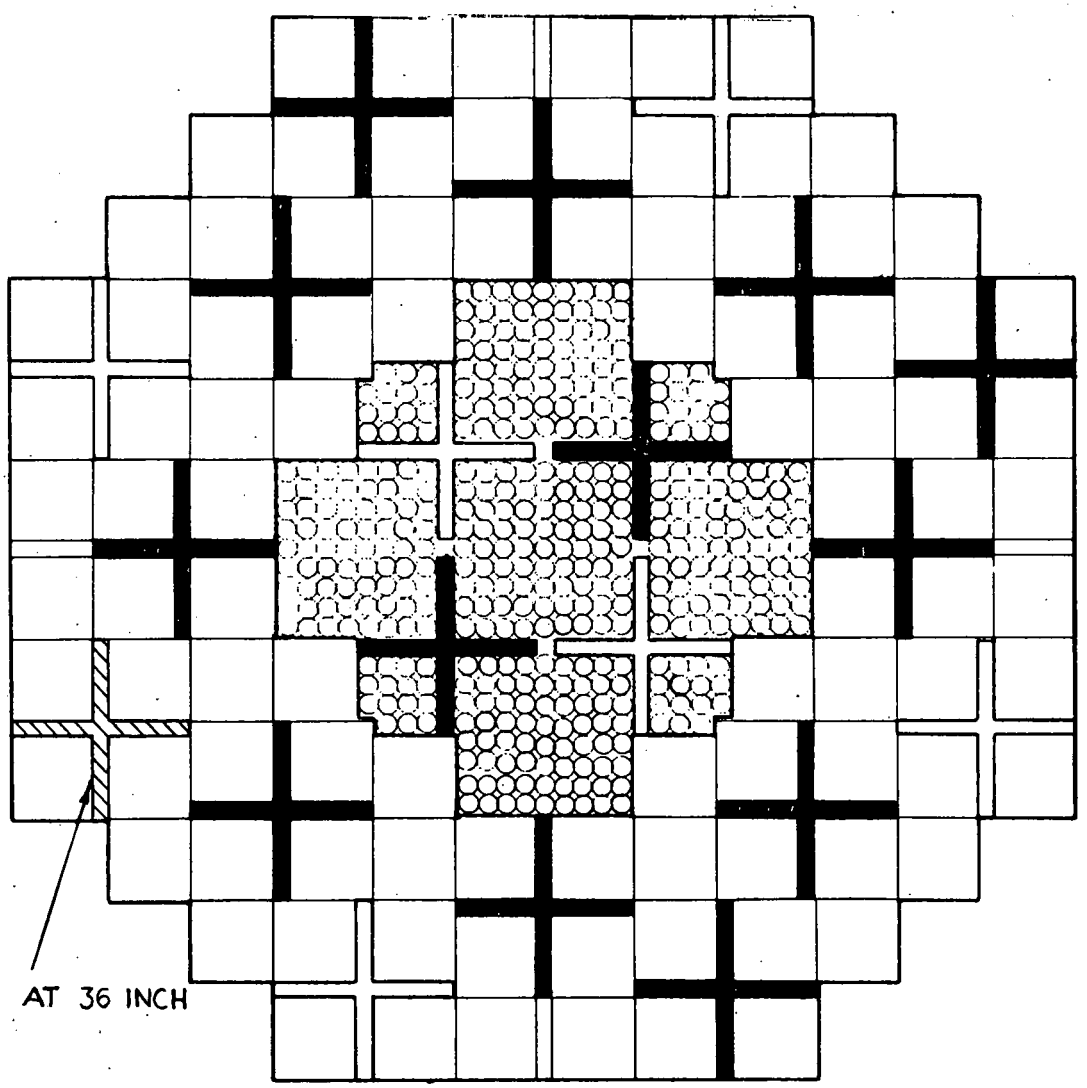

Figure 3.11 Control rod pattern for rod drop experiment. Solid rods denote full-in. White rods denote full out.

method described below, was found to be 3.6 per cent Δk, giving a total control rod worth of 13.6 per cent Δk. This is the control rod worth for the configuration cited, which was not an exact mock-up of the Pathfinder cold clean core.

Using methods that are being applied to the calculation of the

Pathfinder rod worth (refer to Section 3.1), control rod worth of 13.9 per cent Δk and 13.4 per cent Δk for the 81 and 64 rod section, respectively were calculated for this core. This is in good agreement with the 13.6 per cent Δk measured for the integral core of 81 rod lower and 64 rod upper lattices in this critical experiment.

3.3.2 ROD DROP EXPERIMENTS

This experiment was performed to determine the reactivity worth of 1/2 withdrawn and 6 fully withdrawn control rods in a full core already containing 13 fully inserted rods. The rod configuration is shown in Figure 3.12. Basically, the measurement consists of measuring the neutron count rate before and immediately after a rod drop. The reactivity associated with the dropped rods is a function of the ratio of the two count rates. (Count rate is here defined as the finite ratio $\Delta N/\Delta T$, not the differential dn/dt).

The apparatus consisted of a miniature fission counter, preamplifier, amplifier, scaler, printer, starting circuit, and timer. The miniature fission counter which was positioned at various locations within the core, was used to detect the neutron flux at criticality before the rod drop, and after the rods had been inserted. Prior to the drop with the reactor critical 15-sec counting rates were determined as a pre-drop reference. The starting circuit was then set (See Section 3.3.4) and the rods were scrammed. When the rods reached the full-in position (about 0.7 sec after scram), the starting circuit was energized, triggering the scaler, and the post-

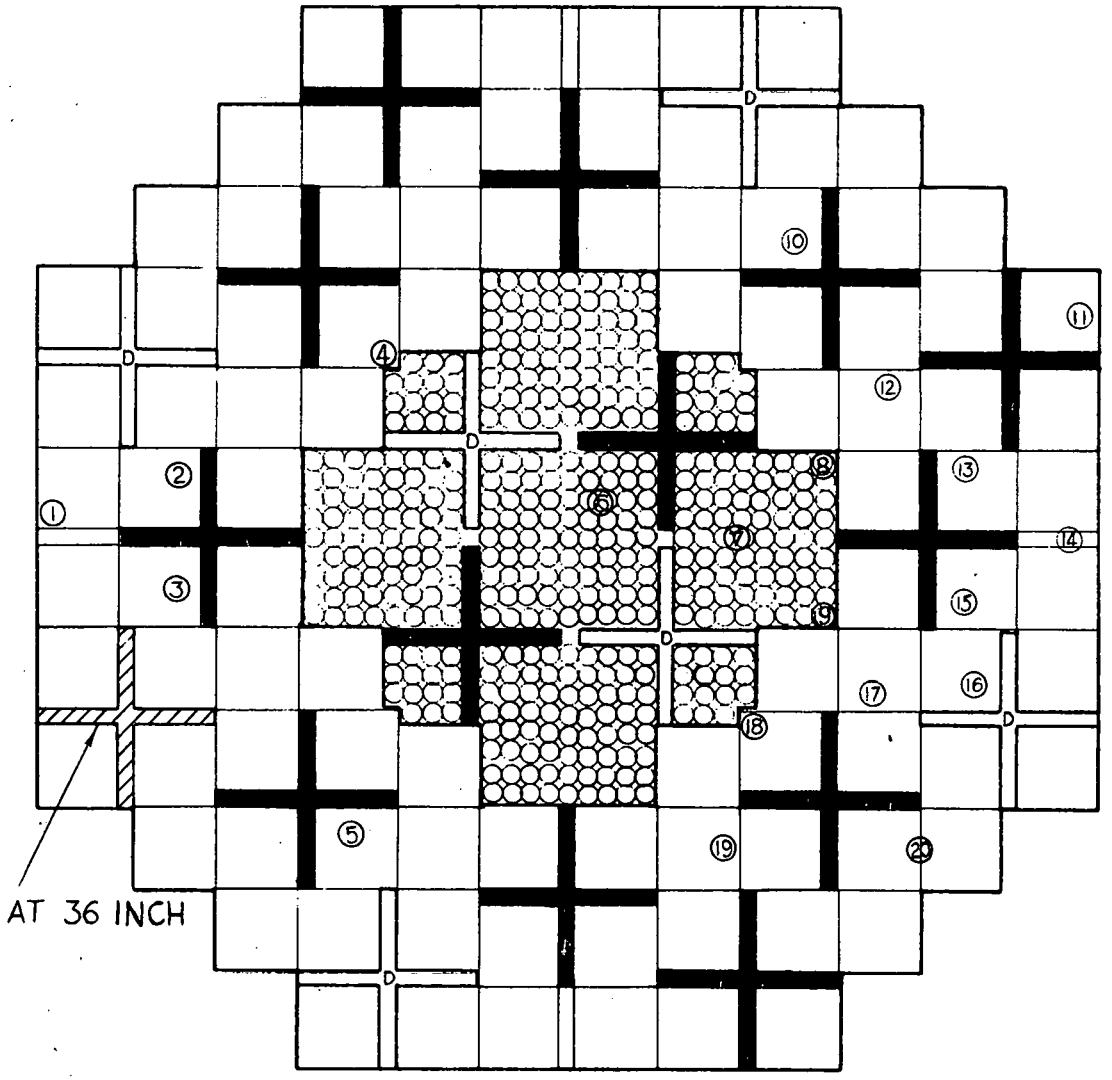

Figure 3.12 Location of data points for rod drop experiment. D denotes dropped; all other rods are stationary. Each point shown was taken at an axial location of 40 in. above the bottom of the fuel. The total fuel length is 72 in.

drop counting rate was measured. The counting of the post-drop flux lasted for 15 sec, at which time the integrated counts for this period was printed. This 15-sec counting rate was then the post-drop reference.

To a very good approximation, the negative reactivity inserted in a just critical (K = 1.00) reactor can be represented by $\rho = C(R-1)$, where C is a constant, and R is the ratio of pre-drop to post-drop neutron count rate that is begun immediately after the insertion. The time behavior of a critical reactor following a negative reactivity insertion is theoretically predicted by the neutron balance equation. The LaPlace transform technique was used to solve the equation, yielding R as a function of ρ and ΔT. For a ΔT of 15-sec and starting with reactivities of the order to be measured, the calculations yielded a value of 0.002733 $\pm$ 0.000003 for C for ρ expressed in percent $\Delta k/k$.

The ratio of pre-drop to post-drop neutron flux caused by a discrete absorber varies with the proximity of the measurement location to the absorber because of changes in the flux distribution. Therefore, the measurement of pre-drop to post-drop flux was made in 20 different reactor locations chosen to give a representative picture of the total behavior. The data point locations are also shown in Figure 3.12 and the measured value of ρ for each data point is presented in Table 3.4. To obtain a value for the reactivity worth of the rod drop, these values of ρ were appropriately averaged over the reactor core. A value of 3.6 per cent ΔK was obtained as the rod drop worth.

Not included in this tabulation are several measurements of the reproducibility at a given reactor location and measurements

TABLE 3.4 VALUES OF OBTAINED BY ROD DROP
(See Fig. 3.12 for location of data points)

Data Point	K (Per cent)	Data Point	K (Per Cent)
1	4.03	11	2.80
2	4.62	12	2.81
3	3.76	13	2.94
4	3.63	14	3.56
5	3.85	15	3.95
6	3.98	16	5.30
7	3.56	17	3.70
8	3.17	18	3.45
9	3.47	19	2.81
10	3.67	20	4.00

of the pre-drop to post-drop ratio at several axial positions of a fixed X-Y location. The reproducibility of the measurements were found to be within $\pm$ 3 per cent. No discernable variation in ρ was found between different axial positions of a fixed X-Y location.

3.3.3 MEASUREMENT OF CONTROL ROD DROP TIME

This experiment was performed to determine as accurately as possible the time interval from the instant a reactor scram signal is given until the control rods reach the full-in position.

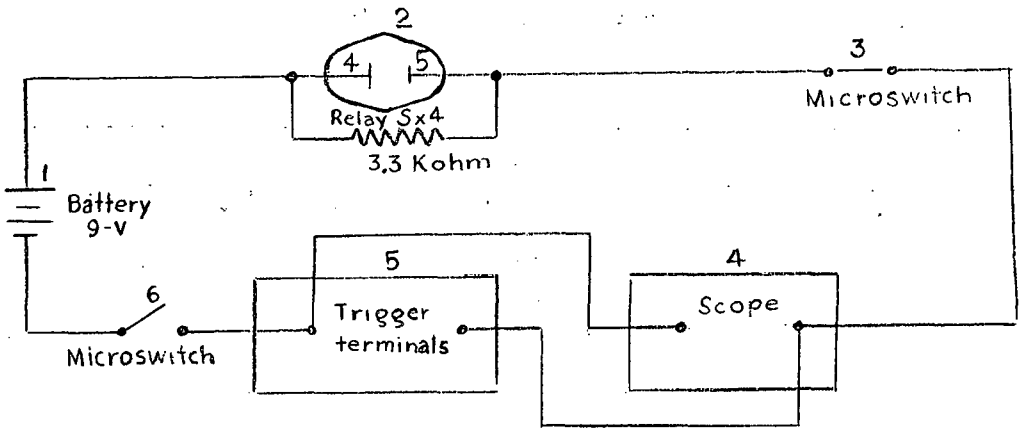

Figure 3.13 Schematic of electrical circuit for drop tests. The 9-v battery (1) supplied scope signal and trigger power. The normally open contacts (4,5) were part of relay Sx4 in the control console and closed on scram.

Apparatus used in this experiment included a power supply, a starting circuit, a micro-switch to indicate when the rod was in, and an oscilloscope with attached polaroid camera.

A schematic of the electrical circuit utilized for drop tests is shown in Figure 3.13.

The rod drop time tests were performed in conjunction with the rod drop experiments. The reactor was brought to power in a normal operating manner and upon reaching criticality at a certain power level and operating at this point for a short time, the reactor scram bar was pushed dropping all rods (five safety rods and two regulating rods). Although the majority of tests were performed under actual operating conditions with the rod dropping into a water-filled core, tests were also performed to determine the drop time in air. For the latter, tests were performed at shutdown condition with but

one rod (Safety 4) being raised and then dropped via the normal reactor scram push bar routine.

Briefly, the technique utilizing the scope is as follows: The scope provides its own light signal which will traverse the screen 10 cm in distance in any of several time settings. The beam traverse is initiated or triggered by an increment of voltage applied to the scope trigger terminals.

This light beam is deflected vertically when an external voltage is applied to the scope input terminals, the amount of vertical deflection is proportional to the voltage applied.

For the drop time tests, the sweep time was set at 0.1 cm/sec which then gave a total screen traverse time of 1 sec.

The sweep could have been triggered by the 9-v signal the instant the scram push bar activated relay Sx4 but for clarity the sweep was triggered by closing a microswitch (6) supplying approximately 1-v to the trigger input an instant before the scram bar was pushed.

Referring to Figure 3.14 the initial portion of the sweep initiated by closing the microswitch (6) was deflected upward slightly corresponding to the applied 9-v reduced by the voltage drop across the 3.3 kohm resistor. The instant the scram bar was pushed, relay Sx4 closed, shorting out the resistor and the light beam is deflected corresponding to the full 9-v applied. This 9-v trace was sustained until the rod dropped to its full-in position and actuated microswitch (3) opening the circuit. The remainder of the sweep is the base level beam originating in the scope.

IN AIR

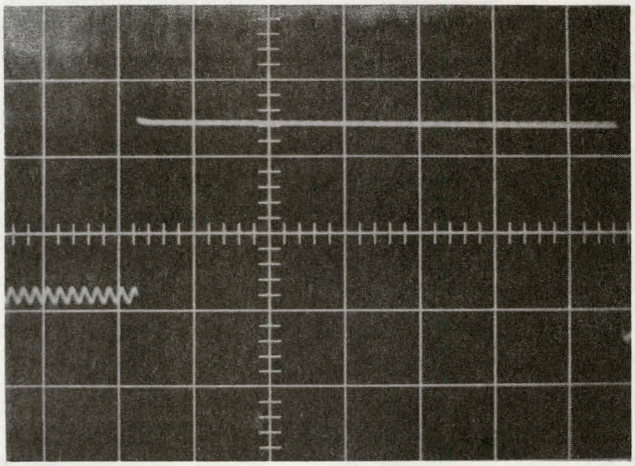

Drop Time: 0.64 Sec.

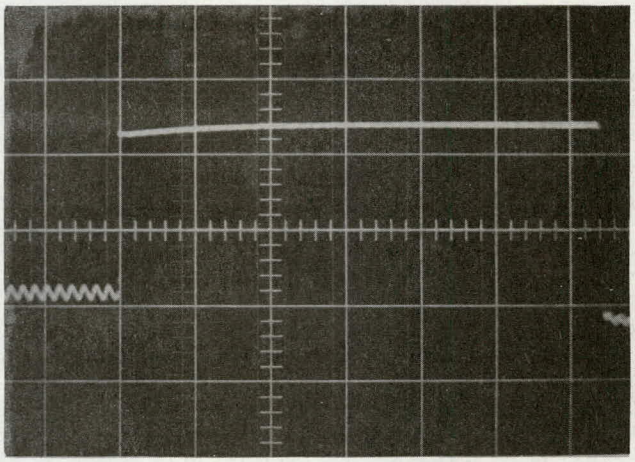

Drop Time: 0.64 Sec.

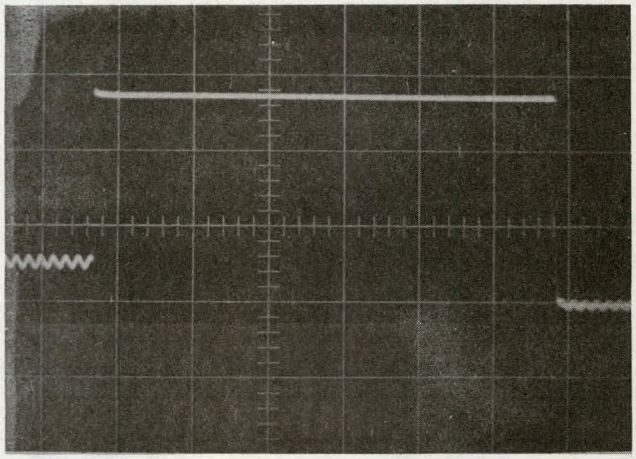

Drop Time: 0.63 Sec.

IN WATER

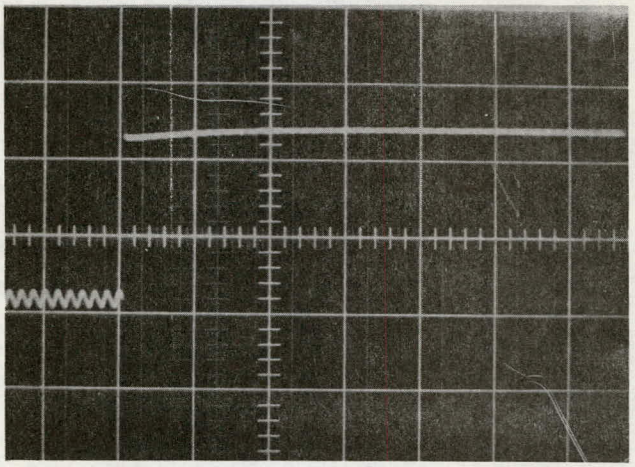

Drop Time: 0.68 Sec.

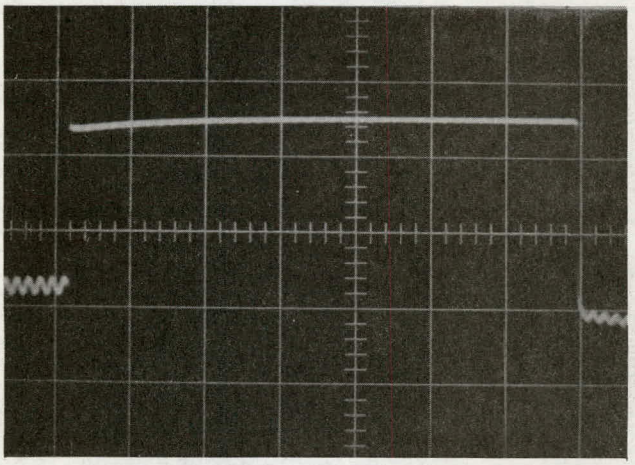

Drop Time: 0.68 Sec.

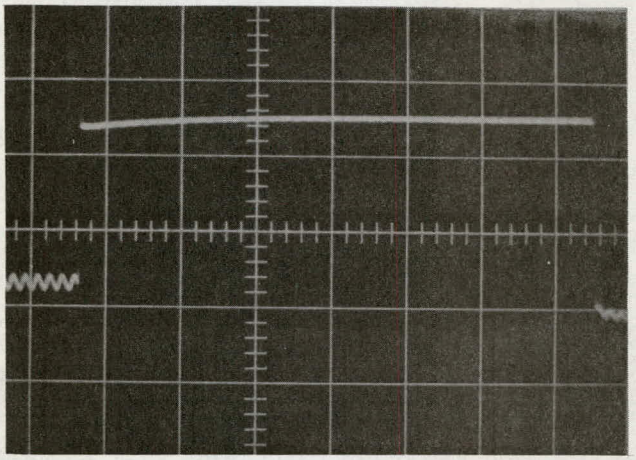

Drop Time: 0.68 Sec.

Figure 3.14 Measurement of control-rod drop time, safety rod No. 4, experiment No. 24. Major divisions on abscissa equal 0.1 sec.

Each large division on the photograph corresponds to 0.1 sec each small division to 0.02 sec. The drop time could then be determined to within one hundredth of a second by counting the divisions traversed by the 9-v signal.

Drop time was obtained for 17 reactor scrams during the rod-drop experiment. In 15 instances the measured drop time was 0.68 sec and the remaining drop times were measured as 0.67 sec.

Four rod drops were made in air at shutdown conditions with 1 rod drop time measured as 0.63 sec and three drop times in 0.64 sec.

THIS PAGE

WAS INTENTIONALLY

LEFT BLANK

PART B

POST CONSTRUCTION R&D

THIS PAGE

WAS INTENTIONALLY

LEFT BLANK

1. INITIAL STABILITY AND PERFORMANCE TESTS

The initial objective of this project is to fabricate a special oscillator control rod and drive mechanism together with suitable instrumentation to measure the resulting variations in neutron flux. This equipment will then be used to conduct oscillator tests in Pathfinder to verify dynamic performance calculations and to determine experimentally the stability of the reactor system.

1.1 OSCILLATOR ROD AND DRIVE

Layout of the oscillator rod was prepared, and the design is continuing. Difficulty was encountered in selecting the neutron poison. Boron steel was proposed, however, shaping and affixing it into the oscillator rotor is a problem. As a result, cadmium, 0.010 in. of which would be equivalent to 1/8 in of boron steel is being considered.

Since cadmium melts at 609 F, and since it will operate in the core at about 500 F, a test was conducted to determine its behavior at operating conditions. A stainless steel cylinder was plated with about 0.007 in of cadmium, placed in a furnace and held at 500 F for about a week. The objective was to determine the stability of cadmium at this temperature.

The results are encouraging, and further tests were started. These include the testing of a 0.070-in thick cadmium plate clamped between two stainless steel plates maintained at 500 F for several weeks. Also, two cylinders with shaped cadmium plate are being prepared for tests. Other poison materials are being investigated.

Another area that is being investigated is the oscillator rod rotor support bearing. This bearing will have to support about 100

pounds thrust load and operate at 490 F with water lubrication. Available bearing test data was obtained in tests at considerably lower speeds than are required (about 1/4 Pathfinder speed is the maximum available data). A test program is therefore being prepared to evaluate the various corrosion resistant water lubricated bearings under expected Pathfinder conditions.